Magneto-crystalline anisotropy of metallic nanostructures: Tight-binding and first-principles studies

Dongzhe Li

UNIVERSITE PIERRE ET MARIE CURIE
ECOLE DOCTORALE DE PHYSIQUE ET CHIMIE DES MATERIAUX

THESE

présentée pour obtenir le grade de:

Docteur de l'Université Pierre et Marie Curie

Spécialité: Physique

par

Dongzhe Li

Magneto-crystalline anisotropy of metallic nanostructures: Tight-binding and first-principles studies

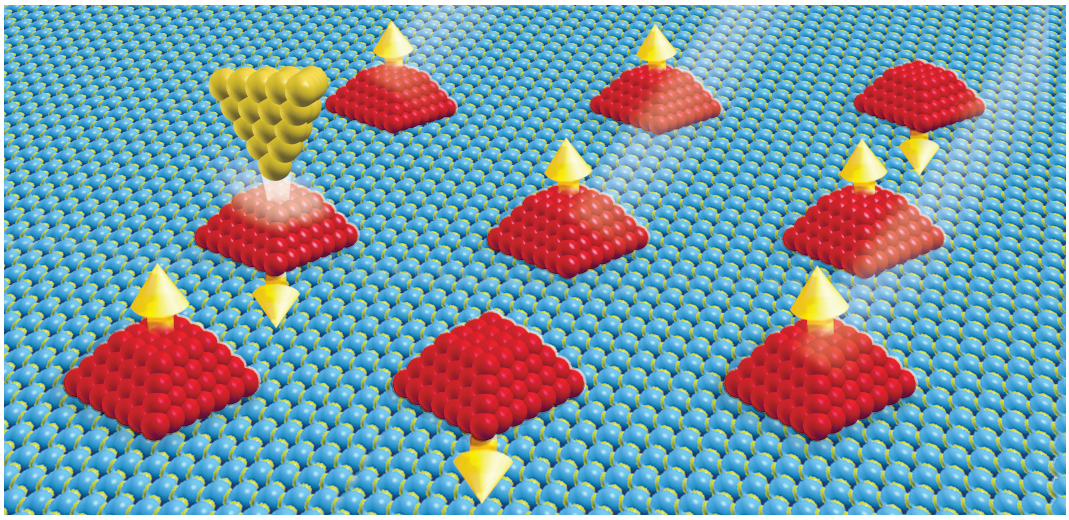

Soutenue le 30 Septembre 2015 en présence du jury composé de

Fabio Finocchi	Président du jury
Mairbek Chshiev	Rapporteur
Lionel Calmels	Rapporteur
Andres Saul	Examinateur
Gustav Bihlmayer	Examinateur
Cyrille Barreteau	Directeur de thèse
Alexander Smogunov	Co-directeur

Remerciements

Ce travail a été réalisé au Service de Physique de l'Etat Condensé (SPEC), laboratoire du CEA Saclay, au sein du groupe Groupe Modélisation et Théorie (GMT).

Je tiens tout d'abord à remercier mon directeur de thèse Cyrille Barreteau ainsi que mon co-directeur de thèse Alexander Smogunov, qui m'ont fait découvrir le monde de la recherche en physique.

Cyrille, grâce à toi j'ai pu démarrer ma thèse dans notre équipe théorique. Je te remercie pour ton soutien indéfectible, ta compétence et tes connaissance en physique. Tes questions justes et précises m'ont permis d'aborder les problèmes sous un angle nouveau, et ainsi d'éclaircir mes raisonnements.

Alexander (Sacha), un vrai théoricien russe, ton calme, ta gentillesse et ta bonne humeur sont toujours au rendez-vous. Je te remercie fortement pour ta patience et ta disponibilité pour m'expliquer la physique théorique, analytique et numérique. Notre discussion scientifique s'est déroulée tous les jours. Grâce à toi j'ai eu la chance d'étudier le transport polarisé en spin avec ton projet "Perfect Spin Filtering".

Je remercie également Fabien Silly pour sa contribution de mesure pour les nanocristaux métallique par STM.

Je tiens remercier François Daviaud et Patrice Roche, qui sont à la direction du SPEC, pour m'avoir accueilli au sein de ce laboratoire.

Un mot particulier à Yannick Dappe, Sylvain Latil et César González Pascual pour les discussions scientifiques, leurs conseils et aussi leur aides pour mon chemin de recherche de post-doc. Je remercie Alexey Kartsev et Julien Depres pour tous les échange plus informels et aussi pour notre "Afterwork" soirée. Merci aussi à tous les autres membres du GMT/SPEC, Jean-Louis Pichard, Geneviève Fleury, Michel Roger. Je souhaite beacoup de reussite à Daniela Di Felice dans sa thèse.

Je tiens remercier François Ducastelle et Daniel Spanjaard pour les discussions scientifiques. Je pense aussi à Jean-Baptiste Moussy, Corinne Kopec-Coelho, Nathalie Royer, Christine Prigian, Catherine Julien (ex-SPCSI), Daniel Bonamy, Ludovic Tortech (ex-SPCSI), Qirong Zhu, Pierre-André Guitard, Vincent Trauchessec, Maxime Rioult, Jelle Dionot, David Peyrot, Camille Blouzon, Thomas Aghavnian, Ludovic Douillard, Patrick

Hsia, Myriam Pannetier-Lecoeur, Grégoire de Loubens ...

Je remercie aussi le group de Vincent Repain au MPQ (Universié Paris Diderot) pour leur bonne manip STM sur l'anisotropie magnétique à l'interface métal-molécule qui colle avec nos calculs DFT avec le couplage spin-orbit.

Je tiens à remercier les membres du jury pour l'intérêt qu'ils ont porté à mon travail. Je remercie Fabio Finocchi (INSP - UPMC, Paris) pour m'avoir fait l'honneur de présider mon jury. Je remercie Andres Saul (CiNaM - Aix Marseille Université, Marseille) et Gustav Bihlmayer (Forschungszentrum Jülich GmbH, Allemagne) qui ont accepté d'en faire partie en tant qu'examinateurs. Je remercie particulièrement les rapporteurs Mairbek Chshiev (SPINTEC - CEA Grenoble, Grenoble) et Lionel Calmels (CEMES - Université Paul Sabatier, Toulouse) pour avoir eu la patience de lire et commenter ce manuscript.

Enfin je remercie ma famille, ma copine et mes amis pour leur soutien au cours de ces trois années de travail.

Contents

Abbreviations

AMR	anisotropic magnetoresistance
bcc	body centered cubic
DFT	density functional theory
fcc	face centered cubic
FR-PPs	fully-relativistic pseudopotentials
FT	force theorem
FT_{gc}	grand-canonical force theorem
GGA	generalized gradient approximation
hcp	hexagonal close packed
K-S	kohn-sham
LCN	local charge neutrality
LSDA	local spin density approxiamtion
MAE	magnetic anisotropy energy
MCA	magneto-crystalline anisotropy
MOKE	magneto-optic kerr effect
PDOS	projected density of states
PPs	pseudopotentials
QE	quantum espresso
QWS	quantum well states
SCF	self-consistent field
SOC	spin-orbit coupling
SP-STS	spin-polarized scanning tunneling spectroscopy
SR-PPs	scalar-relativistic pseudopotentials
TB	tight-binding
XMCD	x-ray magnetic circular dichroism

Introduction

Although magnetism is a relatively old topic in condensed matter physics, studies of nanomagnetism have attracted large attention for its potential applications such as the use of magnetic units down to nanoscale for high density magnetic recording [1, 2] or nonvolatile magnetoresistive random access memory (MRAM). Magnetic anisotropy is a general phenomenon that is characterized by the change of physical properties of a magnetic system with respect to the orientation of the magnetization. In particular, magnetic anisotropy energy (MAE), which is defined as the change of total energy associated to a change of the orientation of the spin moment (Fig. 1, left) is an extremely important quantity that is crucial for the stability of nano-scale magnetic grains. Such small nanoclusters are of great importance in view of future miniaturization of data storage devices since they have well-defined structure as well as an ability to assemble into well-ordered arrays on the substrate. However, the magnetic stability of a nanocrystal decreases proportionally to its size, therefore, one of the most challenging problems towards ultimate magnetic density storage is evidently to be able to synthesize well-ordered arrays of magnetic nanocrystals with as large magnetization and MAE as possible. That would prevent the magnetization flips due to thermal (or any other) fluctuations and increase the blocking temperature as it is sketched on Fig. 1 (left panel).

There are two physical sources for MAE, both of them are due to relativistic effects: the shape anisotropy and the magneto-crystalline anisotropy (MCA). The shape anisotropy is mediated by magnetic dipole-dipole interactions and originates from the quantum-field relativistic corrections to electron-electron interaction [4]. This long range interaction depends on the shape of the crystal and basically favors magnetization along the most elongated direction of the crystal. The physical origin of MCA is the spin-orbit coupling (SOC) which can be derived theoretically from the Dirac equation [5]. Unlike shape anisotropy, the MCA is a short range effect localized around atomic cores. SOC stands at the origin of many other intriguing features in low-dimentinal magnetic materials, such as rashba effect, magneto-optic Kerr effect (MOKE), tunnelling/balistic anisotropic magnetoresistance (AMR) [6–8], the chiral magneric order [9] and quantum anomolous Hall effect (QAHE) [10], to list a few. Understanding the role of the SOC in these phenomena is crucial for

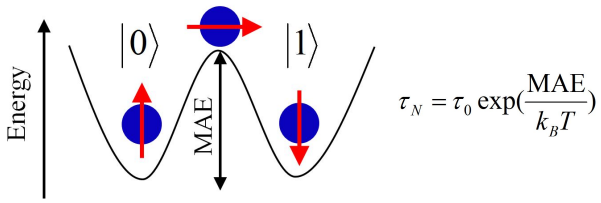

τ_N	1 s	1 mn	1 h	1 day	1 year	10 years
$\frac{\text{MAE}}{k_B T}$	23	27	31	34	40	43

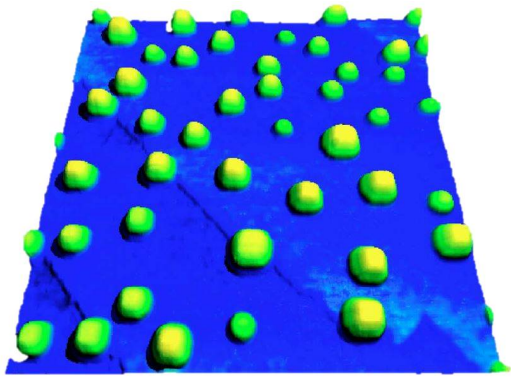

Figure 1: Left: Néel relaxation time τ_N – a mean time between two flips of the magnetic moment – with respect to the magnetic anisotropy energy MAE (over temperature), where k_B is the Boltzmann constant, T is the temperature and τ_0 is the attempt time (typical values of which are between 10^{-9} and 10^{-10} seconds). Right: 3D representation of scanning tunneling microscopy (STM) topography of truncated pyramid-shaped Fe nanocrystals of nanometer-size grown on $SrTiO_3(001)$ substrate [3].

both fundamental interests and practical applications.

A large MCA is expected in the systems with large spin moments and SOC. Large spin moments are usually found in magnetic $3d$ metals while the SOC is rather weak there. Heavy $4d$ or $5d$ materials, on the contrary, have larger SOC but are normally nonmagnetic. Therefore, in order to get both large magnetization and MCA, one is particularly interested in the nanostructured "cheap" $3d$ transition metal systems or in bimetallic systems consisting of $3d$ elements deposited on $5d$ heavy element substrate. In $3d$ bulk transition-metal, the value of MCA per atom is extremely small (some μeV/atom) in cubic systems such as Fe, Cr and Ni due to the high symmetry reason while it is larger ($\sim$ 65 μeV/atom) in noncubic systems such as hexagonal close packed (hcp) Co. The MCA can get much larger in nanostructures (some meV/atom) such as adatoms, ultrathin films or nanoclusters compared to their bulk values because of both reduced dimensionality and lower coordination number. More recently, scientists have shown for the first time that one can reach the maximum theoretical limit of the energy required to control the magnetization of a $3d$ single atom. The magnetic anisotropy limit was found $\sim$ 60 meV [11]. Due to the smallness of the energy differences in play, the determination of MCA still remains numerically delicate.

From a theoretical point of view, to deal with SOC in a density functional theory (DFT) scheme necessitates a full-relativistic formalism (at least for the determination of pseudopotentials). Technically, several approaches have been developed for the determination of the MCA. The brute force method consists in performing self-consistent field (SCF) calculations including SOC for various orientations of the magnetization [12]. This approach, although straightforward, is the most computationally demanding and hard to converge. One should use penalization techniques to obtain the total energy for any spin confuguration. Rather early it was recognized that small changes of the total energy could

be related to the changes of the eigenvalues of the Hamiltonian. This is the so-called force theorem [13, 14] that the MCA is given by band energy difference instead of total energy difference obtained after a one-step diagonalization of the full Hamiltonian including SOC, starting from the SCF scalar relativistic density/potential. Besides its computational efficiency, it is also very stable numerically, but it cannot be applied to systems with large SOC. Several works are also based on a perturbative treatment that consists in writing to second order the energy correction due to the spin-orbit Hamiltonian treated as a perturbation [15, 16]. Bruno [17] has also derived an interesting relation between the orbital moment and the MCA in a ferromagnet based on the second-order perturbation theory by ignoring the spin-flip excitations. It is often used for the analyses of the results obtained in models and first-principles calculations [18–21]. An extension of the Bruno's formula considering also contribution from the spin-flip process in an approximated way has been proposed [22]. In addition, for systems with uniaxial symmetry, the MCA can be evaluated through the expectation value of the angular derivative of the SOC Hamiltonian (torque) at an angle of $\theta = 45°$, where θ is the angle between the magnetization and the normal axis, leading to so-called torque method [23]. Moreover, the case of large-scale systems is generally treated with empirical Neel-like model [24].

Recent experiments showed that it is possible to grow Fe [3] and Co [25] nanocrystals by epitaxy on $SrTiO_3$ substrate with a remarkable control of size, shape and structure, as shown in Fig. 1 (right panel). More precisely, the nanocrystals are in shape of truncated-pyramids of nanometer size with well-defined length to height ratio and containing 2 different facets only. The nanocrystals adopt a truncated-pyramid shape on a reconstructed $SrTiO_3(001)$ substrate but can however adopt, a different bulk structure: body-centered cubic (bcc) for Fe and face-centered cubic (fcc) for Co. The structure and shape of nanocrystals govern their magnetic properties at the nanometer size. This PhD thesis is devoted to the study of the electronic and magnetic properties of these particular Fe and Co nanocrystals on $SrTiO_3$ using both semi-empirical tight-binding model and first-principles calculations, with a particular emphasis on the MCA. An important part of this study was dedicated to the determination of a proper local decompositon of MCA that we have applied to different magnetic nanostructures. It is based on a careful implementation of the force theorem within the grand-canonical formulation in the tight binding model [18, 26, 27] as well as in QUANTUM ESPRESSO package [28].

This manuscript is organized in five chapters. In chapter 1, a short introduction to spin DFT will be given, followed by a description of our tight-binding model used in this work. Chapter 2 is devoted to the pratical implementation details of the force theorem within the grand-canonical formulation by tight-binding and DFT. In chapter 3, the MCA of two-dimensional Fe and Co free-standing slabs with different crystallographic orientations is investigated with a particular emphasis on the local analysis of MCA. Chapter 4 is devoted to the MCA of free Fe and Co nanocrystals (containing up to several hundred atoms) in shape of truncated pyramids. In chapter 5, the MCA at Fe(Co)|$SrTiO_3$ interfaces and of small Fe and Co clusters deposited on $SrTiO_3$ is studied. Finally, we give conclusions and perspectives of this work.

CHAPTER 1

Methods

In this chapter, we describe two basic electronic structure methods used in this PhD study. In the first part, I will briefly discuss the spin density functional theory with a particular emphasis on non-collinear magnetism. In the second part, a semi-empirical magnetic tight-binding model will be presented.

1.1 Spin Density Functional Theory

1.1.1 The many-body Hamiltonian

To discuss the electronic structure of a many-body (interacting) system, it is natural to start with non-relativistic Schrödinger equation:

$$H_{\text{total}}\Psi_{\text{total}} = E_{\text{total}}\Psi_{\text{total}}, \tag{1.1}$$

where the Hamiltonian for a system of M nuclei and N electrons can be written as follows:

$$H = -\sum_{A=1}^{M}\frac{\hbar^2}{2M_A}\nabla_A^2 - \frac{\hbar^2}{2m}\sum_{i=1}^{N}\nabla_i^2 - e^2\sum_{i=1}^{N}\sum_{A=1}^{M}\frac{Z_A}{r_{iA}} + \frac{1}{2}\sum_{i\neq j}^{N}\frac{e^2}{r_{ij}} + \frac{e^2}{2}\sum_{A\neq B}^{M}\frac{Z_A Z_B}{R_{AB}}. \tag{1.2}$$

The first two terms describe the kinetic energy of the nuclei and electrons while the other three terms represent the nuclei-electron, electron-electron and nuclei-nuclei interactions, respectively.

The Born-Oppenheimer approximation is usually introduced which is the assumption that the nuclei are nearly fxed with respect to electron motion due to the mass of nuclei

being much larger than the electron mass. Then the total wavefunction can be factorized in a product of nuclei and electronic components $\Psi_{\text{total}} = \Psi_{\text{elec}} \times \Psi_{\text{nuclei}}$. The electronic many-body Schrödinger equation is written as follows:

$$H\Psi = E\Psi, \tag{1.3}$$

(we suppress from now on the index elec) with electronic Hamiltonian

$$H = -\frac{\hbar^2}{2m}\sum_{i=1}^{N}\nabla_i^2 - e^2\sum_{i=1}^{N}\sum_{A=1}^{M}\frac{Z_A}{r_{iA}} + \frac{1}{2}\sum_{i\neq j}^{N}\frac{e^2}{r_{ij}} = T + V + U. \tag{1.4}$$

containing kinetic T, single-body V (due to, for example, electron-nuclei interactions) and electron-electron U contributions as defined explicitely in the last line. The solution of Eqs. 1.3, 1.4 gives the electronic wavefunction Ψ and the electronic energy E. The total energy is then the sum of E and the constant contribution from nuclei-nuclei potential if the latters are treated classically.

We will focus solely on the electron part, which is itself a formidable problem. Although the nuclei-electron interaction is by no means simple, it can be treated, whereas the electron-electron interaction is just impossible to accomplish without some approximations.

1.1.2 The Kohn-Sham equation

The Density Functional Theory (DFT) is the most successful approach in terms of parameter-free *ab initio* description for computing electronic structure of matter. The theoretical footing of DFT is based on two theorems provided by Hohenberg and Kohn in 1964 [29, 30].

The first Hohenberg-Kohn theorem states that there are one-to-one mapping between external potential $V(\mathbf{r})$, the ground state electron wave function $\Psi(\mathbf{r}_1, \mathbf{r}_2, ..., \mathbf{r}_N)$ and, further, the ground state density $n(\mathbf{r})$ as it is represented below:

$$V(\mathbf{r}) \leftrightarrow \Psi(\mathbf{r}_1, \mathbf{r}_2, ..., \mathbf{r}_N) \leftrightarrow n(\mathbf{r}). \tag{1.5}$$

Therefore, all the observables in the ground state are unique functionals of the electron density $n(\mathbf{r})$ which is much simpler than the wave function since it depends on only one variable $\mathbf{r}$.

The second Hohenberg-Kohn theorem states that the exact ground state density $n(\mathbf{r})$ corresponding to the external potential $V(\mathbf{r})$ minimizes the energy functional:

$$\frac{\delta E_V[n(\mathbf{r})]}{\delta[n(\mathbf{r})]} = \mu, \tag{1.6}$$

where μ is the chemical potential and

$$E_V[n] = \langle\Psi[n]|T + U|\Psi[n]\rangle + \int V(\mathbf{r})n(\mathbf{r})d\mathbf{r}, \tag{1.7}$$

where $\Psi[n]$ is the inverse of the last map in Eq. 1.5.

In 1965, Kohn and Sham [31] proposed an efficient way to solve for $n(\mathbf{r})$ mapping a "real" interacting electrons problem to the one of non-interacting electrons. They suggested to rewrite the variational functional $E_V[n]$ in the following way:

$$E_V[n] = T_s[n] + \int V(\mathbf{r})n(\mathbf{r})d\mathbf{r} + \frac{e^2}{2}\int\int \frac{n(\mathbf{r})n(\mathbf{r}')}{|\mathbf{r}-\mathbf{r}'|}d\mathbf{r}d\mathbf{r}' + E_{xc}[n]. \tag{1.8}$$

Here $T_s[n]$ is the kinetic energy of non-interacting electrons, $T_s[n] = \langle\Psi_s[n]|T|\Psi_s[n]\rangle$, where $\Psi_s[n]$ is the inverse of the last map in Eq. 1.5 for non-interacting electrons. All remaining corrections are collected in the exchange-correlation functional, $E_{xc}[n]$, which is unknown and needs to be approximated, in general.

The variational problem for so written functional is then equivalent to solution of single-particle effective equations:

$$\left[-\frac{\hbar^2}{2m}\bigtriangledown^2 + V_{\text{eff}}(\mathbf{r})\right]\phi_i(\mathbf{r}) = \epsilon_i\phi_i(\mathbf{r}), \tag{1.9}$$

$$V_{\text{eff}}(\mathbf{r}) = V(\mathbf{r}) + e^2\int\frac{n(\mathbf{r}')}{|\mathbf{r}-\mathbf{r}'|}d\mathbf{r}' + V_{xc}(\mathbf{r}), \tag{1.10}$$

where ϕ_i are the so-called Kohn-Sham (K-S) orbitals of the non-interacting system and $V_{xc}(\mathbf{r}) = \delta E_{\text{xc}}[n(\mathbf{r})]/\delta n(\mathbf{r})$ is the exchange-correlation potential. The electron density is then given by:

$$n(\mathbf{r}) = \sum_i^{\text{occ}} |\phi_i(\mathbf{r})|^2 \tag{1.11}$$

so that the K-S equations have to be solved self-consistently. It is very important to realize that the K-S scheme would produce exact ground state density $n(\mathbf{r})$ and, as a consequence, the total energy if one knew the exact exchange-correlation functionals.

1.1.3 Non-collinear magnetism

Spin-polarized Kohn-Sham equation

If electron system is moreover coupled to external magnetic field $\mathbf{B}(\mathbf{r})$, the first Hohenberg-Kohn theorem can be generalized and one-to-one mappings can be now established:

$$\{V(\mathbf{r}), \mathbf{B}(\mathbf{r})\} \leftrightarrow \Psi(\mathbf{r}_1\sigma_1, \mathbf{r}_2\sigma_2, ..., \mathbf{r}_N\sigma_N) \leftrightarrow \{n(\mathbf{r}), \mathbf{m}(\mathbf{r})\}, \tag{1.12}$$

where now, in addition to position $\mathbf{r}_i$, also spin index σ_i is introduced for i-th electron. All the observables in the ground state are now unique functionals of $n(\mathbf{r})$ and the spin magnetization $\mathbf{m}(\mathbf{r})$.

Kohn-Sham scheme is established by introducing the total energy variational functional $E_{V,\mathbf{B}}[n,\mathbf{m}]$ in the following way:

$$E_{V,\mathbf{B}}[n,\mathbf{m}] = T_s[n,\mathbf{m}] + \int V(\mathbf{r})n(\mathbf{r})d\mathbf{r} - \int \mathbf{B}(\mathbf{r})\mathbf{m}(\mathbf{r})d\mathbf{r} + \frac{e^2}{2}\int\int \frac{n(\mathbf{r})n(\mathbf{r}')}{|\mathbf{r}-\mathbf{r}'|}d\mathbf{r}d\mathbf{r}' + E_{xc}[n,\mathbf{m}], \tag{1.13}$$

where exchange-correlation energy $E_{\rm xc}$ is the functional of both electron and magnetization densities. Konh-Sham equations for two-component spinor wavefunctions state:

$$\left[-\frac{\hbar^2}{2m}\bigtriangledown^2 + V_{\rm eff}(\mathbf{r}) - \mu_B\boldsymbol{\sigma}\mathbf{B}_{\rm eff}(\mathbf{r})\right]\begin{pmatrix}\phi_i^{\uparrow}\\ \phi_i^{\downarrow}\end{pmatrix} = \epsilon_i\begin{pmatrix}\phi_i^{\uparrow}\\ \phi_i^{\downarrow}\end{pmatrix}, \tag{1.14}$$

$$V_{\rm eff}(\mathbf{r}) = V(\mathbf{r}) + e^2\int\frac{n(\mathbf{r}')}{|\mathbf{r}-\mathbf{r}'|}d\mathbf{r}' + V_{xc}(\mathbf{r}), \tag{1.15}$$

$$\mathbf{B}_{\rm eff}(\mathbf{r}) = \mathbf{B}(\mathbf{r}) - \mathbf{B}_{xc}(\mathbf{r}), \tag{1.16}$$

where $\boldsymbol{\sigma}$ is the vector made of Pauli matrices:

$$\sigma_x = \begin{pmatrix}0 & 1\\ 1 & 0\end{pmatrix}, \sigma_y = \begin{pmatrix}0 & -i\\ i & 0\end{pmatrix}, \sigma_z = \begin{pmatrix}1 & 0\\ 0 & -1\end{pmatrix} \tag{1.17}$$

and $V_{xc}(\mathbf{r}) = \delta E_{\rm xc}[n(\mathbf{r}),\mathbf{m}(\mathbf{r})]/\delta n(\mathbf{r})$ and $\mathbf{B}_{xc}(\mathbf{r}) = \delta E_{\rm xc}[n(\mathbf{r}),\mathbf{m}(\mathbf{r})]/\delta\mathbf{m}(\mathbf{r})$ are exchange-correlation potential and magnetic field, respectively. The electron density and spin magnetizations are given by:

$$n(\mathbf{r}) = \sum_i^{occ}|\phi_i^{\uparrow}(\mathbf{r})|^2 + |\phi_i^{\downarrow}(\mathbf{r})|^2, \tag{1.18}$$

$$\mathbf{m}(\mathbf{r}) = \sum_i^{occ}\phi_i^{\alpha *}(\mathbf{r})\boldsymbol{\sigma}_{\alpha\beta}\phi_i^{\beta}(\mathbf{r}), \tag{1.19}$$

where magnetic moment is expressed in units of magneton Bohr, $\mu_B = e\hbar/2mc$ (e is the electron charge).

Equivalently, the theory can be formulated in terms of spin density matrix:

$$\tilde{n}(\mathbf{r}) = \begin{pmatrix}n^{\uparrow\uparrow}(\mathbf{r}) & n^{\uparrow\downarrow}(\mathbf{r})\\ n^{\downarrow\uparrow}(\mathbf{r}) & n^{\downarrow\downarrow}(\mathbf{r})\end{pmatrix}. \tag{1.20}$$

which in terms of Kohn-Sham orbitals is given by:

$$n^{\alpha\beta}(\mathbf{r}) = \sum_i^{occ}\phi_i^{\alpha *}(\mathbf{r})\phi_i^{\beta}(\mathbf{r}). \tag{1.21}$$

The relation to the charge and spin magnetizations are provided by:

$$n(\mathbf{r}) = {\rm Tr}[\tilde{n}(\mathbf{r})]; \quad \mathbf{m}(\mathbf{r}) = {\rm Tr}[\tilde{n}(\mathbf{r})\cdot\boldsymbol{\sigma}] \tag{1.22}$$

and vice versa:

$$\tilde{n}(\mathbf{r}) = \frac{1}{2}(n(\mathbf{r})\tilde{\mathbf{I}} + \boldsymbol{\sigma}\cdot\mathbf{m}(\mathbf{r})) = \frac{1}{2}\begin{pmatrix} n(\mathbf{r}) + m_z(\mathbf{r}) & m_x(\mathbf{r}) - im_y(\mathbf{r}) \\ m_x(\mathbf{r}) + im_y(\mathbf{r}) & n(\mathbf{r}) - m_z(\mathbf{r}) \end{pmatrix}, \tag{1.23}$$

If the exchange-correlation energy is expressed in terms of the spin density matrix, $E_{\mathrm{xc}}[\tilde{n}(\mathbf{r})]$, the 2×2 matrix of exchange-correlation potential, $\tilde{V}_{\mathrm{xc}}(\mathbf{r}) = \delta E_{\mathrm{xc}}[\tilde{n}(\mathbf{r})]/\delta\tilde{n}(\mathbf{r})$, of the following form:

$$\tilde{V}_{\mathrm{xc}}(\mathbf{r}) = V_{\mathrm{xc}}(\mathbf{r})\tilde{\mathbf{I}} + \mu_B\boldsymbol{\sigma}\cdot\mathbf{B}_{\mathrm{xc}}(\mathbf{r}). \tag{1.24}$$

will enter into K-S equations. Here, $\tilde{\mathbf{I}}$ is the unity 2×2 matrix.

Collinear magnetism

In the case of collinear magnetism, the spin density is assumed to adopt the same direction at each point in space as well as the (possible) external magnetic field. This direction is usually taken as z. The potential matrices in Eq. 1.14 are therefore diagonal and the spin K-S equations are decoupled for purely spin up or spin down wavefunctions:

$$\left[-\frac{\hbar^2}{2m}\nabla^2 + e^2\int\frac{n(\mathbf{r}')}{|\mathbf{r}-\mathbf{r}'|}d\mathbf{r}' + V(\mathbf{r}) - \mu_B\sigma B_z(\mathbf{r}) + V^{\sigma}_{\mathrm{xc}}(\mathbf{r})\right]\phi^{\sigma}_i(\mathbf{r}) = \epsilon_i\phi^{\sigma}_i(\mathbf{r}). \tag{1.25}$$

where σ at the magnetic field term takes $+(-)$ for up (down) equation and $V^{\sigma}_{\mathrm{xc}}(\mathbf{r})$ corresponds to the functional derivative of exchange-correlation energy with respect to the σ part of the diagonal density matrix. All magnetic materials with a collinear magnetic order (i.e. ferromagnetic, antiferromagnetic or ferrimagnetic) can be discribed by Eq. 1.25.

Exchange-correlation functionals

Since the E_{xc} is defined as the difference between the exact energy and other contributions that may be evaluated numerically, the exact E_{xc} functional is complicated and unkown. We start by introducing the simplest and probably the most important parameterization of exchange correlation energy ϵ_{xc} in the local spin density approximation (LSDA) which is based on the homogeneous electron gas:

$$E^{\mathrm{LSDA}}_{\mathrm{xc}}(\mathbf{r}) = \int n(\mathbf{r})\epsilon_{\mathrm{xc}}[n(\mathbf{r}), |\mathbf{m}|]d\mathbf{r}. \tag{1.26}$$

In the framework of LSDA, ϵ_{xc} depends on the electron density and on the magnitude of magnetization. Therefore, in the collinear case it is quite straightforward since the density matrix is $\tilde{n}(\mathbf{r})$ is diagonal. In the homogeneous gas, the analytic expression is known for exchange-energy density but not for correlation-energy density except for the high- and low-density limits. One of the most popular parameterizations is proposed by Perdew and Zunger [32], it consists in interpolating the accurate intermediate values obtained from the quantum Monte Carlo data of Ceperley and Alder [33].

In the case of non-collinear magnetism, we need to diagonalize the $\tilde{n}(\mathbf{r})$ in a local spin axis using the spin one-half rotation matrix (see Eq. 1.27). We introduce the global xyz and local $x''y''z''$ spin axis, for which the exchange-correlation field $\mathbf{B}(\mathbf{r})$ always along the z''. The local spin axis can be achieved from the global one by two steps: i) a new frame $x'y'z'$ is obtained from the global axis by a rotation of ϕ on the z axis, ii) a second rotation of an angle θ on the y' axis gives the local spin axis. Therefore, the change of axis from the global to the local can be defined by the spin one-half rotation matrix:

$$\tilde{U}(\theta,\phi) = \begin{pmatrix} e^{-i\frac{\phi}{2}}\cos\frac{\theta}{2} & -e^{-i\frac{\phi}{2}}\sin\frac{\theta}{2} \\ e^{i\frac{\phi}{2}}\sin\frac{\theta}{2} & e^{i\frac{\phi}{2}}\cos\frac{\theta}{2} \end{pmatrix}. \tag{1.27}$$

So the up and down spin densities $n''_{\uparrow}$, $n''_{\downarrow}$ in the local axis at each point are defined by diagonalizing a non-collinear electron density as follows:

$$\begin{pmatrix} n''_{\uparrow} & 0 \\ 0 & n''_{\downarrow} \end{pmatrix} = \tilde{U}^{\dagger} \begin{pmatrix} n_{\uparrow\uparrow} & n_{\uparrow\downarrow} \\ n_{\downarrow\uparrow} & n_{\downarrow\downarrow} \end{pmatrix} \tilde{U}. \tag{1.28}$$

Once the non-collinear density matrix is diagonalized, the diagonal up and down densities are used to evaluate the exchange-correlation potential.

In contrast, in the gereralized gradient approximation (GGA) the gradients of $n(\mathbf{r})$ and $\mathbf{m}(\mathbf{r})$ have to be considered. hence, in principle it can not be applicable to a non-collinear system. However, since the contribution of $n(\mathbf{r})$ and $\nabla n(\mathbf{r})$ is more important than $\nabla m(\mathbf{r})$, the GGA can be extended in non-collinear case in an approximated way. There are two different parameterizations widely used in terms of gradient of $\mathbf{m}(\mathbf{r})$: i) the gradient of the magnitude of the magnetization $\nabla|\mathbf{m}|$, or ii) the gradient of $\mathbf{m}_z$ in global axis is projected onto the local direction of magnetization. Note that the most significant difference between these two parameterizations can be expected from regions where the magnetization density changes its sign, more details in Ref. [34]. Here, we introduce the latter one as follow,

$$E_{\mathrm{xc}}^{\mathrm{GGA}}(\mathbf{r}) = \int n(\mathbf{r})\epsilon_{\mathrm{xc}}[n(\mathbf{r}), |\mathbf{m}|, \nabla n(\mathbf{r}), \nabla \mathbf{m}_z(\mathbf{r})]d\mathbf{r}. \tag{1.29}$$

where $\nabla \mathbf{m}_z(\mathbf{r})$ can be obtained by using spin one-half rotation matrix in Eq. 1.27 in the case of non-collinear magnetism.

$$\nabla \mathbf{m}_z(\mathbf{r}) \leftarrow \mathrm{Tr}\left\{\tilde{\sigma}_z \tilde{U}^{\dagger}\tilde{n}(\mathbf{r})\tilde{U}\right\}. \tag{1.30}$$

Typically (but not always) the GGA is more accurate than LSDA, i.e. the GGA greatly reduce the bond dissociation energy error, and generally improves transition-state barriers. PW91 [35] and PBE [36] are the most widely used parameterizations of GGA which can be reliably used over a very wide range of materials.

1.1.4 Relativistic corrections and magnetic anisotropy

In relativistic quantum mechanics the free electron, as all particles of spin 1/2, is described by Lorentz invariant Dirac equation [5]:

$$i\hbar\gamma^{\mu}\frac{\partial\phi}{\partial x^{\mu}} = mc\phi, \tag{1.31}$$

where $x^{\mu} = (ct, x, y, z)$ is the 4-vector of time-space coordinates, c is the light velocity and m is the rest mass of electron. The electron wave function ϕ has four-components (Dirac bi-spinor) and γ^{μ} are special 4×4 matrices. In the standard representation they are given by:

$$\gamma^0 = \begin{pmatrix} \mathbf{I} & 0 \\ 0 & -\mathbf{I} \end{pmatrix}, \boldsymbol{\gamma} = \begin{pmatrix} 0 & \boldsymbol{\sigma} \\ -\boldsymbol{\sigma} & 0 \end{pmatrix}, \phi(r,t) = \begin{pmatrix} \psi_1(r,t) \\ \psi_2(r,t) \\ \chi_1(r,t) \\ \chi_2(r,t) \end{pmatrix}. \tag{1.32}$$

with a bi-spinor ϕ composed of (so-called) large and small 2-component spinors, ψ and χ, respectively.

The Dirac equation can be re-written in the form explicitely resolved in time derivative:

$$i\hbar\frac{\partial\phi(r,t)}{\partial t} = H\phi(r,t). \tag{1.33}$$

where H is the Hamiltonian operator:

$$H = c\boldsymbol{\alpha}\cdot\mathbf{p} + \beta mc^2 \tag{1.34}$$

and $\mathbf{p} = -i\hbar\boldsymbol{\nabla}$ are momentum operators. The 4×4 matrices $\boldsymbol{\alpha}$ and β are given by:

$$\beta = \gamma^0 = \begin{pmatrix} \mathbf{I} & 0 \\ 0 & -\mathbf{I} \end{pmatrix}, \boldsymbol{\alpha} = \gamma^0\boldsymbol{\gamma} = \begin{pmatrix} 0 & \boldsymbol{\sigma} \\ \boldsymbol{\sigma} & 0 \end{pmatrix}. \tag{1.35}$$

Consider now an electron moving in external electromagnetic field, created, for example, by nuclei of a crystalline lattice and described in general by a 4-component potential $A^{\mu} = (\Phi, \mathbf{A})$ (Φ is the scalar potential and $\mathbf{A}$ is the vector-potential). The Dirac equation will be altered in the simple Lorentz invariant way:

$$\gamma^{\mu}\left[i\hbar\frac{\partial}{\partial x^{\mu}} - \frac{e}{c}A_{\mu}\right]\phi = mc\phi, \tag{1.36}$$

where e is the (negative) electron charge. The Hamiltonian is modified accordingly:

$$H = c\boldsymbol{\alpha}\left[\mathbf{p} - \frac{e}{c}\mathbf{A}\right] + \beta mc^2 + e\Phi \tag{1.37}$$

The great advantage of using the standard representation (Eq. 1.32) is that the small spinor $\chi \ll \psi$ in the non-relativistic limit (at small particle velocities, $v \ll c$), turning

exactly to zero for a particle at rest ($v \to 0$). This allows to write the Dirac equation for a large 2-component spinor ψ only, expanding formally χ over small parameter $1/c$.

Thus, the fully relativistic Hamiltonian can be written as the sum:

$$H = H^{NR} + \delta H^{(1)} + \delta H^{(2)} + ... \tag{1.38}$$

of non-relativistic Hamiltonian

$$H^{NR} = \frac{1}{2m}\left(\mathbf{p} - \frac{e}{c}\mathbf{A}\right)^2 + e\Phi. \tag{1.39}$$

and relativistic corrections of defferent orders of magnitude with respect to $1/c$.

The first-order correction is the well-known Zeeman term which describes the interaction of particle spin moment with external magnetic field $\mathbf{B} = \text{curl } \mathbf{A}$:

$$\delta H^{(1)} = H^{\text{Zeeman}} = -\mu_B \boldsymbol{\sigma} \cdot \mathbf{B}. \tag{1.40}$$

where $\mu_B = e\hbar/2mc$ is the magneton Bohr. From here it appears that the electron has intrinsic magnetic (spin) moment $\mu_B\boldsymbol{\sigma}$, not related to its orbital motion, interacting with magnetic field.

The second-order terms are the mass-velocity correction, the Darwin shift and the spin-orbit coupling (SOC) term:

$$\begin{aligned} \delta H^{(2)} &= H^{\text{Mass-velocity}} + H^{\text{Darwin}} + H^{\text{SOC}} \\ &= -\frac{p^4}{8m^3c^2} + \frac{e\hbar^2}{8m^2c^2}\Delta\Phi + \frac{e\hbar}{4m^2c^2}(\nabla\Phi \times \mathbf{p}) \cdot \boldsymbol{\sigma}. \end{aligned} \tag{1.41}$$

The first two terms are diagonal in spin index and are therefore called scalar-relativistic corrections while the SOC term is non-diagonal. It couples the electron spin and orbital degrees of freedom and stands at the origin of *magneto-crystalline anisotropy* (MCA).

Another source for magnetic anisotropy arises from the interaction between electrons themselves. From quantum electrodynamics it follows [4] that the interaction Hamiltonian between two electrons i and j has a well-known Coulomb non-relativistic part:

$$U_{ij}{}^{NR} = \frac{e^2}{|\mathbf{r}_i - \mathbf{r}_j|}. \tag{1.42}$$

and relativistic corrections of the second-order over $1/c$. Among the latters is the magnetic dipole-dipole interaction:

$$\delta U^{(2)} = U^{\text{dipole}} = \mu_B^2 \left[\frac{\boldsymbol{\sigma}_i\boldsymbol{\sigma}_j}{r_{ij}^3} - 3\frac{(\boldsymbol{\sigma}_i \cdot \mathbf{r}_{ij})(\boldsymbol{\sigma}_j \cdot \mathbf{r}_{ij})}{r_{ij}^5}\right]. \tag{1.43}$$

where $\mathbf{r}_{ij} = \mathbf{r}_j - \mathbf{r}_i$. This term is of importance for us since it causes the *shape anisotropy* favoring the in-plane alignment of electron magnetic moments on the volume surface. Note that this dipole-dipole interaction is long-range unlike the SOC term localized around atomic cores where electric fields are especially large.

1.1.5 Spin-orbit coupling for a spherically-symmetric field

The spin-orbit coupling (SOC), introduced in the previous section, can be seen as an interaction of the spin moment with the magnetic field experienced by the moving electron. The SOC usually splits states (typically of the order of few to few hundred meV) that are degenerate in a non-relativistic description. In the case of spherically-symmetric potential $\Phi(r)$, as in atom, SOC term can be written as follows:

$$H^{\mathrm{SOC}} = \frac{e\hbar}{4m^2c^2}(\nabla\Phi(\mathbf{r}) \times \mathbf{p}) \cdot \boldsymbol{\sigma} = \frac{\hbar}{4m^2c^2}\frac{1}{r}\frac{dV}{dr}(\mathbf{r} \times \mathbf{p}) \cdot \boldsymbol{\sigma} = \xi(r)\mathbf{L} \cdot \mathbf{S}, \tag{1.44}$$

where $V = e\Phi$ is the electron potential energy, $\mathbf{L} = (\mathbf{r} \times \mathbf{p})/\hbar$ and $\mathbf{S} = \boldsymbol{\sigma}/2$ are the orbital and spin momentum operators, respectively, and

$$\xi(r) = \frac{\hbar^2}{2m^2c^2}\frac{1}{r}\frac{dV}{dr}. \tag{1.45}$$

is the so-called SOC strength constant growing with atomic number of chemical element.

The SOC induces physical phenomena, such as magneto-crystalline anisotropy, the Rashba effect, and it also plays an important role in topological insulators, which have attracted a lot of attention due to their intriguing physics as well as their potential applications in spintronics [37]. If the SOC is included, the total energy of the system depends on the direction of spin moment with respect to the crystallographic axis. Physically, this difference arises due to the crystal field that favors the orbital motion of the electron along preferred direction.

1.1.6 QUANTUM ESPRESSO package

Up to now, the many-body Hamiltonian has been mapped onto a problem of a self-consistent single particle K-S equations within the framework of the Born-Oppenheimer approximation and density functional theory. From the point of view of the numerical scheme, we used the Quantum ESPRESSO (QE) [28] package which is based on DFT, using a plane waves basis (which are orthonormal and energy-independent) to expand the single-particle eigenstates of the K-S equations and pseudopotentials (PPs) [38] to represent electron–ion interactions within the frozen-core approximation. The SOC, crucial for magnetocrystalline anisotropy, is taken into account via fully-relativistic pseudo-potentials (FR-PPs) [39] which are generated by solving the atomic Dirac equation for the larger 2-component spinor ψ (as outlined in Section 1.1.4) for each atomic type.

By introducing pseudopotentials (PPs) we are able to remove core electrons from the calculation and replace the real valence wavefunctions by the so-called pseudo wavefunctions which match exactly the true real wavefunctions outside the core radius but are nodeless inside. Norm-conserving [40] and ultrasoft [41] are the two most common forms of pseudopotentials used in *ab initio* calculations. In this PhD thesis, we have used the latter one which allows to reduce substantially the plane wave cutoff energy in the calculations.

The PPs can be split into a local part $V^{\text{loc}}(\mathbf{r})$ and a non-local part V^{NL}. In the case without spin-orbit coupling, the non-local part of the PP can be written by introducing projectors on the well defined orbital angular momentum l at each atomic site i:

$$V^{\text{NL}} = \sum_i \sum_{l,m} D^i_{l,m} |\beta^i_l Y^i_{l,m}\rangle\langle\beta^i_l Y^i_{l,m}|, \tag{1.46}$$

where β^i_l, $Y^i_{l,m}$, $D^i_{l,m}$ are radial components of projector functions, spherical harmonics and pseudopotential coefficients, respectively. This spin-independent pseudopotential can be constructed at the scalar relativistic level but does not include the spin-orbit coupling.

If the SOC is included, the well defined quantum number is the total angular momentum, j. The spin-angle functions are introduced to project into states of j about each atom so that:

$$V^{\text{NL, SOC}} = \sum_i \sum_{l,j,m_j} D^i_{l,j,m_j} |\beta^i_{l,j} \tilde{Y}^i_{l,j,m_j}\rangle\langle\beta^i_{l,j} \tilde{Y}^i_{l,j,m_j}|, \tag{1.47}$$

where $\beta^i_{l,j}$ (as above) are radial functions and $\tilde{Y}^i_{l,j,m_j}$ are spin-angle functions, corresponding to (l, j, m_j) quantum numbers. This PP is a 2×2 matrix of operators acting on two-component spinor wavefunctions and includes both scalar relativistic and SOC effects. The spin-angle functions $\tilde{Y}^i_{l,j,m_j}$ are

$$\tilde{Y}^i_{l,j,m_j} = \begin{pmatrix} \left(\frac{l+m+1}{2l+1}\right)^{1/2} Y_{l,m} \\ \left(\frac{l-m}{2l+1}\right)^{1/2} Y_{l,m+1} \end{pmatrix} \quad , \quad \tilde{Y}^i_{l,j,m_j} = \begin{pmatrix} \left(\frac{l-m+1}{2l+1}\right)^{1/2} Y_{l,m-1} \\ -\left(\frac{l+m}{2l+1}\right)^{1/2} Y_{l,m} \end{pmatrix}, \tag{1.48}$$

for $j = l + 1/2$ where $m = m_j - 1/2$ and $j = l - 1/2$ where $m = m_j + 1/2$, respectively. Next, one can rewrite Eq. 1.47 by making use of Clebsch-Gordan coefficients, for more details see Ref. [39]. This way one finally arrives at:

$$V^{\text{NL, SOC}} = \sum_i \sum_{l,j,m,m'} D^{i,\sigma,\sigma'}_{l,j,m,m'} |\beta^i_{l,j} Y^i_{l,m}\rangle\langle\beta^i_{l,j} Y^i_{l,m'}|. \tag{1.49}$$

where both $-l < m < l$ and $-l < m' < l$. Now the projectors are written in terms of usual spherical harmonics as in the scalar relativistic case but with PP coefficients which are now spin-dependent.

1.2 Magnetic Tight-Binding model

Although DFT is very successful to describe the electronic structure, one of the problem is the required computational time, which remains a challenge for large systems, i.e. some thousands of atoms per supercell. Using semi-empirical tight binding method, the more realistic systems can be feasible with the parameters obtained by *ab initio* calculations. Here, we describe the main ingredients of our magnetic TB model, more details can be found in our previous work [18, 26, 27].

1.2.1 Tight-Binding Hamiltonian

As in DFT, we are lead to solve one-electron Schrödinger equation:

$$H|\Psi\rangle = E|\Psi\rangle. \tag{1.50}$$

In the tight-binding (TB) model of electronic structure, the wavefunction can be expanded in a non-orthogonal atomic basis set,

$$|\Psi\rangle = \sum_{i\lambda} C_{i\lambda}|i\lambda\rangle. \tag{1.51}$$

where λ represent the s, p and d atomic orbitals centered at each site i, in general, we consider only the valence eletrons which mainly contribute to the chemical bonding.

If we write the Schrödinger equation with a wavefunction given by Eq. 1.51, it leads to a matrix equation of the form:

$$\tilde{H}\mathbf{C} = \epsilon\tilde{S}\mathbf{C}. \tag{1.52}$$

where $\tilde{H}$ and $\tilde{S}$ are the Hamiltonian and overlap matrices while $\mathbf{C}$ is the vector bulit from the coefficients $C_{i\lambda}$. The eigenvalue ϵ form the so-called band-structure of the crystal.

Let us now write down the matrix elements of the Hamiltonian,

$$H_{i\lambda j\mu} = \langle i\lambda|H|j\mu\rangle = \langle i\lambda|T + \sum_i V_i^{\mathrm{at}}|j\mu\rangle. \tag{1.53}$$

Here the effective potential is approximated by the sum of isolated neutral atomic-like potentials.

The diagonal matrix elements (i=j) can be written as:

$$H_{i\lambda i\mu} = \epsilon_{i\lambda}^{\mathrm{at}}\delta_{\lambda\mu} + \langle i\lambda|\sum_{k\neq i} V_k^{\mathrm{at}}|i\mu\rangle. \tag{1.54}$$

The first term corresponds to the on-site orbital levels and the second one is the so-called crystal filed integral which is often ignored in practice.

The off-diagonal matrix elements ($i \neq j$) are given by,

$$H_{i\lambda j\mu} = \epsilon_{j\mu}^{\mathrm{at}} S_{i\lambda j\mu} + \langle i\lambda|V_i^{\mathrm{at}}|j\mu\rangle + \langle i\lambda|\sum_{k\neq i,j} V_k^{\mathrm{at}}|j\mu\rangle. \tag{1.55}$$

The first two terms describe the two-center integrals and we neglect the three-center integrals (the last trem) since their contribution is much smaller than the two-center ones. The two-center integrals are the so-called hopping integrals $\beta_{i\lambda j\mu}$ which measure the ability of electrons to hop from one site to another. Due to the spherical symmetry of the atomic potentials, the hopping elements of the Hamiltonian can be described with 10 types of Slater-Koster parameters and we introduce a cutoff since the hopping integrals decrease exponentially with respect to distance between atoms.

The TB Hamiltonian expands the eigenstates of a systems in terms of a non-orthogonal orbital basis and contains three types of parameters: on-site patameters, hopping parameters and the overlap patameters. The Mehl and Papaconstantopoulos's parameterization

procedure [42] is used by fitting the total energies and band structure of non-magnetic systems to reproduce *ab initio* calculations (or experimental results) over a wide range of intraatomic distances and various crystallographic structures.

1.2.2 Local charge neutrality

Since the parameterized TB Hamiltonian is given by a non-self-consistent scheme, this could lead to a large charge transfer in inhomogeneous systems (i.e. vacancy, slab or cluster etc). A constraint technique is used to maintain the same charge for every site by adding a penalizaion term to the total energy.

$$E^{\text{tot}} = E^{\text{tot},0} + E^{\text{LCN}} = E^{\text{tot},0} + \sum_i \frac{U_i^{\text{LCN}}}{2}(N_i - N_i^0)^2. \tag{1.56}$$

where U^{LCN}, N_i and N_i^0 are the local charge neutrality constant, the Mulliken charge and the charge that we want to impose on site i, respectively. The value of U^{LCN} should be large enough to ensure $N_i \approx N_i^0$, in practice, we take $U^{\text{LCN}} = 20$ eV.

In the case of orthogonal basis set, if we minimize the total energy with this penalization term, it leads to a similar eigenvalue equation where the constraint for the charge neutrality modifies the on-site energies,

$$H_{i\lambda j\mu} = H^0_{i\lambda j\mu} + U_i^{\text{LCN}}(N_i - N_i^0)\delta_{i\lambda j\mu}. \tag{1.57}$$

For a non-orthogonal basis set the charge is replaced by Mulliken charge and the Eq. 1.57 can be generalized as follows:

$$H_{i\lambda j\mu} = H^0_{i\lambda j\mu} + \left[\frac{U_i^{\text{LCN}}}{2}(N_i - N_i^0) + \frac{U_j^{\text{LCN}}}{2}(N_j - N_j^0)\right] \cdot S_{i\lambda j\mu}. \tag{1.58}$$

Since the local charge neutrality term in the Hamiltonian now depends on the local charge and the charges themselves are calculated from the eigenstates of the Hamiltonian, this equation must be solved self-consistently. And finally, if we compare the band energy obtained by a diagonalization of Hamiltonian including the local charge neutrality with Eq. 1.56, there is a double counting term which should be considered.

$$E^{\text{tot}} = E^{\text{band}} - E^{\text{dc}} = \sum_\alpha f_\alpha \epsilon_\alpha - \sum_i \frac{U_i^{\text{LCN}}}{2}[N_i^2 - (N_i^0)^2]. \tag{1.59}$$

where f_α is the Fermi-Dirac occupation of state α and ϵ_α is the eigenstate of the "corrected' Hamiltonian.

1.2.3 Stoner model

Until now, the parameterized TB Hamiltonian is spin independent, here we introduce a simple model proposed by Stoner [43, 44] to remove the spin degeneracy. In the Stoner

model, an extra term which describes the electron-electron interaction is added to the total energy of the non-magnetic system $E^{\mathrm{tot},0}$.

$$E^{\mathrm{tot}} = E^{\mathrm{tot},0} - \sum_i \frac{I_{i\lambda}}{4} M_{i,d}^2. \tag{1.60}$$

where the $M_{i,d}$ is the spin moment of d orbitals. The minimization of E^{tot} leads to a modified Hamiltonian. The modification of electronc levels for spin up and down is described by the exchange splitting that depends on the spin moment on site i, m_i and the Stoner parameter for $i\lambda$ orbital, $I_{i\lambda}$,

$$\epsilon_{i\lambda\sigma} = \epsilon^0_{i\lambda} - \frac{1}{2} I_{i\lambda} M_{i,d} \sigma. \tag{1.61}$$

where $\sigma = 1$ for spin up while $\sigma = -1$ for spin down. Since the exchange splitting of s and p orbitals is much smaller than d orbital, the s and p components of Stoner parameter are taken as $I_s = I_p = I_d/10$ [18]. Note that the spin moment is originated mainly from $3d$ orbitals in the transition metals (i.e. Fe, Co and Ni etc). We can derive easily the Stoner criterion, $I \cdot D(E_F) > 1$, by minimizing the total energy, where $D(E_F)$ is the density of states (DOS) at the Fermi energy.

Let us write the Stoner potential $V^{\mathrm{Stoner}}_{i\lambda j\mu}$,

$$V^{\mathrm{Stoner}}_{i\lambda\sigma, j\mu\sigma'} = -\frac{\sigma}{2} (I_{i\lambda} M_{i,d}) \delta_{ij} \delta_{\lambda\mu} \delta_{\sigma\sigma'}. \tag{1.62}$$

where $I_{i\lambda}$ is the Stoner parameter on the site i and orbital λ, and M_i is the ith site magnetic moment.

In the case of collinear magnetism, the Stoner potential matrix is diagonal in its local spin frame, therefore, it modifies exclusively the on-site energies of system.

$$\widetilde{V}^{\mathrm{Stoner\text{-}loc}}_{i\lambda j\mu} = -\frac{1}{2} I_{i\lambda} (M_{i,d} \sigma_z) \delta_{ij} \delta_{\lambda\mu}. \tag{1.63}$$

where $\hat{\sigma}_z$ is the z component of Paulli matrix.

As we described in the Sec. 1.1.3, it is straightforward to obtain the Stoner potential in the global frame in the non-collinear case,

$$\widetilde{V}^{\mathrm{Stoner\text{-}glo}}_{i\lambda j\mu} = -\frac{1}{2} I_{i\lambda} (\mathbf{M}_{i,d} \cdot \boldsymbol{\sigma}) \delta_{ij} \delta_{\lambda\mu}. \tag{1.64}$$

As in the case of the local charge neutrality, the total energy should be corrected by so-called double counting term arising from Stoner term.

$$E^{\mathrm{tot}} = E^{\mathrm{band}} - E^{\mathrm{dc}} = \sum_\alpha f_\alpha \epsilon_\alpha + \sum_i \frac{I_{i\lambda}}{4} M_{i,d}^2. \tag{1.65}$$

The value of the Stoner parameter I_d is determined by reproducing *ab initio* data of the spin magnetization of bulk systems with respect to the lattice constant. We set $I_s = I_p = I_d/10$ since the magnetization is dominated by d orbitals in the transition metals. The optimal values of I_d are 0.88 and 1.10 eV for Fe and Co, respectively.

1.2.4 Spin-orbit coupling

The SOC is of relativistic nature and couples the electron spin with its own orbital motion, it is given for a spherical potential,

$$V^{\mathrm{SOC}} = \xi(r) \cdot \mathbf{L} \cdot \mathbf{S}. \tag{1.66}$$

with $\mathbf{L} = (\mathbf{r} \times \mathbf{p})/\hbar$ the angular momentum, $\mathbf{S} = \boldsymbol{\sigma}/2$ the spin operator and the radical-dependant function $\xi(r)$ is given by,

$$\xi(r) = \frac{\hbar^2}{2m^2c^2} \frac{1}{r} \frac{dV}{dr}. \tag{1.67}$$

Using $\langle \mathbf{r}|i\lambda\rangle = R_{i\lambda}(r) \cdot Y_{i\lambda}(\theta, \phi)$ where $R_{i\lambda}(r)$ and $Y_{i\lambda}(\theta, \phi)$ are the radical and spherical harmonic functions, respectively, we can write the matrix elements of SOC potential as follows,

$$V^{\mathrm{SOC}}_{i\lambda\sigma, j\mu\sigma'} = \xi_{i\lambda\mu} \langle \bar{\lambda}\sigma|\mathbf{L} \cdot \mathbf{S}|\bar{\mu}\sigma'\rangle \delta_{ij} = \xi_{i\lambda\mu} \langle \bar{\lambda}|\mathbf{L}|\bar{\mu}\rangle \langle \sigma|\mathbf{S}|\sigma'\rangle \delta_{ij}. \tag{1.68}$$

where $\bar{\lambda}$ and $\bar{\mu}$ are the angular parts of the atomic orbital. Since $\xi_i(r)$ is localized near $r = 0$ and $\langle \bar{\lambda}|\mathbf{L}|\bar{\mu}\rangle$ is block-diagonal for s (it is zero), p and d orbitals, the spin-orbit constant $\xi_{i\lambda}$ is determined by only two parameters:

$$\xi_{i\lambda} = \int_0^\infty R^2_{i\lambda}(r) \xi_i(r) r^2 dr, \ \lambda = p \text{ or } d. \tag{1.69}$$

The spin-orbit constant for d orbital is determined by comparaison with *ab initio* band structure including SOC and we found that 60 and 80 meV are very good estimates for Fe and Co, respectively. In practice, we ignore the p component of SOC constant since the effect is negligible in most physical phenomena.

Summary of magnetic tight-binding model

In summary, our magnetic TB Hamiltonian in a non-orthogonal s, p and d atomic-like basis is written as a sum of four terms,

$$H = H^{\mathrm{TB}} + H^{\mathrm{LCN}} + H^{\mathrm{Stoner}} + H^{\mathrm{SOC}}. \tag{1.70}$$

where H^{TB} is a standard "non-magnetic" TB Hamiltonian, the form of which is very similar to the one introduced by Mehl and Papaconstantopoulos. This Hamiltonian contains three terms: the on-site atomic levels, the hopping integrals and overlap integrals which are written as analytic functions depending on a set of parameters. H^{LCN} is a term ensuring local charge neutrality and H^{Stoner} is the Stoner-like contribution, modifying the on-site levels, that controls the spin magnetization. In addition, H^{SOC} is also on-site Hamiltonian corresponding to the spin-orbit coupling.

CHAPTER 2

Magnetic anisotropy

In this chapter, we first introduce the different approaches widely used in the literature to calculate the magnetic anisotropy, in particular, we emphasise on the so-called force theorem which is used in this PhD study. Next we will give the implementation details of the force theorem in the tight binding code as well as in the plane-wave DFT package QUANTUM ESPRESSO. We will show that, the so-called grand canonical force theorem is the most suited to describe the local quantities of MCA.

Magnetic anisotropy is one of the most important properties of magnetic materials due to their tremendous technological applications for spintronics devices [37]. In last decades, higher storage densities were achieved by reducing the magnetic grains down to nanoscale. However, the magnetic stability of a nano-object decreases proportionally to its size and the ultimate limit is reached when thermal fluctuations overcome the energy barrier to switch the global magnetization of the system. For example the thermal stability of small nanocrystals with respect to magnetization reversal is controled by the height of the energy barrier to overcome during the switching process of the magnetization. The most crucial issue in exploring ultimate density data storage, i.e. high-density magnetic recording [1, 2], is the magnetic anisotropy energy (MAE), which is characterized by the dependence of the energy of a magnetic system on the orientation of its magnetization. The orientation corresponding to the minimum of energy (so-called easy axis) determines the magnetization direction at low temperature. With the recent developement of nanotechnology fabrication techniques, the search for materials with large uniaxial anisotropy and high structure stability has been very intensive for spintronics applications.

The origin of MAE contains two different parts, both of them are due to relativistic effects: i) The first part is the so-called shape anisotropy related to the macroscopic shape

and it is originated from the Breit interaction [4] but usually ascribed to the classical long-range magnetic dipole-dipole interactions, ii) The second one is referred to as magnetocrystalline anisotropy (MCA) determined by the crystal structure and composition and originates from the spin-orbit coupling (SOC).

2.1 Shape anisotropy

Suppose $\mathbf{m_i}$ and $\mathbf{m_j}$ are two magnetic moments separated by a distance of r_{ij} in space, the dipolar energy comes from the magnetic dipole-dipole interaction and can be written as follow:

$$E_{\text{dip}} = \frac{\mu_0}{8\pi} \sum_{i \neq j} \frac{1}{r_{ij}^3} \left[\mathbf{M_i} \cdot \mathbf{M_j} - 3 \frac{(\mathbf{r_{ij}} \cdot \mathbf{M_i})(\mathbf{r_{ij}} \cdot \mathbf{M_j})}{r_{ij}^2} \right]. \tag{2.1}$$

where μ_0 is the magnetic constant and the magnetic moment is in units of the Bohr magneton (μ_{B}). The second term in the dipolar interaction shows clearly that the dipole energy depends on the orientation of the magnetic moments $\mathbf{M_i}$, $\mathbf{M_j}$ with respect to $\mathbf{r_{ij}}$.

When all magnetic moments are parallel, E_{dis} may be rewritten as,

$$E_{\text{dip}} = \frac{\mu_0}{8\pi} \sum_{i \neq j} \frac{M_i M_j}{r_{ij}^3} (1 - 3\cos^2 \theta_{ij}). \tag{2.2}$$

where θ_{ij} is the angle beween the direction of the magnetic moment and the vector connecting atoms i and j. Therefore, if the magnetization points parallel to r_{ij}, the E_{dip} is the lowest. Therefore it costs energy to rotate the two dipole moments perpendicular to the the r_{ij}-axis.

The shape anisotropy essentially depends on the global shape of the sample and it usually favors magnetization along elongated directions of the sample, i.e., it favors in-plane anisotropy in films. Since the shape anisotropy is of a classical origin, it needs not to be included in electronic calculation and can be added *a posteriori* by summing all pairs of magnetic dipole-dipole interaction energies.

2.2 Magneto-crystalline anisotropy

As stated before, the origin of the MCA is the SOC, it is a quantum effect of relativistic nature that breaks the rotational invariance with respect to the spin quantization axis. Therefore, if the SOC is included, the energy of the system depends on the orientation of the spin with respect to the crystallographic axes. There are several different methods to calculate the MCA in the literature: i) self-consistent scheme [12], ii) force theorem [13, 14, 21], iii) perturbation treatement [15, 16], iv) Bruno formula [17] and v) other methods such as empirical Neel-like model [24] for large-scale systems and torque method [23] for systems with uniaxial symmetry. There are evidences of achieving similar results for most of the $3d$ transition metals.

2.2.1 Self-consistent scheme

The calculation of MCA through the self-consistent scheme is based on the direct calculation of the total energy difference of the two different magnetization directions with spin-orbit coupling, which is included in the K-S equation in the presence of the self-consistent full-relativistic potential. It has the following form

$$\mathrm{MCA} = E^{\mathrm{tot}}[\hat{\mathbf{m}}_1] - E^{\mathrm{tot}}[\hat{\mathbf{m}}_2]. \tag{2.3}$$

where $\hat{\mathbf{m}}_1$ and $\hat{\mathbf{m}}_2$ are the two different orientations of magnetization. In principle, this approach is "exact" and straightforward. However, it is the most computationally demanding since it usually necessitates a long self-consistent filed (SCF) loop that implies the diagonalization of large matrices including SOC, so it is called as "brute force method". On the other hand, the SCF with SOC is hard to converge since it requires a well-converged charge density or potential. One should use penalization techniques to obtain $E^{\mathrm{tot}}[\hat{\mathbf{m}}]$ for any spin configuration. Therefore, assessing the MCA for systems containing hundreds of atoms by this approach is especially challenging.

2.2.2 Force theorem

As we mentioned above the MCA is defined as the fully relativistic total energy difference between two different magnetization directions. However, if the modification of the potential induced by SOC is small as in the case of the Fe- and Co-based systems, the so-called force theorem (FT) [13, 14, 21] is applied. The MCA is taken as the band energy difference (instead of the total energy difference) obtained after a one-step diagonalization of the full Hamiltonian including SOC, starting from the well converged self-consistent scalar relativistic (without SOC) density/potential. The band energy difference between two spin orientations $\hat{\mathbf{m}}_1$ and $\hat{\mathbf{m}}_2$ can be written as follow,

$$\mathrm{MCA}^{\mathrm{FT}} = E^{\mathrm{band}}[\hat{\mathbf{m}}_1] - E^{\mathrm{band}}[\hat{\mathbf{m}}_2] = \int^{E_F^1} E n_1(E) dE - \int^{E_F^2} E n_2(E) dE. \tag{2.4}$$

here $n_1(E)$ and $n_2(E)$ are the density of states and E_F^1 and E_F^2 are the Fermi level of the configurations $\hat{\mathbf{m}}_1$ and $\hat{\mathbf{m}}_2$, respectively. The Fermi levels are determined by the condition on the total numbers of electrons N in the system:

$$N = \int^{E_F^1} n_1(E) dE = \int^{E_F^2} n_2(E) dE. \tag{2.5}$$

It should be noted that the FT leads to not only a considerable saving of the computational cost but is also numerically very stable since the self-consistent effect including SOC is ignored. Therefore, only one iteration is needed for the perturbed systems, which is also kown as "one-shot-calculation".

It is important to note that the band energy is a summation of the eigenvalues over the occupied states (at fixed number of electrons). Therefore a small variation of Fermi energy is expected with respect to the non perturbed system as follows:

$$E_F^1 = E_F + \delta_1 \quad \text{and} \quad E_F^2 = E_F + \delta_2 \tag{2.6}$$

where E_F is the Fermi level of the non-perturbed system. At linear order the variation of band energy can be written

$$\mathrm{MCA}^{\mathrm{FT_{gc}}} = \int^{E_F} E\Delta n(E)dE + E_F(\delta_1 n_1(E_F) - \delta_2 n_2(E_F)) \tag{2.7}$$

where $\Delta n(E)$ is the variation of the charge difference between two different spin configurations. Explicitly, $\Delta n(E) = n_1(E) - n_2(E)$.

Using the conservation of the total number of electrons it comes that

$$\mathrm{MCA}^{\mathrm{FT}} \approx \mathrm{MCA}^{\mathrm{FT_{gc}}} = \int^{E_F} (E - E_F)\Delta n(E)dE \tag{2.8}$$

The $\mathrm{FT_{gc}}$ formulation seems very similar to the standard FT formulation, but it leads to very different "space" partition of the energy. The underlying reason can be found in the type of statistical ensemble: canonical for FT and grand-canonical for $\mathrm{FT_{gc}}$. The grand-canonical ensemble for which the "good" variable is the Fermi energy (and not the total number of electrons) is better suited for a spatial partition of the energy [45]. For example the Gibbs construction [46] to define properly surface quantities is based on a grand-canonical ensemble. Within this approach the suitable potential is the so-called grand-potential $\Omega = E_\mathrm{b} - E_F N$. This formalism can be generalized at finite temperature [45, 47]. Since the first-order variation of the Helmholtz Free Energy ($F = E^{\mathrm{band}} - TS_e$) at constant electron-number is equal to the fisrt order variation of the grand-potential at constant chemical potential the FT and $\mathrm{FT_{gc}}$ formulation are equivalent in terms of variation of total energy. However the spatial repartition of energy could be very different within these two approaches, this point will be explained in the next section.

2.2.3 Perturbation treatment

When the SOC is small (as in the $3d$ transition metals) the relation between the electron occupation and MCA can be written in the framework of second order perturbation theory [15, 16]:

$$\mathrm{MCA} = E_z - E_x \approx \xi^2 \sum_{u,o,\sigma,\sigma'} \left[\frac{|\langle u^\sigma|\mathbf{L}_z|o^{\sigma'}\rangle|^2 - |\langle u^\sigma|\mathbf{L}_x|o^{\sigma'}\rangle|^2}{\epsilon_u^\sigma - \epsilon_o^{\sigma'}} \right]. \tag{2.9}$$

Here ξ is the SOC constant, ϵ_u^α and ϵ_o^β are the energy levels of the unoccupied states with spin σ ($|u^\sigma\rangle$) and occupied states with spin σ' ($|o^{\sigma'}\rangle$), respectively. One should note that due to time-reversal symmetry of the non-perturbed states, the diagonal elements of

SOC matrix is zero, therefore the energy shift of all states is identically zero in the first order of perturbation.

Since the MCA is inversely proportional to the energy difference between unoccupied and occupied states, the most important contributions to the MCA can be expected in the case of one state is placed just below and another one just above the Fermi level.

2.2.4 Bruno formula

The orbital moment is a quantity essentially related to the SOC and to the MCA in magnetic systems. It is well known that the easy axis always corresponds to the direction where the orbital moment is the largest. Bruno formula [17] is based on a perturbative treatment with an additional approximation: neglecting spin-flip terms (applicable when exchange splitting is substantial). In this treatment the orbital moment anisotropy is proportional to the MCA. This model works well for strong magnets such as Co due to the lack of unoccupied spin-up d states.

$$\mathrm{MCA}_i \approx -\frac{\xi_i}{4}[\langle \mathbf{L}_i^1 \rangle - \langle \mathbf{L}_i^2 \rangle]. \tag{2.10}$$

where $\langle \mathbf{L}_i^1 \rangle$ and $\langle \mathbf{L}_i^2 \rangle$ are the orbital moments on site i along the spin magnetization direction of 1 and 2, respectively.

However, when the spin-flip contributions become important, such as in the case of large SOC, then a simple correspondence between MCA and orbital moment is not valid anymore [20], we have to consider also contributions from the spin-flip processes and a more exact expression could be found in Ref. [22].

2.3 Force Theorem: practical implementations

In this section we will illustrate the implementation details of the MCA calculations by the force theorem in our magnetic tight-binding code [18, 26, 27] as well as in the plane-wave DFT electronic structure package QUANTUM ESPRESSO [28].

2.3.1 Tight-binding model

Let us now consider the effect of a perturbative external potential δV^{ext} which in our case is the SOC. This external potential will induce a total potential variation $\delta V = \delta V^{\mathrm{ext}} + \delta V^{\mathrm{ind}}$ where δV^{ind} is the potential variation provoked by the modification of on site levels in the perturbed system due to self-consistent effects. Within our model δV^{ind} is simply related to the variation δN_i and δM_i of the charge and magnetic moment thus,

$$\delta V^{\mathrm{ind}} = \sum_{i,\lambda,\sigma} |i,\lambda,\sigma\rangle \Big[U_i^{\mathrm{LCN}} \delta N_i - \frac{I_{i\lambda}}{2} \delta M_i \sigma \Big] \langle i,\lambda,\sigma|, \tag{2.11}$$

The variation of the band energy due to $\delta V^{\rm ind}$ can be straighforwardly calculated from the first order pertubration expansion:

$$\sum_{\alpha} f_{\alpha}\langle\alpha|\delta V^{\rm ind}|\alpha\rangle = \sum_{i} U_i^{\rm LCN} N_i \delta N_i - \sum_{i} \frac{I_{i\lambda}}{2} M_i \delta M_i, \tag{2.12}$$

This variation is exactly compensated (to linear order) by its corresponding double counting term and therefore the change of the total energy is equal to the change of band energy induced by the external potential only, leading to the so-called force theorem:

$$\Delta E^{\rm tot} \approx \Delta E^{\rm FT}_{\rm band} = \Delta\Big[\sum_{\alpha} f_{\alpha}\epsilon_{\alpha}\Big]. \tag{2.13}$$

where $\Delta E^{\rm FT}_{\rm band}$ is calculated by ignoring the self-consistent corrections. This means that the eigenvalues of the perturbed system are obtained by a one-step diagonalization of $H^{\rm TB} + \delta V^{\rm ext}$. The force theorem leads to a considerable saving in the computational cost, and it is also often more presise than the full self-consistent calculations with SOC. In systems containing "light" atoms like Fe or Co for which the spin-orbit coupling constant ξ_d is modest (≈ 60 meV) it is expected that the force theorem should work very well.

Indeed, within the force theorem the total energy difference is approximated as the difference of the single particle energies, this type of the calculation is performed in three steps: i) a first collinear self-consistent filed calculation without SOC for which the density matrix is diagonal in spin space, ii) a global rotation of the density matrix to "prepare" it in the right spin direction, and iii) a one step noncollinear non-self-consistent calculation including SOC.

In order to check the validity of the force theorem, we have performed a series of calculations for ultrathin layer of bcc-Fe(001) with various thicknesses ranging from one to twenty atomic layers, within the full SCF with SOC and FT approaches. The lattice parameter of bcc-Fe(001) $a_0 = 2.85$ Å found from *ab initio* calculations (which is close to the experimental value of $a_0 = 2.86$ Å) and no atomic relaxations were performed. Note that the MCA is obtained as band energy difference for spin magnetization which is perpendicular or parallel to the atomic slabs. Explicitely, MCA $= E^{\rm band}_{\perp} - E^{\rm band}_{\parallel}$. A mesh of 50×50 in-plane k-points has been used for SCF calculations without SOC within a Marzari-Vanderbit smearing parameter of 50 meV. In the non-SCF calculations with SOC the mesh was increased to 80×80 and the smearing parameter was reduced to 10 meV in order to provide a precision below 10^{-2} meV. The MCA obtained by these two methods differ by less than 10^{-2} meV proving the validity of FT approach (two curves almost superpose), which will be used systematically in the rest of the calculations. For more details about the convergence tests of force theorem, please see ANNEXE A.

So far we have only considered variations of total energies but it is also very instructive to investigate the local density of energy. Let us write the MCA as a sum of atomic-like contribution within FT and $\rm FT_{gc}$ approaches:

$$\rm MCA^{FT} = \sum_{i} \left[\int^{E_F^{\perp}} E n_i^{\perp}(E) dE - \int^{E_F^{\parallel}} E n_i^{\parallel}(E) dE \right] \tag{2.14}$$

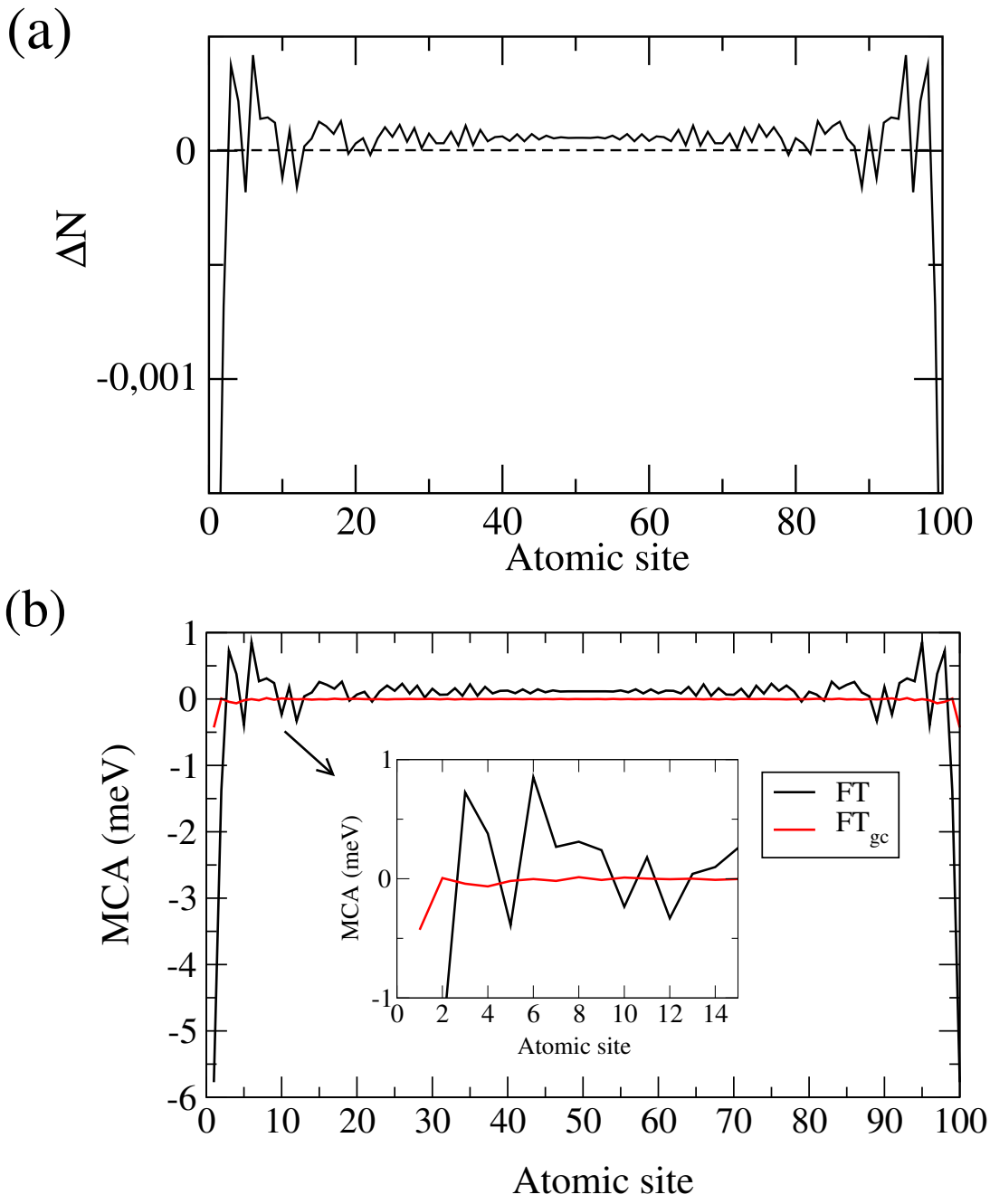

Figure 2.1: a) Variation of the charge difference $\Delta N_i = (N_i^{\perp} - N_i^{\parallel})$ between out-of-plane and in-plane magnetic configurations (obtained after one diagonalization) on successive atomic layers of a Fe(001) slab containing $N = 100$ layers. b) Layer resolved MCA of the Fe(001) slab calculated with two different methods: canonical FT (black lines) and grand canonical $\mathrm{FT_{gc}}$ (red lines). The zoom over the first 15 layers is shown in the inset. Positive (negative) MCA values mean in-plane (out-of-plane) eaxy-axis direction.

$$\mathrm{MCA}^{\mathrm{FT_{gc}}} = \sum_i \left[\int^{E_F} (E - E_F) \Delta n_i(E) dE \right] \tag{2.15}$$

where $n_i^{\perp}(E)$ and $n_i^{\parallel}(E)$ are the density of states on atom i for perpendicular or in-plane magnetization direction, respectively, and $\Delta n_i(E) = n_i^{\perp}(E) - n_i^{\parallel}(E)$. $E_F^{\perp}$ and $E_F^{\parallel}$ are the corresponding Fermi energies and E_F is the Fermi level of the collinear self-consistent calculation without SOC.

In order to check the difference between FT and $\mathrm{FT_{gc}}$ formulations in terms of local decomposition the layer-resolved MCA per Fe atom a bcc-Fe(001) slab of 100 layers is plotted in Fig. 2.1 (b). The most striking result is the very large oscillating behaviour which persists very deeply into the bullk for the FT method. In addition, the local MCA obviously does not converge toward the expected bulk value which in this case should be exactly zero (since the three cubic axis are equivalent). In contrast, the layer resolved MCA obtained from the $\mathrm{FT_{gc}}$ method corresponds to the behaviour expected from a proper local quantity, namely a dominant variation in the vicinity of the surface that attenuates rapidly when penetrating in the bulk. This is indeed the case since only the surface atomic layer is strongly perturbed. In fact there are slight oscillations over the five first outer layers and an almost perfect convergence towards the bulk value for deeper layers. It is then clear that $\mathrm{FT_{gc}}$ is the appropriate method to define a layer resolved MCA. Note, however, that the total MCA are almost strictly indentical for FT and $\mathrm{FT_{gc}}$. Finally, it is very interesting to point out a striking analogy that exists with the simple one-dimensional free-electron model discussed in the ANNEXE B.

It is also useful to note the relation between Eq. 2.14 and Eq. 2.15 in order to understand the difference between the two methods:

$$\mathrm{MCA}_i^{\mathrm{FT_{gc}}} = \mathrm{MCA}_i^{\mathrm{FT}} - E_F(N_i^{\perp} - N_i^{\parallel}) \tag{2.16}$$

where $N_i^{\perp}$ and $N_i^{\parallel}$ are the Muliken charges on atom i for perpendicular or in-plane magnetization, respectively.

When summed over all the atoms of the system the additionnal term, $E_F(N^{\perp} - N^{\parallel})$, disappears since the total number of electrons is preserved and we recover the equivalence between FT and $\mathrm{FT_{gc}}$ for total energy differences. This formula is quite instructive since it shows that the difference between FT and $\mathrm{FT_{gc}}$ is related to the slight charge redistribution between the two magnetic configurations. At the first sight it seems that FT and $\mathrm{FT_{gc}}$ should lead to very similar decomposition of the energy since the local charge neutrality term is supposed to avoid charge transfers and therefore $\Delta N_i = N_i^{\perp} - N_i^{\parallel} \approx 0$, but one should bear in mind that the force theorem applies only if self-consistency effects are ignored and therefore larger charge redistributions may appear. They produce irrelevant (to magnetic anisotropy) contributions $E_F \Delta N_i$ to the local anisotropy energy which should be substracted as it is accomplished in the $\mathrm{FT_{gc}}$ approach. In Fig. 2.1 (a) we show ΔN^i which indeed looks very similar in shape to the FT layer resolved MCA and, when substracted, leads thus to well behaved $\mathrm{FT_{gc}}$ layer resolved MCA curve.

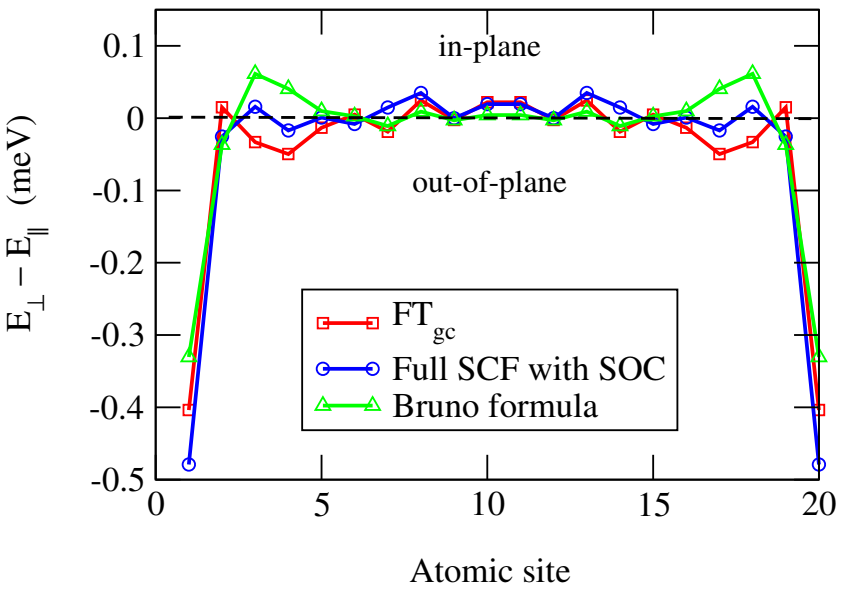

Figure 2.2: Layer-resolved MCA of the Fe(001) slab with $N = 20$ layers calculated using FT_{gc} approximation (red squares), full self-consistent calculation with SOC (blue circles) and the Bruno formula (green triangle ups). Note that the layer-resolved spin-projected orbital moments are obtained by self-consistent calculations.

These arguments show that the local variation of band energy should be the same after a self-consistent calculation provided that the local charge neutality is achieved. To check this point we plot in Fig. 2.2 the layer-resolved MCA for a Fe(001) slab of 20 layers with full SCF calculation with SOC (blue circles) and FT_{gc} method (red squares). Note that in the case of the full SCF approach one should consider the variation of the total energy wich includes band energy as well as double counting terms. In our TB scheme the double counting terms can easily be decomposed as a sum of atomic contributions and will participate to the local MCA. The layer-resolved MCA obtained from the two methods are presented and an excellent agreement between them is indeed found.

To gain better understanding of MCA beyond bare numbers, investigating related quantities is helpful. The orbital moment is a quantity essentially related to the SOC and to the MCA in magnetic systems. It is well known that the easy axis always corresponds to the direction where the orbital moment is the largest. These arguments can be made more quantitative. As previously mentioned, Patrick Bruno [17] has derived an interesting relation (see Eq. 2.10) using second order pertubation theory (since first order term vanishes) with respect to the SOC parameter. Provided that the exchange splitting is large enough compared to the d-electron bandwidth, the MCA can be made proportional to the variation of the orbital moments.

This formula is based on a perturbative expansion (and an additional approximation concerning spin-flip transitions) for which the reference system and also the Fermi level

are those of the unperturbed system without SOC. It can be shown that this approach is compatible with a grand canonical ensemble description. (See Ref. [47] for a detailed discussion about statistical ensemble and second-order corrections in the context of magnetic anisotropy.) This relation can be generalized to systems with several atoms per unit cells [48] and also be used to extract a layer-resolved MCA [49].

In Fig. 2.2 the layer resolved MCA calculated by Bruno formula (green triangle ups) and by the force theorem (red squares) are plotted, we found that only the surface layers have a significant contribution, while contribution from the inner layers rapidly converges to the bulk (zero) value within the two approaches. However, note that Bruno's model results in quite different total MCA compared to the FT approximation in the vicinity of the surface. One can say that there is a rather good qualitative agreement between the two approaches, however, Bruno's formula can significantly (and quantitatively) differ from the $\mathrm{FT_{gc}}$ results. This discrepancy can probably be attributed to the main approximation of Bruno's formula (besides the second-order expansion), which consists in neglecting spin-flip excitations when the majority spin d bands are fully occupied, which is not the case for Fe.

2.3.2 DFT calculations

In *ab initio* DFT calculations, the spin-orbit coupling is included explicitely in the relativistic K-S equations for 2-component electronic spinor wave functions with a self-consistently calculated potential. The SOC induced energy can be written as follows:

$$\delta E^{\mathrm{ind}} = E^{\mathrm{SR+SOC}}[n, \mathbf{m}] - E^{\mathrm{SR}}[n_0, \mathbf{m}_0]. \tag{2.17}$$

Here $n_0(\mathbf{r})$ and $\mathbf{m}_0(\mathbf{r})$ are the charge and spin densities from the scalar-relativistic (SR) self-consistent calculation while $n(\mathbf{r})$ and $\mathbf{m}(\mathbf{r})$ are those obtained with fullly relativistic (SR+SOC) self-consistent calculation. This induced energy δE^{ind} can be trivially split onto two contributions [13, 14]:

$$\delta E^{\mathrm{ind}} = E^{\mathrm{ind}}_{\mathrm{scf}} + \delta E^{\mathrm{ind}}_{\mathrm{band}}, \tag{2.18}$$

where

$$\delta E^{\mathrm{ind}}_{\mathrm{scf}} = E^{\mathrm{SR+SOC}}[n, \mathbf{m}] - E^{\mathrm{SR+SOC}}[n_0, \mathbf{m}_0], \tag{2.19}$$

$$\delta E^{\mathrm{ind}}_{\mathrm{band}} = E^{\mathrm{SR+SOC}}[n_0, \mathbf{m}_0] - E^{\mathrm{SR}}[n_0, \mathbf{m}_0] = \sum_i^{\mathrm{occ}} \epsilon_i(\hat{\mathbf{m}}) - \sum_i^{\mathrm{occ}} \epsilon_i, \tag{2.20}$$

The first term is due to change in self-consistent charge and spin densities while the second one comes purely from the change in band energies with and without SOC calculated at the same self-consistent (SR) $\{n_0, \mathbf{m}_0\}$ with the magnetic moment rotated to the direction $\hat{\mathbf{m}}$.

It has been demostrated by X. Wang *et al.* [13] that for "light" element systems with a small spin-orbit interaction (such as Fe, Co and Ni), the $E^{\mathrm{ind}}_{\mathrm{scf}} \propto \xi^4$ while $\delta E^{\mathrm{ind}}_{\mathrm{band}} \propto \xi^2$ with respect to the SOC constant ξ so that the band energy change is the dominant

contribution. Therefore, the MCA can be simply calculated as the band energy change between two magnetic orientation $\hat{\mathbf{m}}_1$ and $\hat{\mathbf{m}}_2$:

$$\mathrm{MCA} = \sum_i^{\mathrm{occ}} \epsilon_i(\hat{\mathbf{m}}_1) - \sum_i^{\mathrm{occ}} \epsilon_i(\hat{\mathbf{m}}_2) = \int^{E_F^1} E D^1(E) dE - \int^{E_F^2} E D^2(E) dE, \tag{2.21}$$

both calculated in the SR self-consistent potential with globally rotated magnetic moments in $\hat{\mathbf{m}}_1$ and $\hat{\mathbf{m}}_2$ directions which proves the Force Theorem in the present context. The last part of the equation rewrites the band energies in terms of densities of states $D^{1,2}(E)$ and Fermi energies $E_F^{1,2}$ of two magnetic configurations.

Our *ab initio* calculations are performed using the QUANTUM ESPRESSO (QE) [28] DFT package. QE performs an iterative solution of the K-S equations using a plane waves basis set and pseudopotentials (PPs) [38] to represent electron-ion interactions. The SOC can be considered as a local interaction since it is large in the neighbourhood of the nucleus and is treated in QE via fully-relativistic pseudopotentials (FR-PPs). The non-diagonal elements in spin of the Hamiltonian come from the SOC but also from the exchange-correlation potential since the calculations are necessary to be done with an option of non-collinear magnetism [50, 51].

We have implemented the Force Theorem in QE in the same two-step way as described above for TB model: i) a SCF calculation with scalar-relativistic PPs (without SOC) is performed to obtain the charge density and the spin moment distributions in real space, and ii) the spin moment is globally rotated to a certain direction followed by a non-SCF calculation with FR-PPs (with SOC). The change in band energy between two spin moment directions gives, as discussed above, the total MCA.

The total MCA is decomposed over different atoms I in a slightly different way in comparison with TB approach:

$$\mathrm{MCA}_I = \int^{E_F^1} (E - E_F^2) D_I^1(E) dE - \int^{E_F^2} (E - E_F^2) D_I^2(E) dE, \tag{2.22}$$

where the atomic density of states $D_I(E)$ is calculated by projecting electronic wave functions onto all atomic orbitals Ψ_α of I-th atom, $D_I(E) = \sum_{i\alpha} |\langle \Psi_\alpha | \phi_i \rangle|^2 \delta(E - \epsilon_i)$. It is important to note that the Fermi level of one of magnetic configurations (we have chosen here the second one), E_F^2, is substracted under integrals and exact Fermi levels for two configurations are used as the limits of integration. This way we avoid the reference to electronic levels of a system without SOC, since the PPs with and without SOC are not generally correlated and can produce an arbitrary shift of levels. Due to total charge conservation in this "canonical" approach, the sum of MCA_i over all atoms gives exactly the total MCA while for the "grand canonical" scheme, Eq. 2.15, it was, in principle, only approximate. The discrepancy between "grand canonical" and "canonical" formulations within TB approach is, however, very tiny since the effect of SOC on the Fermi level is negligable in the case of "light" elements like Fe or Co.

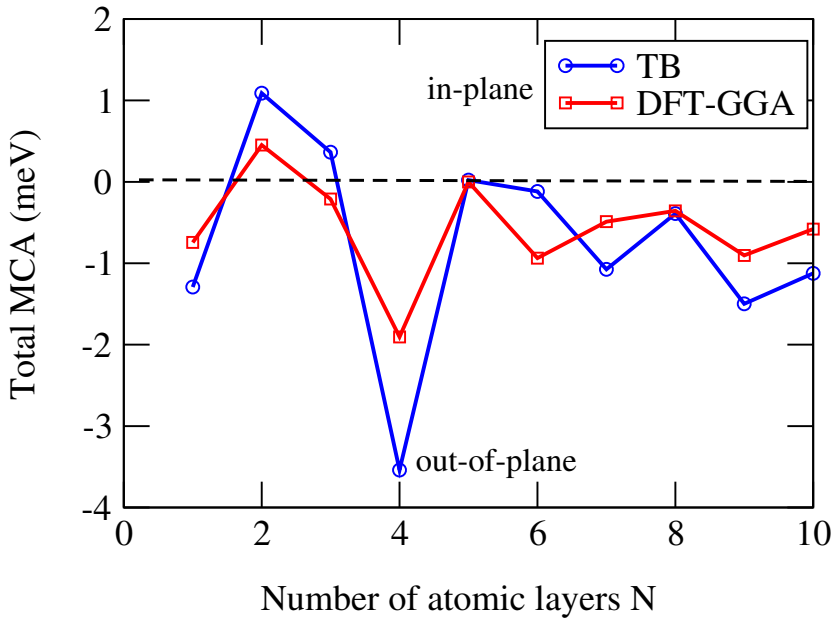

Figure 2.3: MCA of bcc-Fe(001) slab (per unit planar cell) as a function of its thickness N. TB calculations (blue circles) are compared with *ab initio* DFT-GGA results (red squares), both of them calculated within the force theorem approximation.

Since QE gives an access to real space wave-functions it is natural to define also the real-space resolved MCA as:

$$\mathrm{MCA}(r) = \int^{E_F^1} (E - E_F^2) D^1(r, E) dE - \int^{E_F^2} (E - E_F^2) D^2(r, E) dE. \tag{2.23}$$

where the local density of states is computed via electron wave-functions in the usual way, $D(r, E) = \sum_i |\phi_i(r)|^2 \delta(E - \epsilon_i)$. Once again, the integral of MCA(r) over all the space will give exactly the total MCA. This decomposition is very helpful in elucidating the electronic origin of the MCA.

In order to check the accuracy of the Force Theorem which we have implemented in the QE package, we have performed the calculations for bcc-Fe(001) with a various thickness ranging from 1 to 12 layers, with the full relativistic self-consistent calculations and FT approaches. The spin-orbit coupling is included via fully-relativistic ultrasoft pseudopotentials. The generalized gradient approximation (GGA) for exchange-correlation potential in the Perdew, Burke, and Ernzerhof parametrization [36] was employed. To describe thin films we have used the so-called super-cell geometry separating the adjacent slabs by about 10 Å in the z direction (orthogonal to the surface) in order to avoid their unphysical interactions. Since the MCA is usually a tiny quantity, ranging from μeV to meV, it requires a very precise determination of total energy, and the total energy difference among various spin directions is very sensitive to the convergence of computational parameters. We found

that 40×40 k-points mesh in the two-dimensional Brillouin zone was sufficient to obtain the MCA accuracy below 10^{-2} meV. A Marzari-Vanderbilt broadening scheme with 0.001 Ry broadening width was used with plane-wave kinetic energy cutoffs of 30 Ry and 300 Ry for the wave functions and for the charge density, respectively. The MCA obtained by these two different methods differs by less than 10^{-2} meV, providing a validity of FT in first-principles calculations. For more details about the convergence tests of force theorem, please see ANNEXE A.

Next, we compare in Fig. 2.3 the total MCA for the same Fe slabs calculated within Force Theorem by DFT and TB approaches. A good agreement between two calculations is found which proves, in particular, the efficiency and quality of our TB model. Note, however, the larger discrepancy between TB and DFT-GGA for thin slabs, which indicates the limits of the TB model, which are probably less accurate for low coordinated systems.

CHAPTER 3

Magneto-crystalline anisotropy of Fe and Co free-standing slabs

In this chapter, we will analyse the MCA of two-dimensional Fe and Co free-standing slabs with different crystallographic orientations. A particular emphasis is made on the local analysis of MCA: decomposition of MCA over different atoms as well as atomic orbitals. Finally, our rather general orbital-resolved analysis applies also to other systems and allows, for example, predicting the MCA behavior of magnetic thin films upon covering by various organic materials such as graphene or C_{60} molecule.

As mentioned before, the MCA originates from the relativistic manifestation of the coupling between the electron spin and its own orbital motion. It is well kown that the MCA in bulk cubic $3d$ systems is extremely small (typically some μeV/atom) since the orbital moment is nearly quenched. However, a much larger anisotropy can be expected in low-dimentional systems such as ultrafilms (typically some meV/atom) due to reduced dimentionality (reduction of coordination) or symmetry. Moreover, since the SOC is a very localized effect, the modification of electronic structure at surfaces and interfaces can give rise to striking magnetic behaviour in ultrathin magnetic films, such as perpendicular magnetic anisotropy (PMA) which was first shown experimentally by Gradmann and Müller [52] in epitaxial $Ni_{48}Fe_{52}(111)$ thin films. Hence, in the past, the MCA in many ferromagnetic multilayers and ultrathin films has become of particular interest due to their potential technological applications such as perpendicular recording media [53, 54].

The investigation of the MCA for magnetic naostructures remains a challenge to both theory and experiment. From the experimental point of view, the MCA is routinely measured by magnetic hysteresis loops [55]. Recently two different techniques are employed to

study the magnetic properties of magnetic thin films. The first one is the X-ray magnetic circular dichroism (XMCD) [56] which relies on the fact that light absorption in magnetic material depends on the light polarization, thus it allows to determine the spin and orbital moments as well as the MCA of single atoms. Another key technique is magneto-optic Kerr effect (MOKE) [57] based on the fact that the polarization state of light is modified when reflected at a magnetic material. From theoretical point of view, the treatment of MCA is always numerically delicate due to its tiny value. Technically, several approaches have been developped for determination of the surface MCA. A brute force method involves *ab initio* self-consistent calculations including SOC and determination of total energies for different spin orientations [58–61]. This approach, although straightforward, is also the most computationally demanding. The other method uses the fact that the SOC in $3d$ transition metals is rather small ($\sim$ 60 meV) which makes a perturbative treatment of SOC possible. Using a perturbative treatment of SOC in tight-binding, some important features of the MCA for monolayer and multilayer have been cleared up with respect to the orbital moment, d-band filling and crystal field effects [17, 62, 63]. Concomitantly, the *ab initio* calculations using the so-called force theorem is well suited to calculation of MCA for several layered ferromagnetic systems [21, 64–68]. Besides its computational efficiency, it is also very stable numerically.

There exists a vast body of research on the MCA of Fe and Co 2D geometries deposited on different substrate both experimentally ([69–74] for Fe and [75–79] for Co) and theoretically ([16, 80–84] for Fe and [85–88] for Co), and a review is available in Ref. [89]. In this chapiter, we will present a systematic studies of MCA for Fe and Co freestanding slabs by tight-binding as well as first-principles calculation in the framework of DFT, with a particular emphasis on the atomic site/d-orbitals decomposition of MCA. This study could be useful to explain the existing experiments or prepare future experiments.

3.1 Total MCA of Fe and Co slabs

3.1.1 Methodology and structures

The Fe and Co slabs were constructed from bcc-Fe and fcc-Co with the lattice parameters of $a_0^{\mathrm{Fe}} = 2.85$ Å and $a_0^{\mathrm{Co}} = 3.53$ Å found from *ab initio* calculations (which is close to the experimental values of $a_0^{\mathrm{Fe}} = 2.87$ Å and $a_0^{\mathrm{Co}} = 3.54$ Å) and no atomic relaxations were considered. The MCA has been calculated using the force theorem (see 2.2.2) which was checked to work very well due to small spin-orbit coupling in Fe and Co. Hence the MCA is defined as the band energy difference for $\mathbf{M}$ perpendicular or parallel to the atomic slabs. Explicitely, $\mathrm{MCA} = E_{\perp}^{\mathrm{band}} - E_{\parallel}^{\mathrm{band}}$.

In the TB model, a mesh of 50×50 in-plane k points has been used for SCF calculations without SOC whereas the mesh was incresed to 140×140 in non-SCF calculations with SOC in order to provide a precision below 10^{-5} eV. A Marzari-Vanderbilt broadening scheme with smearing parameter of 10 meV has been used.

Ab initio DFT calculations were carried out with QUANTUM ESPRESSO package [28]

using generalized gradient approximation (GGA) for exchange-correlation potential in the Perdew, Burke, and Ernzerhof parametrization [36]. The scalar relativistic self-consistent calculations were performed first followed by one-step full relativistic calculations including SOC (relativistic ultrasoft pseudopotentials). The cut-off energies were set to 30 and 300 Ry for wave-functions and charge density, respectively. We used 10 Å of vacuum space in the z direction in order to avoid the unphysical interactions between two adjacent slabs. The mesh of 40×40 k points for both scalar relativistic and full relativistic calculation was used and the same smearing parameter and technique were employed.

3.1.2 Results and discussions

Fig. 3.1 shows thickness dependence of the total MCA of N-atom bcc-Fe and fcc-Co bulk slabs of different crystallographic orientations, (001)/(110) for Fe and (001)/(111) for Co, respectively. In the case of Co slabs, the results of both TB (blue) as well as *ab initio* (red) calculations are presented. Note that positive (negative) value of MCA means in-plane (out-of-plane) eaxy axis.

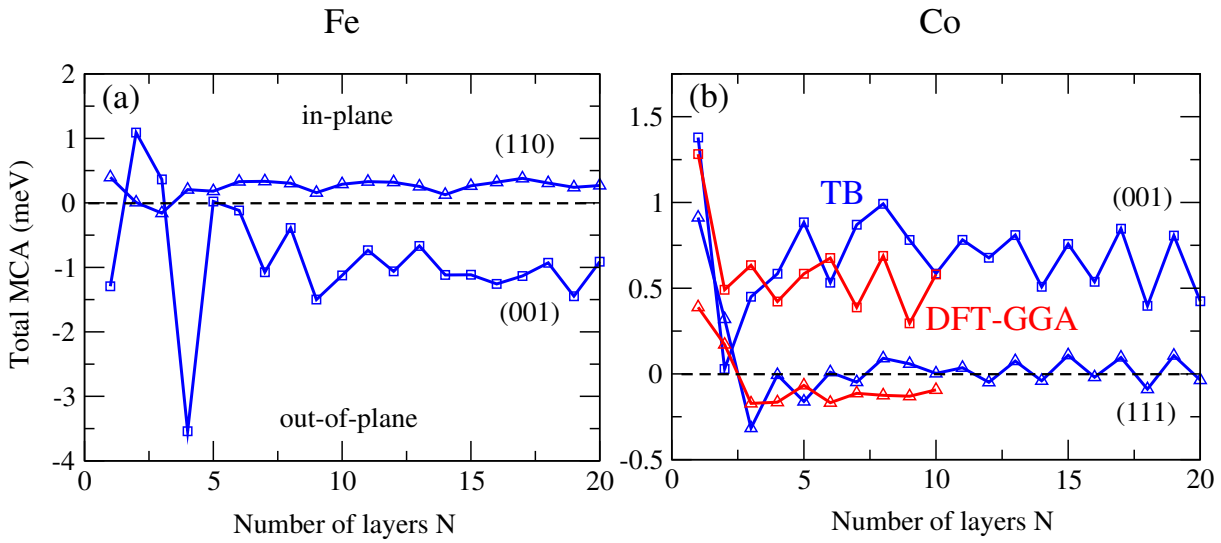

Figure 3.1: Total MCA per unit cell, $E_{\perp}^{\text{band}} - E_{\parallel}^{\text{band}}$, of N-atom-thick bcc-Fe and fcc-Co slabs as a function of the number of layers N. Squares and triangle ups are for two different orientations of Fe and Co slabs, respectively. In the case of fcc-Co slabs, TB calculations (blue) are compared with *ab initio* DFT-GGA calculations (red)

.

The quite large oscillating behaviors have been found for all slabs, such oscillations remain even for thick slabs, particularly pronounced for Fe(001) and Co(001). This kind of long-range oscillating behavior has been recently reported by experiments in thin ferromagnetic films of Fe and Co [74, 90, 91], and was interpreted in terms of spin-polarized quantum well sates (QWS). The QWS are formed in ferromagnetic films from occupied

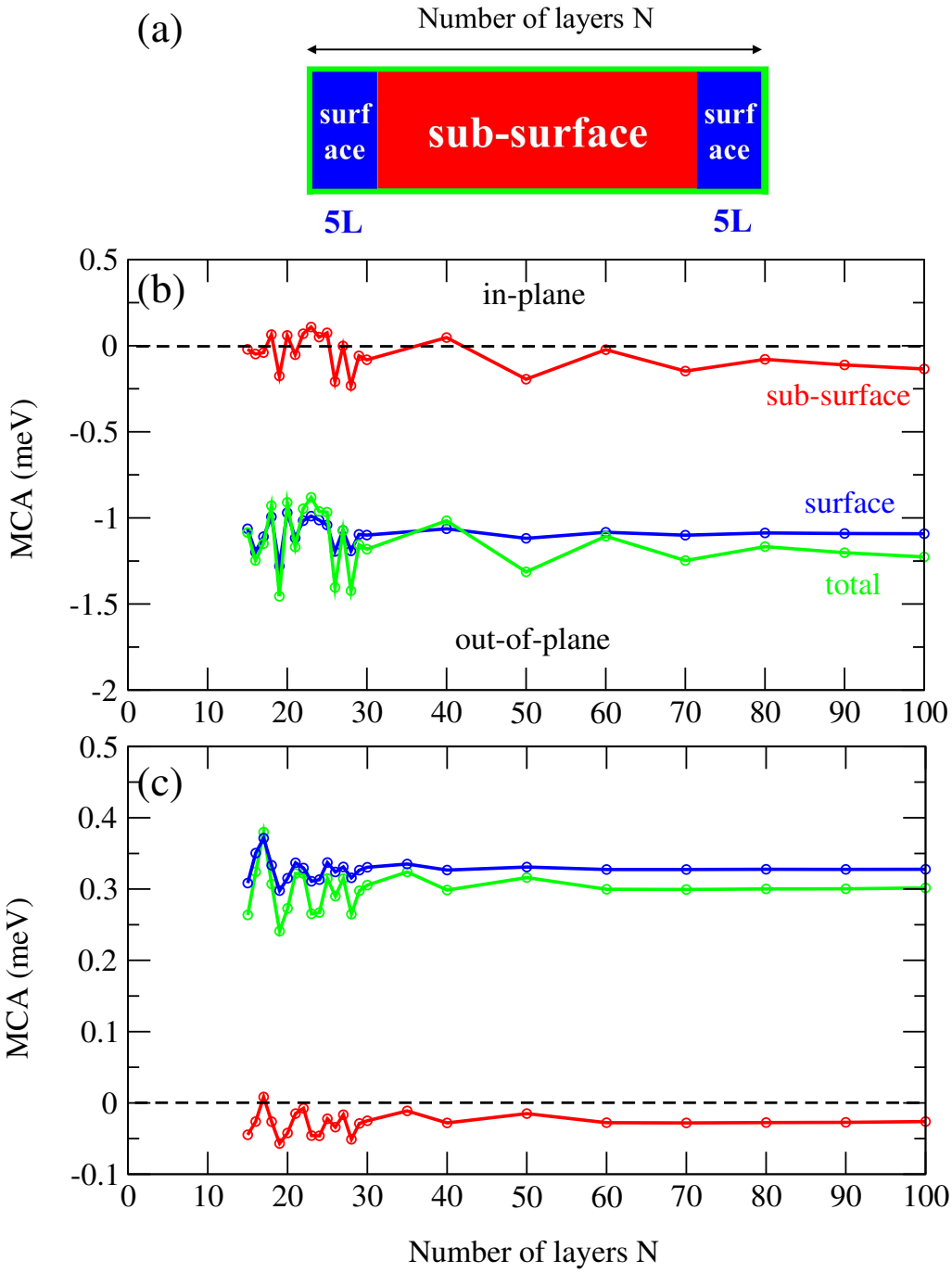

Figure 3.2: TB results: (a) Schematic presentation of N-atom slabs with surface and sub-surface contribution. The surface contribution is obtained by summing the MCA over the five outer layers of the unit cell on each side of the slab. Surface (blue), subsurface (red) and total MCA (green) per unit cell of N-atom for (b) bcc-Fe(001) and (c) bcc-Fe(110) slabs as a function of the number of atomic layers N in the slab. Positive (negative) MCA values mean in-plane (out-of-plane) eaxy-axis direction. The two different slabs orientations have MCA of opposite sign.

and unoccupied states close to the Fermi level that contribute significantly to the MCA. Although the amplitude of the quantum oscillations is comparable with the total MCA even for the thickest slabs, it is clear that the MCA converges with respect to the slab thickness for every orientations.

Interestingly, we find the opposite behavior for Fe and Co slabs: while the total MCA is out-of-plane/in-plane for Fe(001)/ Fe(110) slabs it is, on the contrary, in-plane/out-of-plane for Co(001)/Co(111) ones. We notice that the converged total MCA for Fe(001) and Co(001) clearly favors out-of-plane and in-plane magnetization, with anisotropy energy around -1 meV/cell and 0.6 meV/cell, respectively. A much smaller amplitude of MCA has been found for both Fe(110) and Co(111), about 0.2 meV/cell for Fe(001) and -0.05 meV/cell for Co(111).

We find a relatively good overall agreement between TB and DFT calculations for Co(001). We further note that in the case of Co(111), the MCA oscillates around zero in the TB model, while the DFT calculations predict rather small out-of-plane magnetic anisotropy. Our results for Co slabs compare rather well with DFT calculations in Ref. [92] done with LDA approximation for exchange-correlation functional.

We also calculated the shape anisotropy of Fe and Co slabs and an almost linear dependence with respect to the thickness has been found for all slabs, please see the ANNEXE D.1 for the detailed analysis.

3.2 Surface and sub-surface contributions

To understand the origin of oscillatory behavior of MCA, we decomposed the total MCA as the surface and sub-surface contributions. We plot in Fig. 3.2 the evolution of the surface (blue), sub-surface (red) and total MCA (green) for both Fe(001) and Fe(110) slabs with respect to the total number of layers N (from 15 to 100). It is natural to define surface MCA as a sum of contributions from five outer layers (from both sides of the slabs) as shown in Fig. 3.2 (a).

The contributions from other layers sum up to what we call a sub-surface MCA. Note that the true surface MCA should be obtained by dividing the surface contribution presented in Fig. 3.2 by two since the slabs contain two surfaces. Our calculations show that Fe(001) and Fe(110) surfaces have very different qualitative behaviour, the total MCA is negative for Fe(001) indicating an out-of-plane easy axis while it is in-plane for Fe(110) since its MCA is positive. More interestingly, in the case of Fe(110), additional calculations have shown that the magnitude of the in-plane anisotropy is almost as large as the one obtained between in-plane and out-of-plane orientations. It is also important to mention that the amplitude of the oscillations, though do not change the sign of the MCA, can however be as large as 0.2 meV for Fe(001) and 0.1 meV for Fe(110) at least up to $N \sim 40$. In addition, the total MCA is essentially dominated by the surface contribution. However, the oscillatory behaviour at large thicknesses, particularly pronounced for Fe(001), clearly originates from the sub-surface. Therefore the QWS interpretation seems valid.

3.3 Layer-resolved MCA

We further study the local decomposition of MCA of Co(001) and Co(111) slabs made of 20 atomic layers as shown in Fig. 3.3. Here, the TB and DFT results have been compared in terms of local analysis. A qualitatively good agreement between TB and DFT calculations is again found for both slabs with the main discrepancy appearing for the surface layers, which indicates that the TB model is presumably less accurate for low coordinated atoms. Interestingly, for both Co(001) and Co(111) slabs these surface layers possess in-plane anisotropy. The local MCA site decomposition then shows damped oscillations converging towards a tiny bulk value. However, while the MCA of the Co(001) slab is strongly dominated by the outermost surfaces layer, this is not the case for the Co(111) slab where sub-surface layers cancel (and even overcome in the DFT case) the surface contribution. This leads to the large in-plane and rather small out-of-plane overall MCA for the Co(001) and Co(111) slabs, respectively, as it is reported in Fig. 3.1.

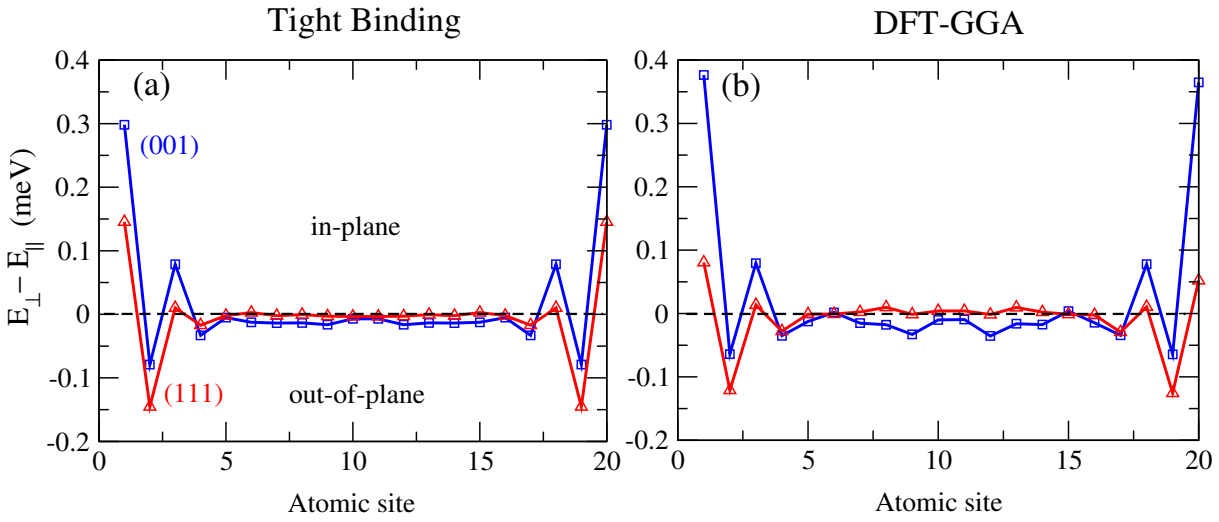

Figure 3.3: Layer-resolved MCA of Co slabs with 20 atomic layers calculated by (a) tight-binding and (b) DFT-GGA within the force theorem approximation. Blue sqaures and red triangle downs are for Co(001) and Co(111) slabs, respectively.

3.4 *d*-orbitals-resolved MCA

For free-standing Fe and Co slabs, the density of states (DOS) around the Fermi energy arises mainly from the minority-spin *d*-orbitals since the majority-spin bands are almost fully occupied and well below E_F. In order to get even more insight into the local decompositon of MCA, we show in Fig. 3.4 the decomposition of the total MCA over different atoms and atomic *d*-orbitals using local density of states (see Eq. 2.22) for Fe and Co

slabs $N = 10$ with different crystallographic orientations. First of all, the structural relaxation was performed by fixing the first seven first layers and relaxing the other three layers (numbered as 7-10 in Fig. 3.4) until atomic forces become smaller than 0.001 eV/Å for determining the most stable geometries. The MCA, taken as the band energy difference between out-of-plane and in-plane magnetic configurations, $E_{\perp}^{\text{band}} - E_{\parallel}^{\text{band}}$, is obtained non-self-consistently (force theorem is applied). And $E_{\parallel}^{\text{band}}$ was chosen as the one with spin direction having azimuthal angle of $\phi = 45°$. This will make the local decomposition of MCA with almost equal contributions for each pair of (d_{zx}, d_{zy}) and of $(d_{x^2-y^2}, d_{xy})$ due to symmetry of d-orbitals extensions. Additionally, since the MCA in the surface plane was found to be extremely small, the choice of this reference in-plane configuration is otherwise irrelevant.

Interestingly, we found that different atomic d-orbitals lead to different magnetic anisotropy. All the curves are almost symmetric which indicate the relaxation effect is negligible. Note that a positive (negative) value of MCA means an in-plane (out-of-plane) magnetization easy axis.

For bcc-Fe(001), the $(d_{x^2-y^2}, d_{xy})$ orbitals spatial extension is essentially in the surface plane, show strong out-of-plane anisotropy of about -0.16 meV/atom at the surface and converge to very small in-plane anisotropy of about 0.02 meV/atom when penetrating into the sub-surface. On the other hand, the d_{z^2} orbital, particularly perpendicular to the slab, favors in-plane magnetization by about 0.08 meV/atom at the surface and it is almost zero anisotropy in the sub-surface. The other (d_{zx}, d_{zy}) orbitals show relatively small out-of-plane of about -0.03 meV/atom at the surface and it oscillates even in the deep sub-surface. The QWS are essentially related to these orbitals.

In the case of bcc-Fe(110), we found that the surface anisotropy is about -0.06 meV/atom $(d_{x^2-y^2}, d_{xy})$, -0.04 meV/atom (d_{z^2}) and 0.00 meV/atom (d_{zx}, d_{zy}) while the sub-surface anisotropy is about -0.06 meV/atom $(d_{x^2-y^2}, d_{xy})$, 0.04 meV/atom (d_{z^2}) and 0.04 meV/atom (d_{zx}, d_{zy}), respectively.

For Co slabs, a very similar feature has been found for fcc-Co(001), fcc-Co(111) and hcp-Co(0001) slabs, showing strong out-of-plane anisotropy for $(d_{x^2-y^2}, d_{xy})$ while it is strong in-plane magnetization for d_{z^2} orbital for both surface and sub-surface atomic sites. The other (d_{zx}, d_{zy}) orbitals favor in-plane magnetization with relatively small magnitude of MCA. Note that in the case of fcc-Co(001), the magnitude of MCA is much larger than it is in other two Co slabs.

Recently, it has been shown that the MCA of free magnetic surfaces can be significantly modified by depositing organic materials such as graphene and C_{60} molecule. For instance, due to hybridization between graphene and Co electron orbitals, the magnetic anisotropy is significantly larger for graphene/Co interface than for the free Co surface [93, 94]. In addition, more recently in C_{60}/hcp-Co(0001) interface, the group of V. Repain observed using MOKE and XMCD techniques a C_{60} overlayer enhances the perpendicular magnetic anisotropy of a Co thin film, inducing an inverse spin reorientation transition from in plane to out of plane [95]. State-of-art first-principles calculations were performed by our group to explain this spin reorientation. We found that the MCA and spin moment of

Co atoms close to the molecule get suppressed due to hybridization between carbon π orbitals and d-orbitals of the Co surface. The strongest hybridization occurs with the out-of-plane oriented d_{z^2} orbital and the smallest for the in-plane oriented $(d_{x^2-y^2}, d_{xy})$. As a consequence, the overall MCA for the Co atoms appears to enhance strongly favoring the out-of-plane orientation [95]. For the same reason, if we deposit C_{60} molecule on bcc-Fe(110), the out-of-plane magnetization of $(d_{z^2}, d_{zx}, d_{zy})$ orbitals get suppressed due to hybridization at the interface, we observe a spin reorientation transition from out-of-plane to in-plane. We believe that our rather general orbital-resolved analysis applies also to other systems that show similar hybridizations and allows, for example, predicting the MCA behavior of magnetic thin films upon covering by various organic materials.

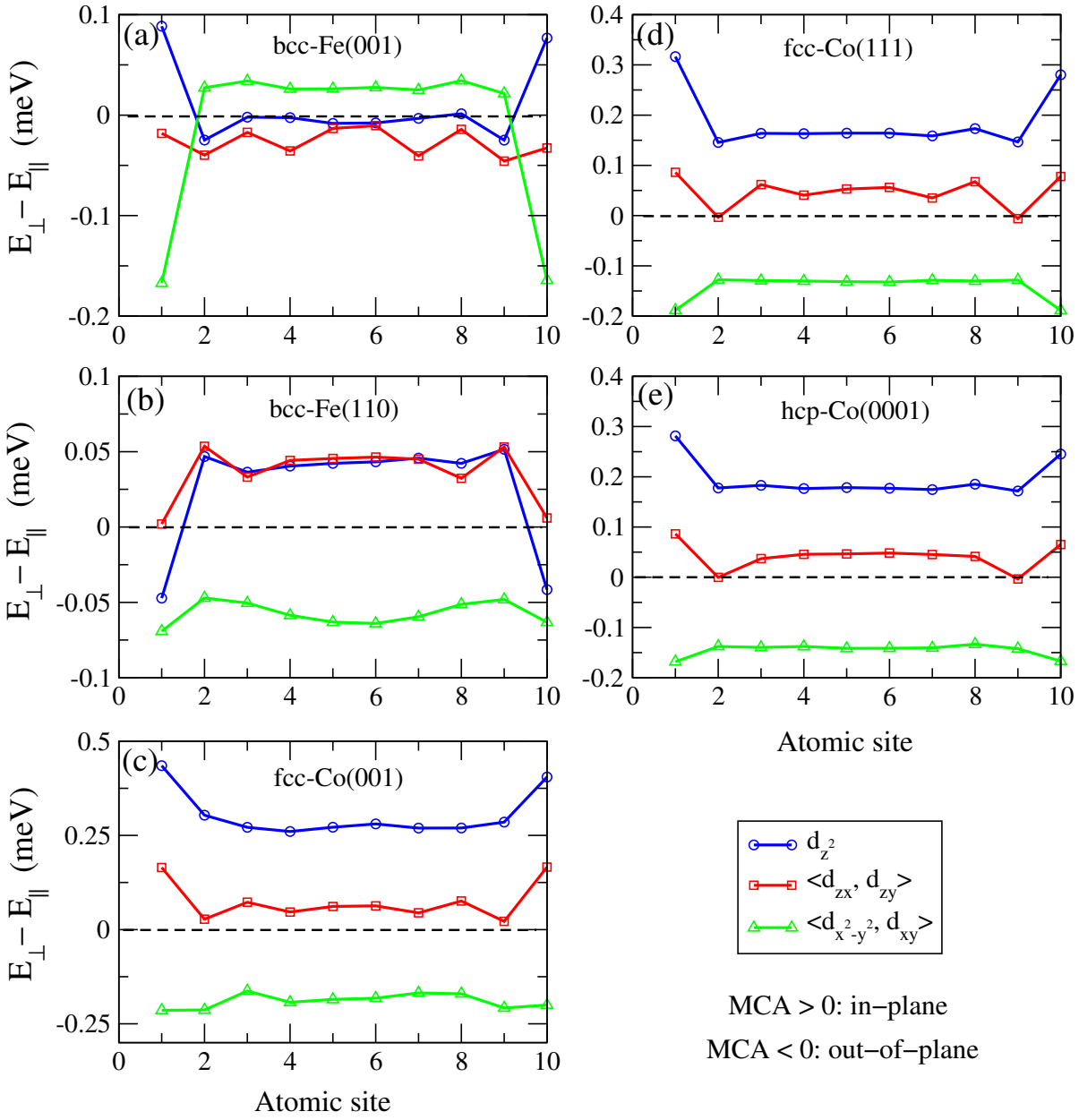

Figure 3.4: DFT results: *d*-orbitals decomposition of MCA for Fe and Co slabs made of 10 atomic layers: (a) bcc-Fe(001), (b) bcc-Fe(110), (c) fcc-Co(001), (d) fcc-Co(111) and (e) hcp-Co(0001). Due to symmetry, contributions from different orbitals in (d_{zx}, d_{zy}) and $(d_{x^2-y^2}, d_{xy})$ pairs are very similar so that their averaged values are presented for simplicity.

CHAPTER 4

MCA of free Fe and Co nanocrystals

In this chapter, we report the calculation of the magnetic anisotropy energy (MAE) of free bcc-Fe and fcc-Co nanocrystals using tight-binding as well as first-principles calculations. We first present the STM observations of epitaxially grown Fe and Co nanocrystals in the form of truncated square pyramids. Our calculations show that, for both elements, the total MAE of free nanocrystals is largely dominated by (001) facets resulting in out-of-plane or in-plane easy axis for Fe or Co, respectively. As a consequence, in Co nanocrystals the spin moment is allowed to rotate almost freely (with a very low in-plane anisotropy barrier) in the easy basal plane while Fe nanocrystals have a high uniaxial anisotropy which makes them much better potential candidates for magnetic storage devices.

Magnetic nanocrystals are of considerable interest because of their potential applications such as high density magnetic recording and memory devices. The electronic and magnetic properties of nanocrystals vary dramatically from their bulk counterparts due to reduced corordination, which offer various opportunities of applications. For nanoclusters of 3*d*-transition metal, the magnetic moment per atom are typically enhanced [96, 97] as compared to their bulk metals, whereas 4*d* elements such as Pd and Rh, which are not magnetic in bulk, can exhibit a magnetic moment in nanoclusters [98, 99]. A key property of any magnetic nanocrystal is its magnetic anisotropy energy (MAE), which is quantified by the energy barrier for flipping the total magnetization between two metastable states. One of the challenges in exploring the ultimate density limit of magnetic information storage is evidently to be able to synthetize well ordered arrays of magnetic nanocrystals of similar sizes and shapes with as large magnetization and magnetic anisotropy as possible. The MAE of 3*d* transition metal nanocrystals (e.g., Fe, Co and Ni) is indeed a subject of intense study both experimentally [24, 100–102] and theoretically [21, 25, 85, 103–107] but

the ability to grow well defined magnetic crytalline nanostructures is also a major issue [3, 108–113]. This is especially the case for Fe and Co nanostructures, that can adopt various crystalline bulk structures. For instance, the Fe natural bulk structure is body-centered cubic (bcc) but it can also be stabilised in a face-centered cubic structure (fcc) structure if it is grown in thin films [114, 115]. In the case of Co, the hexagonal close packed (hcp) structure is the stable bulk but it can be obtaind in thin-film growth of metastable bcc [116], fcc [116–118] or face-centered-tetragonal [119] structures.

In particular, F. Silly and co-workers [3, 25] showed that it is possible to grow Fe and Co nanocrystals by epitaxy on a $SrTiO_3(001)$ support with a remarkable control of their size, shape and structure. The bcc and fcc structures have been found for Fe and Co nanocrystals, respectively. The nanocrystals obtained are in a shape of truncated square pyramids containing two different facets, namely (001)/(110) facets for Fe and (001)/(111) facets for Co. The close-packed and lowest-energy facet for bcc structure is the (110) facet, whereas it is (111) facet for fcc structure [120]. This is the reason for the (110) facets appearing in bcc nanocrystals [in fact, for Fe the surface energies of (001) and (110) orientations are almost the same] and the (111) facets appearing in fcc nanocrystals.

Due to the sensitive interrelation between the magnetism and the atomic structure of these magnetic blocks, any induced modification of the nanostructure will lead to different magnetic properties, particularly important for MAE. In this context, a fundamental problem for the magnetic nanocrystals is to understand how the magnetic anisotropy is determined by the size, shape, facet structure as well as the underlying substrate.

4.1 Self-assembled Fe and Co nanocrystals growth

4.1.1 STM observations

The $SrTiO_3(001)$ surface exhibits different reconstructions [121] depending on sample preparation, which can be used for supported nanocrystal growth. The ground state of $SrTiO_3$ is a perovskite cubic structure with a 3.905 Å lattice parameter. The indirect band gap of pure $SrTiO_3$ is 3.2 eV (while direct band gap energy is 3.75 eV), which makes it unsuitable for imaging in the scanning tunneling microscope (STM). To overcome this problem, one has to use $SrTiO_3(001)$ crystals doped with 0.5% (weight) Nb.

Fig. 4.1 (a) and (b) show the topography of Fe and Co nanocrystals which have been grown on $SrTiO_3(001)$-c(4×2) surface. The nanocrystals have self-assembled into similarly sized nanocrystals. Interestingly, both bcc-Fe and fcc-Co nanocrystals have a truncated-pyramid shape with a (001) top facet and a (001) interface. However, the bcc nanocrystal has the (110) side facets while the fcc nanocrystals has the (111) side ones. As a guide to the eye we have shown in Fig. 4.1 (a) and (b) a schematic illustration of a truncated pyramid. In addition, the measured angle between the side facets and the substrate is ∼45° and ∼54.7° for Fe and Co, respectively. The facet angle is therefore a sufficient condition to distinguish the bcc from fcc structure. The interplanar periodicity along the (001) direction is one-half of the unit-cell dimension for both lattices (1.44 Å for bcc, 1.77 Å for

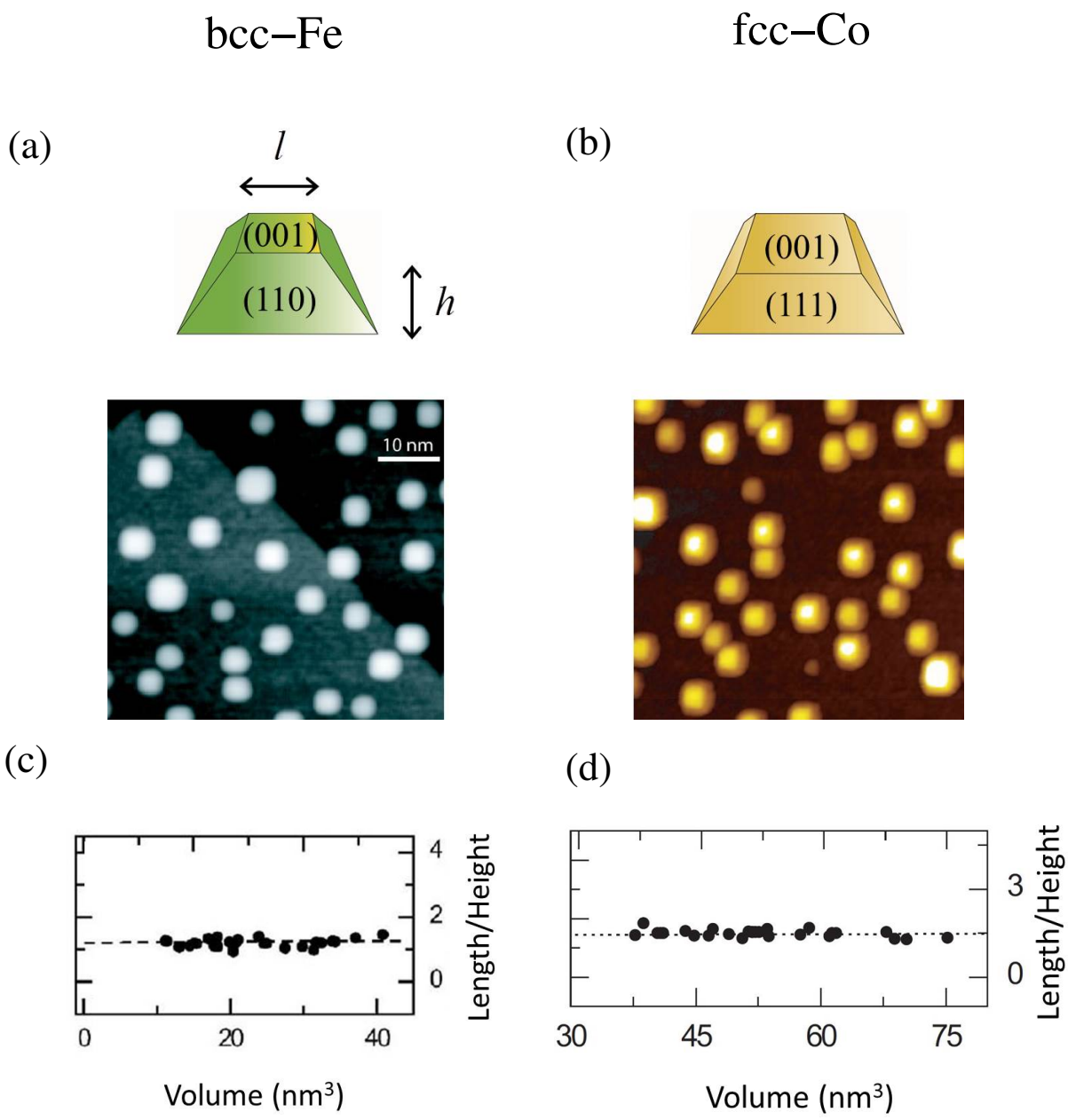

Figure 4.1: STM topography of truncated pyramid-shaped Fe [3] (a) and Co [25] (b) nanocrystals on $SrTiO_3$(001)-c(4×2) substrate. The schematic models of bcc-Fe and fcc-Co are also shown. The length to height ratio of both nanocrystals is constant with respect to its volume and approximately equal to 1.20 and 1.48 for Fe (c) and Co (d), respectively.

fcc). The interface is therefore a (001) plane and the interface crystallography is $(001)_{Fe} \parallel (001)_{SrTiO_3}$, $[100]_{Fe} \parallel [110]_{SrTiO_3}$, $(001)_{Co} \parallel (001)_{SrTiO_3}$, $[100]_{Co} \parallel [100]_{SrTiO_3}$. Therefore, the Fe nanocrystals are rotated by $\sim 45°$ with respect to the $SrTiO_3$ in order to get a better match with the lattice parameter of substrate. The ratio of the length (ℓ) of the top square to the height (h) of the Fe and Co truncated pyramids as a function of volume is shown in Fig. 4.1 (c) and (d). The constant ratio of ℓ/h=1.20±0.12 (Fe) and ℓ/h=1.48±0.13 (Co) suggests that these pyramidal nanocrystals have reached their equilibrium shape. Note that the error in the ratio denotes the standard deviation of the measurements.

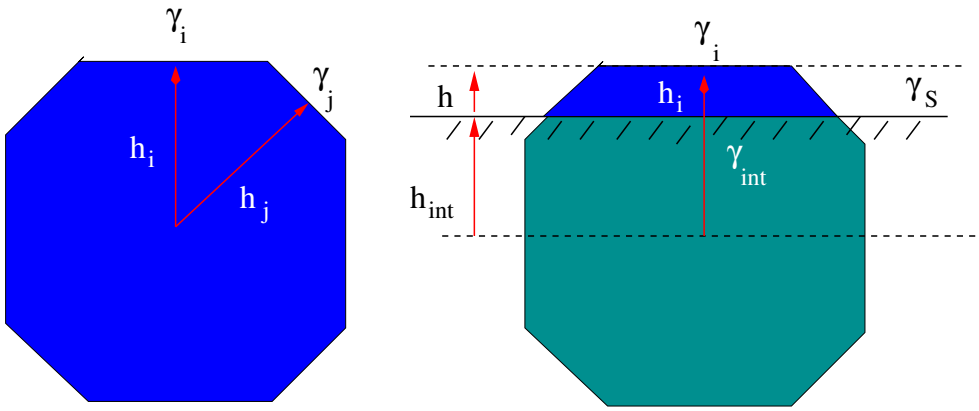

Figure 4.2: Wulff (left) and Wulff-Kaichev (right) construction to determine the equilibrium shape of a free or supported crystal.

4.1.2 Wulff construction

The equilibrium shape of a crystal can be obtained from the Wulff construction [122]. It is based on a variational principle where the total energy of a system is minimized at constant volume. The principle ingredient of the construction is the so-called γ-plot which is a polar representation of the surface energy $\gamma(\mathbf{n})$ for any direction $\mathbf{n}$ of the crystal. The γ-plot usually presents sharp cusps (corresponding to surface energy minima) in high-symmetry directions which define the facets that will appear on the polyhedron shape of the crystal. The size of a facet is basically inversely proportional to its corresponding surface energy. More precisely the following relation holds

$$\frac{\gamma_i}{h_i} = \text{constant} \tag{4.1}$$

where γ_i is the surface energy per surface area of facet i and h_i is the distance of this facet to the center of the crystal. When the nanocrystal is grown on a substrate the Wulff construction is extended into a Wulff-Kaichev construction where the interface energy γ_{int} between the deposited material and the substrate as well as the surface energy of the

substrate γ_S are taken into account. The equilibrium shape is now a truncated Wulff-polyhedron and the truncation height h_{int} is given by the relation (see Fig. 4.2):

$$\frac{\gamma_i}{h_i} = -\frac{\gamma^*}{h_{\text{int}}} = \text{constant}. \tag{4.2}$$

where h_{int} is the distance between the center of the cluster and the interface and γ^* is defined as the difference between the interface energy and the substrate surface energy $\gamma_{\text{int}} - \gamma_S$. When γ^* is negative h_{int} is positive and the Wulff polyhedron is truncated above its median plane (which is the case shown on Fig. 4.2).

In the case of Fe nanocrystals (001) and (110) are the only facets present. Moroever the equilibrium shape of the deposited nanocrystal is a truncated pyramid and the lateral cubic facets are absent meaning that the truncation height h_{int} is larger than $l/2$ (where l is the length of the side of the square facet (see Fig. 4.1). From Eq. 4.2 we have $h = h_{(001)}(1 + \gamma^*/\gamma_{(001)})$ and then expressing $h_{(001)}$ as a function of l (making use of Eq. 4.1) it comes out that the following relation holds:

$$\gamma^* = 2\frac{h}{l}(\sqrt{2}\gamma_{110} - \gamma_{001}) - \gamma_{001}, \tag{4.3}$$

The calculated surface energies by DFT are found to be $\gamma_{001} \approx 2.19$ J/m^2 and $\gamma_{110} \approx 2.18$ J/m^2 which is in agreement with Ref. [123]. By using the length to height ratio ($l/h \approx 1.21$) from the experimental mesurement and the surfaces energies from the calculations, then γ^* ≈-0.76 J/m^2. The strength of the hybridization between the nanocrystal and the substrate can be characterized by its adhesion energy, γ_{adh} that can be obtained from Dupre's formula

$$\gamma_{\text{adh}} = \gamma_{001} + \gamma_{\text{STO}} - \gamma^*. \tag{4.4}$$

This results in $\gamma_{\text{adh}} \approx 3.05$ J/m^2.

In the case of Co nanocrystals, only (001) and (111) are seen on the nanocrystal and the $l/h \approx 1.41$, the adhesion energy is found to be about 3.74 J/m^2.

4.2 Tight-binding model

4.2.1 Geometry of nanocrystals

As has been discussed above, bcc-Fe nanocrystals [3] as well as fcc-Co nanocrystals [25] (Fig. 4.1) can be epitaxially grown on a $SrTiO_3$ substrate with a remarkable control of size, shape and structure. These nanocrystals can contain up to several hundreds atoms and have the form of truncated pyramids, as shown in Fig. 4.3, with a rather constant length-to-height ratio, l/h. The nanocrystals are made of two (001)/(001) top and base facets and four (110)/(111) side facets for Fe/Co nanocrystals. They, however, adopt different bulk structure, i.e., the nanocrystal facets will therefore be different because the close-packed and lowest-energy facet for bcc structure is the (110) facet,whereas it is the (111) facet for

the fcc structure. It is expected that the MAE of such pyramids will be dominated by the surface composed of (001) and (110) or (001) and (111) facets for Fe and Co nanocrystals, respectively. The magnetic properties of nanocrystals will therefore not only depend on the bulk structure but also on the facets orientation and their area.

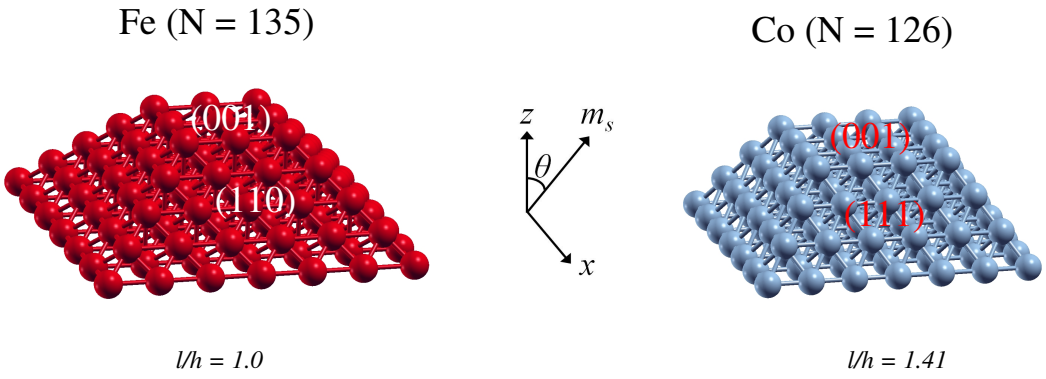

Figure 4.3: Examples of truncated-pyramid shaped Fe and Co nanocrystals studied in the present work. The crystals are made of bcc-Fe and fcc-Co with two types of facets: (001) and (110) for Fe and (001) and (111) for Co, respectively. Their possible size and shape is controlled by length-to-height ratio, l/h, kept to ~ 1.0 (Fe) and 1.41 (Co) which are close to experimental values, ~ 1.20 (Fe) [3] and ~ 1.48 (Co) [25]. The z axis was chosen to be normal to the pyramid base and the spin moment is rotated in the xz plane forming the angle θ with the z axis.

4.2.2 Total MCA of truncated pyramid of different sizes

There exists a vast body of research on the theoretical investigation of combined structural and magnetic properties of unsupported transition metal clusters but relatively fewer are devoted to the determination of their magnetic anisotropy. Moreover, most of them deal with small nanoclusters containing few atoms [85, 103, 124], and the case of large clusters is generally treated with empirical Neel-like models of anisotropy [24]. In the following, we will present TB calculation of paticular nanocrystals containing only two different facets of orientations (001)/(110) and (001)/(111) for Fe and Co, respectively.

The length-to-height ratio of different size of bcc-Fe and fcc-Co nanocrystals can be written $l/h = [2(n_1 - 1)]/(n_2 - n_1)$ and $l/h = \sqrt{2}(n_1 - 1)/[(n_2 - n_1)]$, where $n_2 \times n_2$ and $n_1 \times n_1$ are the number of atoms in the first (bottom) and last (up) layers of the truncated pyramids. We then selected different sizes of bcc-Fe and fcc-Co nanocrystals with the length-to-height ratio of ~ 1.0 (more precisely, $l/h = 1.0$ for N = 29, 135; 1.20 for N = 271; 1.14 for N = 620) and 1.41 (N = 50, 126, 255, 451, 728) close to the experimental value of 1.20±0.12 [3] and 1.48±0.13, respectively (more details, see ANNEXE C). Since the MCA in the xy plane was found to be extremely small, we kept the magnetization always in the xz plane making the angle θ with the z axis. The MCA is defined as the change in

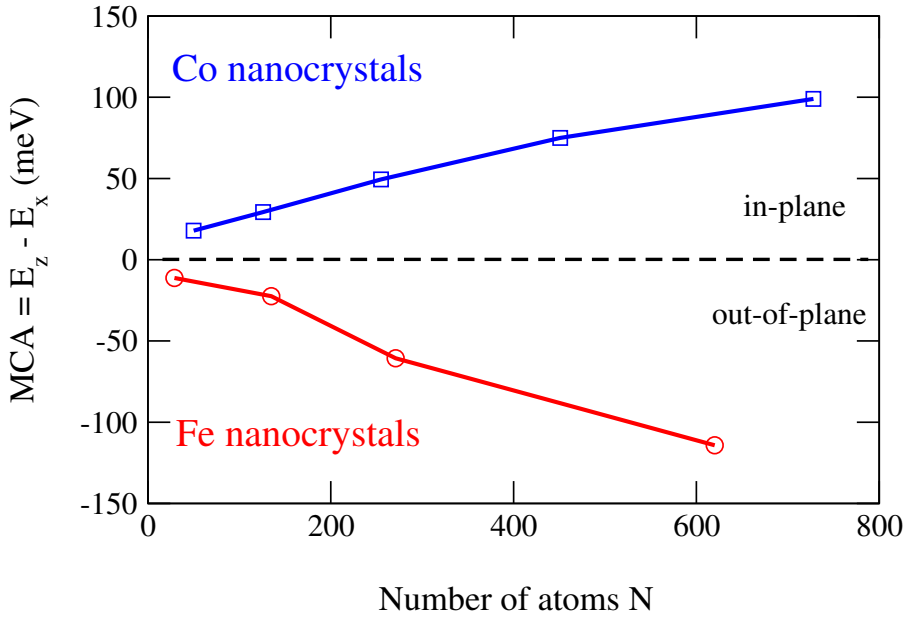

Figure 4.4: Total MCA of Co (blue circles) and Fe (red squares) nanocrystals .vs. the number of atoms. The size of nanocrystals was chosen so to keep a constant length-to-height ratio, 1.41 (Co) and ∼1.0 (Fe).

the band energy between magnetic solutions with magnetization along the z and x axis, explicitly, MCA $= E_z - E_x$. In terms of computational details, the lattice parameters of $a_0^{\mathrm{Fe}} = 2.85$ Å and $a_0^{\mathrm{Co}} = 3.53$ Å were used and no atomic relaxations were considered. In addition, the smearing parameter of 1 meV was employed which allows one to achieve an accuracy of ~ 0.1 meV for the total MCA. In Fig. 4.4, we plot the total MCA of Fe and Co nanocrystals of growing size calculated with TB approach. Interestingly, the total MCA is of the same order of magnitude for both Fe and Co nanocrystals, but opposite in sign, more precisely it is out-of-plane and in-plane easy axis for Fe and Co, respectively. We have also checked the total MCA in the xy plane but have found it extremely small, of amplitude about 3 meV and 0.8 meV for Fe (N = 620) and Co (N = 728) nanocrystals, respectively. This means that while the spin moment of Fe nanocrystals is fixed along the easy out-of-plane axis and needs to overcome the high MCA barrier to reverse from positive to negative direction, the magnetic moment of Co nanocrystals is allowed to rotate almost freely (with a very low in-plane magnetic anisotropy barrier) in the easy basal plane. As mentioned in Sec. 2.1, another important contribution to magnetic anisotropy is the so-called shape anistropy energy. It originates from the magnetic dipole-dipole interactions and can be calculated directly from atomic spin moment from self-consistent without spin-orbit coupling. we have calculated it for different size of the Fe and Co nanocrystals and have found much smaller value compared to its corresponding MCA (see ANNEXE D.2). Note that for both nanocrystals, the shape anisotropy energy favors in-plane magnetization. One can thus

conclude that the Fe nanocrystals are predicted to be more stable magnetically and are thus good potential candidates for magnetic storage devices.

4.2.3 Local analysis of MCA

In order to better explain the origin of MCA for nanocrystals, we performed a local analysis of MCA for the largest Fe nanocrystals made of 620 atoms, with 12 × 12 atoms on the lower base and 5 × 5 atoms on the upper face and containing eight atomic layers. Its length-to-height ratio of 1.14 is close to the experimental value of 1.20±0.12 [3].

In Fig. 4.5 we present the variation of the grand-canonical band energy with respect to the Euler polar angle θ between the magnetization direction and the z axis chosen to be perpendicular to its "roof" and base of (001) orientation (see inset). The azimuthal angle ϕ is kept zero so that the magnetization remains in the xz plane. The easy axis is evidently along the z and the total MCA is of the order of ~ 100 meV. We also checked the azimuthal anisotropy but found an extremely flat energy landscape in the xy plane with an amplitude of ~ 3 meV, the hard axis being along the diagonal of the base. To get more insight on the origin of the MCA we have decomposed the band energy per atomic site and analyzed the different contributions: total (solid black line), surface atoms (dashed black line), (001) facets (blue line) and perimeter of the base (red line) etc. By summing the local MCA over atomic sites in the outer shell of the nanocrystal (dashed black line), we almost recover the total MCA proving that only the outer shell (so called surface atoms) is participating to the anisotropy. A more detailed analysis showed only two significative contributions: i) low-coordinated perimeter atoms of the base (red line) and ii) two (001) facets, excluding perimeter atoms (blue line). Interestingly, the perimeter atoms of the base have the strongest anisotropy (see Tab. 4.1), while on the contrary, the contribution from the (110) side facets is almost negligible (and, moreover, cancel each other because of their opposite orientations). By counting the number of "implied" atoms [100 atoms of (001) surface and 44 atoms of perimeter of base], it is possible to extract an average anisotropy per (001) surface atom and per perimeter of base atom. One finds 0.55 meV/atom and 0.85 meV/atom for (001) and perimeter atoms, respectively. This corresponds quite well to the expected anisotropy found for the Fe(001) free-standing slabs as presented in Sec. 3.1.

In Tab. 4.1 we summarize the different contributions to the total MCA for the biggest Fe (N = 620) and Co (N = 728) pyramids. One can see that the total MCA mainly originates from the lower (001) facet and its perimeter composed of least coordinated atoms. Therefore, in agreement with the previous analysis of Fe(001) and Co(001) slabs, this would favor the out-of-plane and in-plane MCA for Fe and Co nanocrystals, respectively. We notice, moreover, that since nanocrystals of Co are much flatter than those of Fe (as Fig. 4.3 illustrates), which is a consequence of a larger length-to-height ratio for Co, the upper (001) facet, containing more atoms, gives noticeable contribution to the overall MCA in

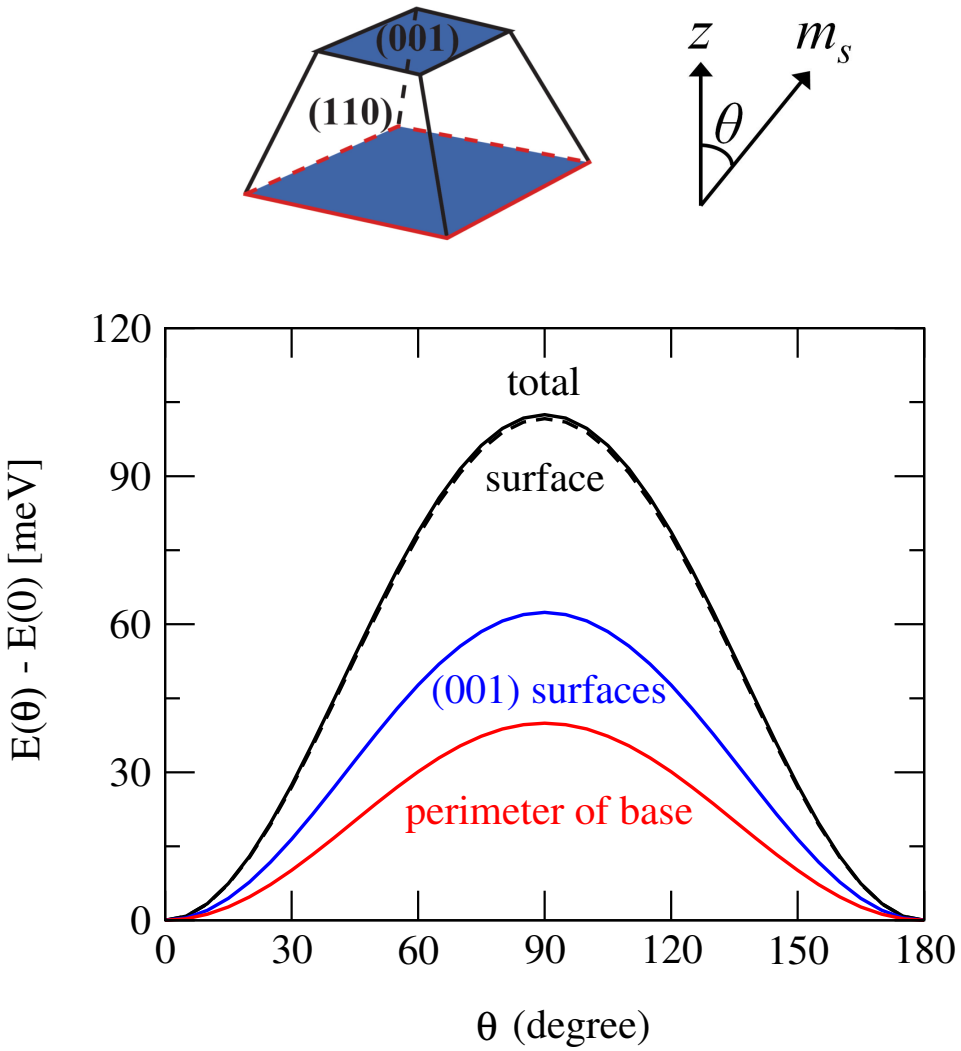

Figure 4.5: Magneto-crystalline anisotropy of a Fe truncted pyramid with N = 620 atoms, as a function of the angle θ between the z axis and the spin direction. Contributions from atoms of the two (001) facets and of perimeter of the base are shown in blue and red lines, respectively. The total MCA and the contribution from atoms of the outer shell (surface) are represented in solid and dashed black lines which are almost superposed. $E(\theta = 0)$ is taken as the zero of energy. Note that in all calculations the azimuthal angle ϕ is equal to zero.

	Fe (N = 620)			Co (N = 728)		
	MCA (meV)	MCA/atom (meV)	N	MCA (meV)	MCA/atom (meV)	N
upper perimeter	-4.8	-0.30	16	9.5	0.39	24
upper (001)	-3.7	-0.41	9	9.0	0.36	25
lower perimeter	-37.5	-0.85	44	40.1	0.84	48
lower (001)	-56.1	-0.56	100	40.1	0.33	121
side surfaces	-15.6	-0.08	180	1.1	0.00	180
total	-114.2	-0.18	620	99.0	0.14	728

Table 4.1: Local analysis of MCA for the biggest Fe (N = 620) and Co (N = 728) nanocrystals. Note that negative (positive) sign means out-of-plane (in-plane) magnetization.

the case of Co nanocrystals. In addition, the contribution of side facets are negligible for both elements.

4.2.4 MCA of truncated bipyramid

We then considered another type of nanocluster: a Fe truncated bipyramid (lower inset in Fig. 4.6) made of 1096 atoms and obtained by attaching symmetrically to the previous truncated pyramid another one (with removed base plane) from below. In Fig. 4.6 we have compared the total MCA of the two nanoclusters.

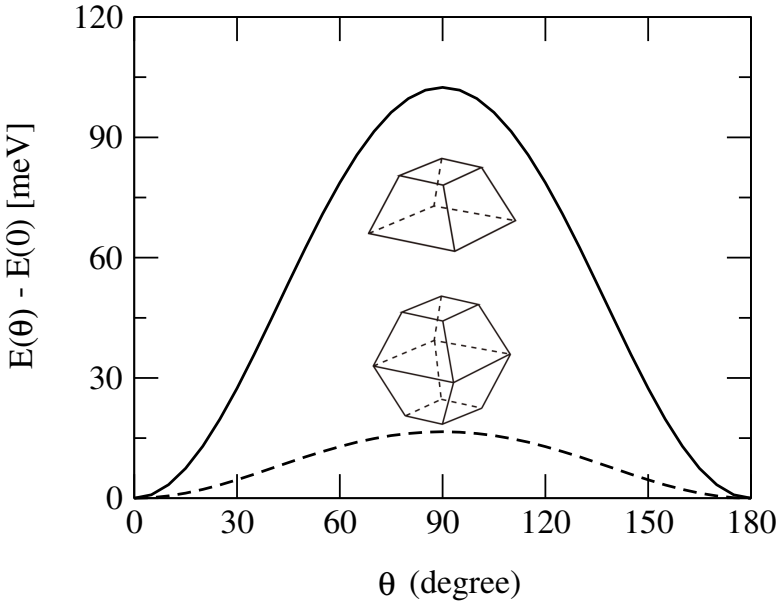

Figure 4.6: Total MCA as a function of angle θ for a Fe truncated pyramid (N = 620) and a Fe truncated bipyramid (N = 1020). For the latter one the MCA is strongly reduced because of the much smaller area of (001) facets.

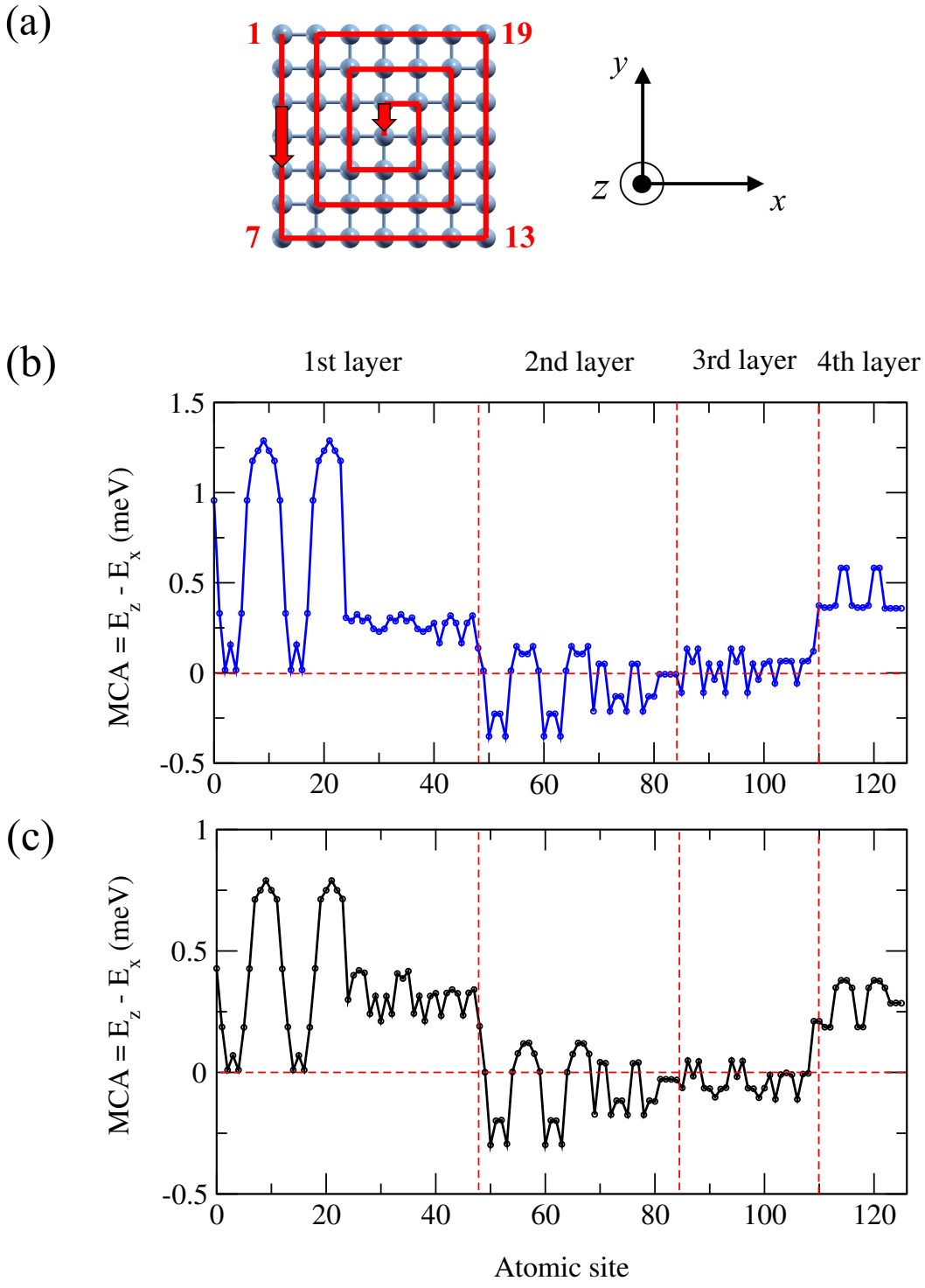

Figure 4.7: Atom-resolved MCA for Co nanocrystal made of 126 atoms: (a) trajectory for numbering the base layer atoms starting from the corner and going along the spiral to the center. The atoms of other layers are numbered in the similar way. (b) MCA per atom in meV within TB approach. (c) MCA per atom in meV from DFT-GGA calculations.

Although the truncated bipyramid contains more atoms, its MCA of about 15 meV is much lower than in the previous case. The explanation is quite straightforward from the previous analysis: the surface of the (001) facets has been strongly reduced and, moreover, the perimeter atoms of the base now have more neighbors and no longer contribute so strongly to the total MCA. The latter comes from two small (001) facets only. This argument works rather well: indeed, the number of atoms in (001) facets is now 18 atoms, which gives an anisotropy of $18 \times 0.56 \approx 10$ meV, a value slightly smaller than the overall MCA of about 15 meV, with the missing contribution coming from perimeter atoms which were not taken into account.

4.3 First-principles calculations

4.3.1 TB .vs. DFT

We have also performed a more detailed local analysis of MCA for a smaller Co nanocrystal made of 126 atoms (shown on the right panel of Fig. 4.3). For such a relatively small nanocrystal, *ab initio* DFT calculations within FT approach can be also carried out and compared with TB results. Fig. 4.8 reports the atom-resolved MCA for such pyramid. The atoms of each atomic layer are numbered starting from the corner and going anticlockwise along the spiral to the centre of the plane, as shown in Fig. 4.7 (a) for the base layer. The other layers are numbered in the same way. A qualitatively good agreement has been found between TB and DFT calculations. Interestingly, we found a sign change of MCA between atomic layers: the MCA favors in-plane magnetization for the first and forth layers and out-of-plane magnetization for the middle layers of the pyramid. The MCA achieves its highest values in the middle of two first layer edges aligned with the x axis, namely for 7-13 and 19-1 segments, and drops down to zero for two other edges. This asymmetry is due to chosen definition of MCA $= E_z - E_x$, since for the first pair of edges we compare the energies between orthogonal and parallel to the edge directions while for the second pair – between two perpendicular directions. Clearly, in the first case the energy difference will be much larger. Of course, if one chooses another definition of MCA, e.g., as the energy difference between the states with spin moment along the z axis and along the diagonal of the base plane, one would have more symmetric contributions from all four base edges.

4.3.2 Real-space distribution of MCA

To get more insight into the local decomposition of MCA, we have looked at its distribution in the real space as defined in Eq. 2.23 using local density of states. Such a real space representation of MCA for the previously studied 126 atoms Co pyramid is shown in Fig. 4.8. Interestingly, there are regions of both positive as well as negative MCA around each atom, in relative proportion which changes from layer to layer. Note that red (blue) colors correspond to in-plane (out-of-plane) magnetization. This leads, on average, to the change of sign for atomic MCA with respect to the layer observed in Fig. 4.7. We notice

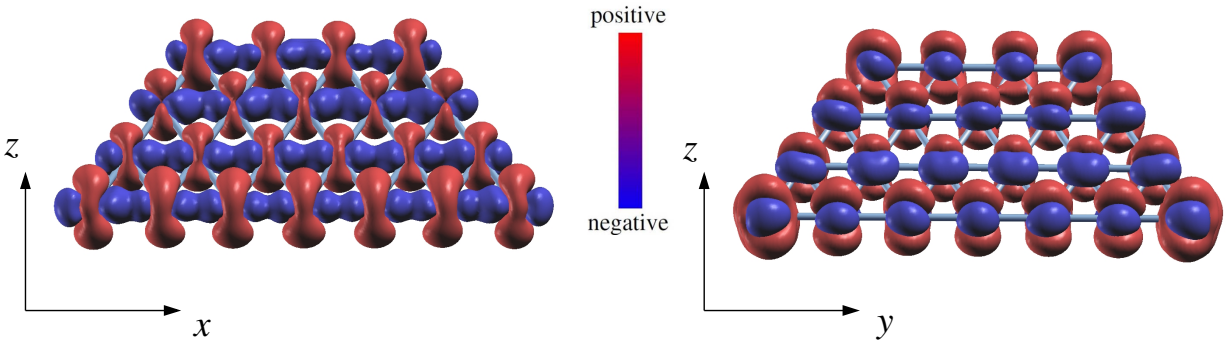

Figure 4.8: DFT calculations: Real-space distribution of MCA for Co nanocrystal of 126 atoms, side views. Two isosurfaces of positive and negative isovalues are shown in red and blue respectively.

moreover that positive and negative regions of MCA have different spatial localization: while the first one extends out of atomic planes (along the z axis) the second one is mostly localized in the xy plane. This is in agreement with the previous d-orbitals-resolved MCA of the fcc-Co(001) slab, showing in-plane MCA for d_{z^2} which extends along z axis while the orbitals extending in-plane ($d_{x^2-y^2}, d_{xy}$) lead to out-of-plane MCA (see Fig. 3.4). This observations can be important when studying the MCA modification due to deposition of pyramids on various substrates ($SrTiO_3$, Cu, Au, etc).

CHAPTER 5

MCA of ferromagnetic slabs and clusters supported on $SrTiO_3$

In this chapter, we present a detailed theoretical investigation of the electronic and magnetic properties of ferromagnetic slabs and clusters deposited on $SrTiO_3$ via first-principles, with a particular emphasis on the magneto-crystalline anisotropy (MCA). We found that in the case of Fe films deposited on $SrTiO_3$ the effect of the interface is to quench the MCA whereas for Cobalt we observe a change of sign of the MCA from in-plane to out-of-plane as compared to the free surface. We also find a strong enhancement of MCA for small clusters upon deposition on a $SrTiO_3$ substrate. The hybridization between the substrate and the d-orbitals of the cluster extending in-plane for Fe and out-of-plane for Co is at the origin of this enhancement of MCA. As a consequence, we predict that the Fe nanocrystals (even rather small) should be magnetically stable and are thus good potential candidates for magnetic storage devices.

The fine-tuning of the interfacial magneto-crystalline anisotropy (MCA) in ferromagnet-oxide insulator systems represents a key issue for several technological applications such as perpendicular magnetic tunnel junctions (p-MTJs) [125–127] and tunneling anisotropic magnetoresistive (TAMR) systems [8, 128]. It is well known that the physical origin of the MCA is the spin-orbit coupling (SOC). For the $3d$ transition-metals the SOC being of the order of a few tens of meV, the MCA per atom is extremely small (10^{-3} meV) in the bulk phase of cubic materials but can get larger ($\sim 10^{-1}$ meV) at surfaces/interfaces due to reduced symmetry. In order to obtain even larger MCA, traditionally, the MCA of nanostructures of $3d$ elements is enhanced by introducing $4d$ or $5d$ heavy elements with large SOC as a substrate such as Co/Pt [129] and Co/Pd [130] multilayers as well as in

small $3d$ clusters on heavy elements substrate [131]. However, despite the weak SOC at the interface, a strong MCA has been observed in Co and Fe thin films on metallic oxides such as AlO_x and MgO [132, 133]. The origin of this large MCA is attributed to electronic hybridization between the metal $3d$ and O-$2p$ orbitals [83]. More recently, Ran et *al*. have shown that it was possible to reach the magnetic anisotropy limit ($\sim$ 60 meV) of $3d$ metal atom by coordinating a single Co atom to the O site of an MgO surface [11].

In the previous chapter, we demonstrated that for both Fe and Co nanocrystals, the MCA of free nanocrystals is mainly dominated by the (001) facets resulting in an opposite behavior: out-of-plane and in-plane magnetization direction favored in Fe and Co nanocrystals, respectively. Therefore, the study of magnetic properties of nanocrystals deposited on a $SrTiO_3$ is essential, since depending on the bonding between the substrate and (001) facets this can influence greatly the overall behaviour of the nanocrystal. In this chapter, we report first-principles investigations of the MCA bcc-Fe(001) and fcc-Co(001) deposited on a $SrTiO_3$ substrate, namely Fe(Co)|$SrTiO_3$ interface. Next, we also investigated the MCA of very small (five atoms) Fe and Co clusters on $SrTiO_3$.

5.1 Fe(Co)|$SrTiO_3$ interfaces

5.1.1 Atomic structures and computational details

We carried out the first-principles calculations by using the plane wave electronic structure package QUANTUM ESPRESSO [28]. Generalized gradient approximation in Perdew, Burke and Ernzerhof parametrization [36] was used for electronic exchange-correlation functionals and a plane wave basis set with the cutoffs of 30 Ry and 300 Ry were employed for the wavefunctions and for the charge density, respectively. The Fe(Co)|$SrTiO_3$ interface was simulated by 10 layers of bcc-Fe(001)[fcc-Co(001)] slab deposited on a $SrTiO_3$(001) with 5 layers. The SrO and TiO_2 planes in the perovskite cubic $SrTiO_3$ alternate in the (001) direction, here $SrTiO_3$(001) surface was chosen to be TiO_2-terminated since it is energetically more favorable than SrO-terminated one [134]. The lattice constants of bulk bcc-Fe, fcc-Co and $SrTiO_3$ are 2.85, 3.531 and 3.93 Å, as compared to the experimental values of 2.87, 3.54 and 3.91 Å. When deposited on $SrTiO_3$ the in-plane lattice parameter of Fe(Co) slab is imposed by the one of bulk $SrTiO_3$ since it has been shown that the Co layer can nicely be grown on this substrate [135, 136]. In order to obtain a better match, the Fe and Co slabs are rotated by 45° with respect to the substrate, and each layer of the ferromagnetic slab is made of 2 atoms per supercell. The TiO_2 layer at the interface in Fe(Co)|$SrTiO_3$ is denoted as **S** (see Fig. 5.1). Layers toward the $SrTiO_3$ bulk are labeled as **S**-1, **S**-2, etc., while Fe(Co) layers towards the surface are labeled as **S**+1, **S**+2, **S**+3, etc.

In the ionic relaxation, the Brillouin-zone has been discretized by using 10 $\times$ 10 in-plane k-points mesh and a smearing parameter of 0.01 Ry. Two bottom layers of $SrTiO_3$ were fixed while other three layers of substrate and ferromagnetic slabs were relaxted until the atomic forces are less than 10^{-3} eV/Å. We found that the most stable configuration

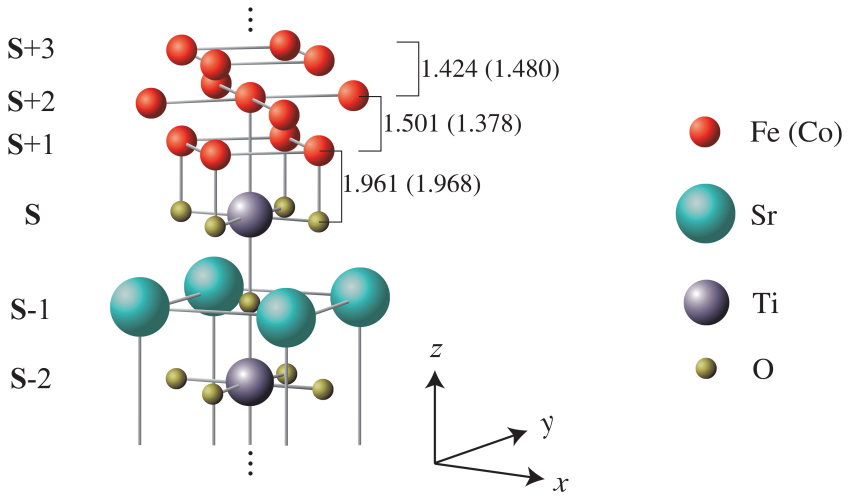

Figure 5.1: Atomic structure of bcc-Fe(001) and fcc-Co(001) slabs on top of TiO_2-terminated (001) surface of $SrTiO_3$. The ferromagnetic slab is rotated by 45° with respect to substrate in order to better match with the $SrTiO_3$ lattice. Note that each layer of ferromagnetic slabs is made of 2 atoms per supercell. Layers **S**+3, ..., **S**-2 are shown and the distances in the z direction between different layers are also indicated.

is, in all cases, where the Fe(Co) sites in layer **S**+1 are on top of the O sites in layer **S** with the distance of 1.961(1.968) Å. This is in agreement with previous study in Ref. [137]. We used 12 Å of vacuum space in the z direction in order to avoid the unphysical interactions between two adjacent elementary unit cells. The mismach with $SrTiO_3$ was found to be about -2.5 and 10.1 % for Fe and Co, respectively. The Fe and Co slabs have been strained and relaxed to accomodate the lattice structure of the $SrTiO_3$ substrate, respectively. As a result, one finds that the distances beween **S** and **S**+1 of about 1.501 Å and 1.378 Å which should be compared with the bulk values of 1.425 Å and 1.765 Å for Fe and Co, respectively.

To obtain reliable values of MCA, the convergence of calculations has been carefully checked. The MCA was calculated from the band energy difference using force theorem, a mesh of 20 × 20 in-plane k-points has been used for SCF calculation with scalar-relativistic PPs with a smaller smearing parameter of 0.005 Ry. In non-SCF calculation with full-relativistic PPs including SOC the mesh was increased to 60 × 60 and smearing parameter was reduced to 0.001 Ry which provides an accuracy of MCA below 10^{-2} meV.

5.1.2 Magnetic spin moment

We plot in Fig. 5.2 the local spin moments of free Fe(Co) slab (blue circles) but the ionic positions are the one obtained after relaxation in presence of $SrTiO_3$(001). In this way we can evaluate the role of the relaxation on the free surface as well as at the interface. The local spin moments of the full system Fe(Co)|$SrTiO_3$(001) are shown in red squares.

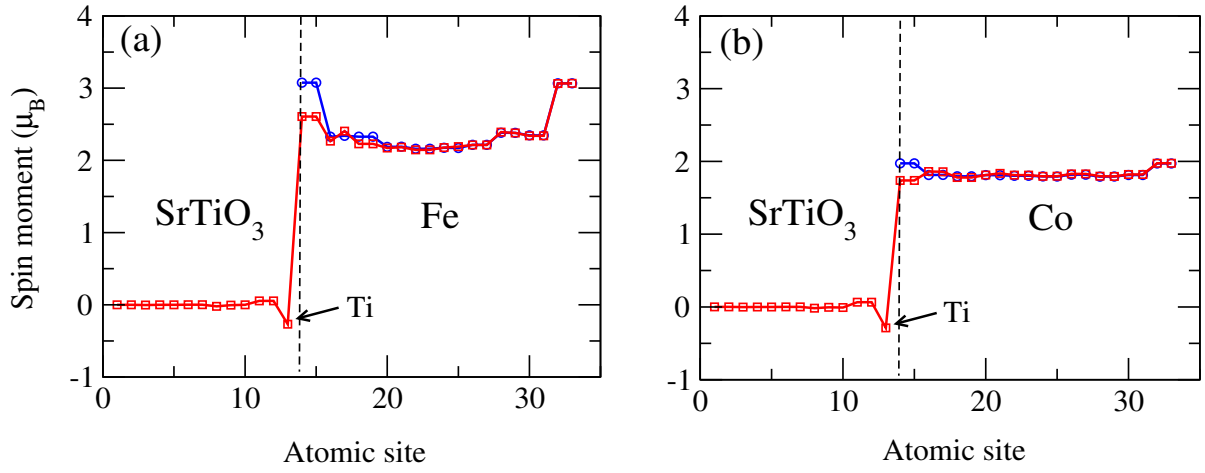

Figure 5.2: Layer-resolved magnetic spin moment (in μ_B) at Fe|SrTiO$_3$(001) (a) and Co|SrTiO$_3$(001) (b) interfaces. Blue circles and red squares correspond to free slab and slab on SrTiO$_3$ substrate, respectively.

For free slabs, the magnetic moment of **S**+1 layer are enhanced up to 3.07 and 1.97 μ_B with respect to their bulk values of 2.15 and 1.79 μ_B in **S**+5 layer for Fe and Co, respectively. However, in the case of Fe(Co)|SrTiO$_3$, the surface spin moment is reduced to 2.61 and 1.74 μ_B (it is even smaller than its bulk value) due to bonding and charge transfer at the interface. In addition, the hybridization between Fe 3*d* and states of TiO$_2$ at the interface induces spin moments for Ti and O atoms. It has been found that the induced magnetic moment of the interface O atom in **S** layer is $\sim$ 0.05 (0.06) μ_B and is parallel to the magnetic moment of Fe(Co). A much larger induced but opposite spin moment in **S** layer has been found on Ti atoms :$\sim$ -0.27 (-0.29) μ_B

5.1.3 Electronic properties

In order to explain the origin of the induced magnetic moments at the interface, we investigated the electronic structure (PDOS) of the free Fe(Co) slab as well as the Fe(Co)|SrTiO$_3$ interface compared to the corresponding PDOS in bulk phase of bcc-Fe (fcc-Co) and SrTiO$_3$.

As shown in Fig. 5.3 (a), the DOS of the interfacial Fe(Co) 3*d* (**S**+1) for free slab differs from the DOS of the bulk Fe(Co) 3*d* (**S**+5) (the shaded plot) as a result of the reduced coordination. A significant minority spin states at $\sim$ 0.1 and 0.7 eV (-0.4 and 0.2 eV) with respect to the Fermi level has been found for the surface.These states are the origin of the increase of spin moment for the surface atom.

Fig. 5.3 (b) - (d) show the PDOS of Fe(Co) 3*d* (**S**+1), Ti 3*d* (**S**) and O 2*p* (**S**) orbitals at Fe(Co)|SrTiO$_3$ interface, indicating the presence of hybridizations between the orbitals. It is well known that the degree of hybridization at the interface depends on the strength

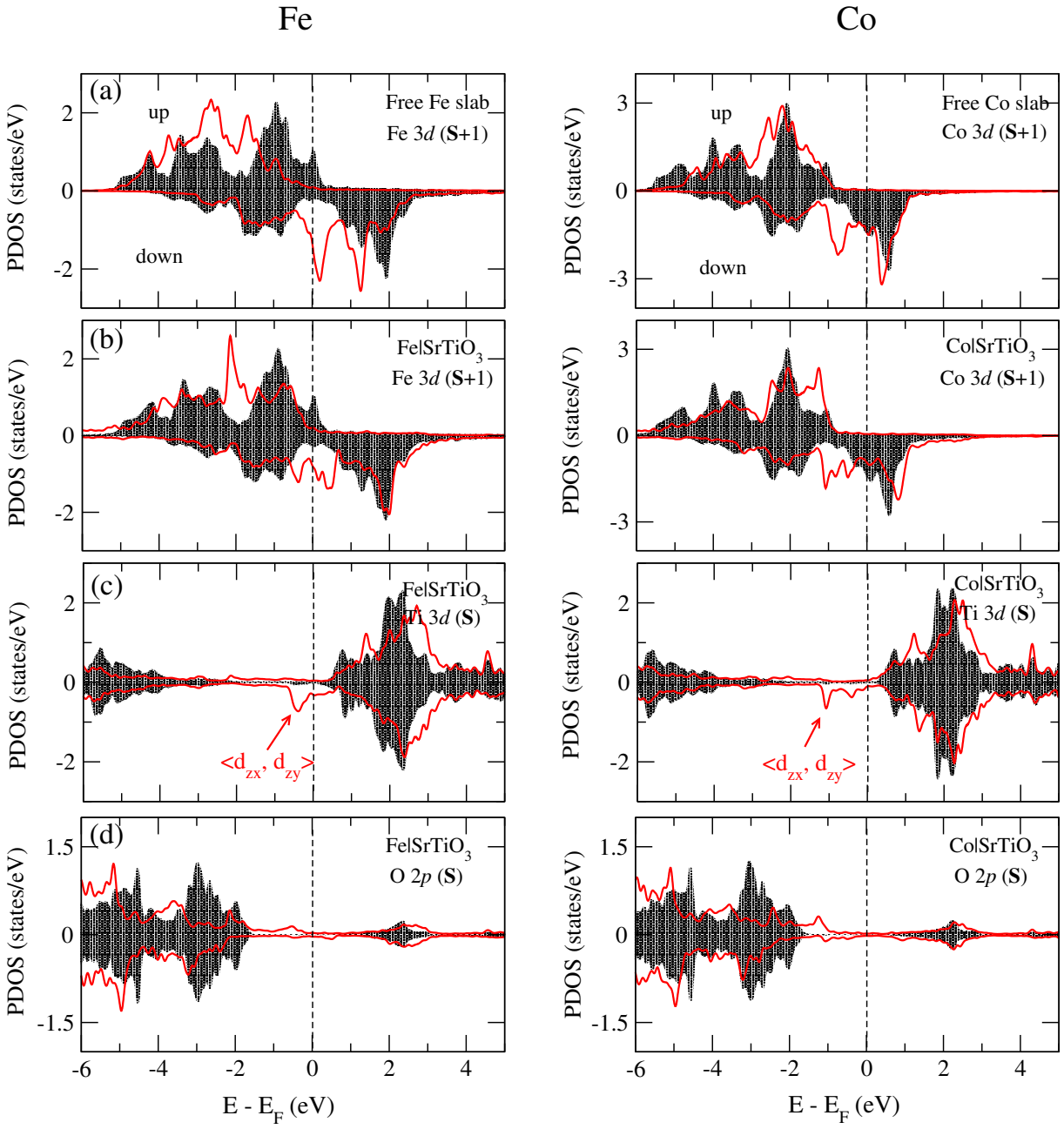

Figure 5.3: (a) Free Fe slab: Scalar-relativistic projected density of states (PDOS) of the surface Fe 3*d* orbitals in layer **S**+1; Fe|$SrTiO_3$(001): PDOS of (b) Fe 3*d* orbitals in layer **S**+1, (c) Ti 3*d* and (d) O 2*p* orbitals in layer **S**. The shaded plots are the DOS of atoms in the central monolayer of Fe slab (a, b) or (c, d) TiO_2 in layer **S**-2. Positive and negative PDOS are for spin up and spin down channels, respectively. The vertical dashed lines indicate the Fermi level (E_F). It is the same for Co as presented in the right panels.

of the orbital overlap and inversely on the energy seperation between them. Although there is a direct atomic bonding between the interfacial Fe(Co) and O atoms, the induced magnetic moment on the O atom was found to be relatively small ($\sim$ 0.05 μ_B). This is due to the fact that O 2p (**S**) orbitals lie well below the Fermi level and, therefore, have a small overlap with the Fe(Co) 3d states. However, the Ti 3d orbitals that are centered at about 2 eV above the Fermi level [the shaded plot in Fig. 5.3 (c)] have a strong hybridization with the minority-spin Fe(Co) 3d orbitals which have a significant weight at these energies [the shaded plot in Fig. 5.3 (b)]. The most important consequence of this hybridization is the formation of the hybridized states in the interval of energies [-0.5, +0.5] eV and [-1, +1] eV for Fe and Co, respectively. As shown in Fig. 5.3 (c), the DOS of the Ti 3d **S** layer at the Fe(Co)|$SrTiO_3$ interface, the minority-spin states which originates from the d_{zx} and d_{zy} orbitals at $\sim$ -0.5 eV (the two peaks at -1 eV and -0.5 eV) are occupied, whereas the corresponding majority-spin states are found at $\sim$ +1.5 eV (the two peaks at +0.5 eV and +1 eV) are inoccupied. This leads to an induced magnetic moment of -0.27 and -0.29 μ_B on the Ti (**S**) for Fe and Co based interfaces, respectively.

5.1.4 Local analysis of MCA

We now investigate the MCA of the Fe(Co)|$SrTiO_3$ interface. The MCA is calculated as band energy difference between the spin quantization axes perpendicular and parallel to the slab surface, explicitely, MCA = $E_{\perp}^{\text{band}} - E_{\parallel}^{\text{band}}$, and for the sake of simplicity we have chosen the most symmetric in plane orientation. By definition a positive (negative) sign in MCA means in-plane (out-of-plane) magnetization axis. It should be noted that, the full relativistic Hamiltonian including spin-orbit coupling is given in a basis of total angular momentum eigenstates $|j, m_j\rangle$ with $j = l \pm \frac{1}{2}$. Although the (l, m_l, m_s) is not a well defined quantum number for the full relativistic calculations, the MCA can still be projected into different orbital and spin by using local density of states. Since the spin-orbit coupling in 3d-electron systems is relatively small, this approximate decomposition introduces a negligible numerical inaccuracy.

As shown in Fig. 5.4 (a) and (b), we have calculated the atom-resolved MCA of the Fe(Co)|$SrTiO_3$ system (red squares) and compared it with the free Fe(Co) slab (blue circles) containing 10 atomic layers (but relaxed in presence of the substrate). For free Fe(Co) slab, the total MCA reaches $\sim$ -0.49 (1.60) meV per unit-cell favouring an out-of-plane (in-plane) axis of magnetization. If the Fe(Co) slab is in contact with $SrTiO_3$ substrate, the axis of magnetization is preserved but the total MCA is reduced to $\sim$ -0.38 (1.02) meV.

From the atom-resolved MCA, one finds that the MCA curves for free slabs are not symmetrical, particularly pronouced for Co, due to (asymmetrical) relaxation effect. The main contribution to MCA is located in the vicinity of the interface, from **S** layer to **S**+3 layer, marked as vertical dotted line in Fig. 5.4 (a) and (b), and it converges to the expected bulk value in the center of the slab (**S**+5 layer). Interestingly, at the interface, in comparison with free Fe(Co) slab it appears that the contact with $SrTiO_3$ strongly favors in-plane and out-of-plane for Fe and Co, respectively.

For Fe(**S**+1), upon adsorption on $SrTiO_3$, the MCA decreases from $\sim$ -0.15 to $\sim$ -0.06

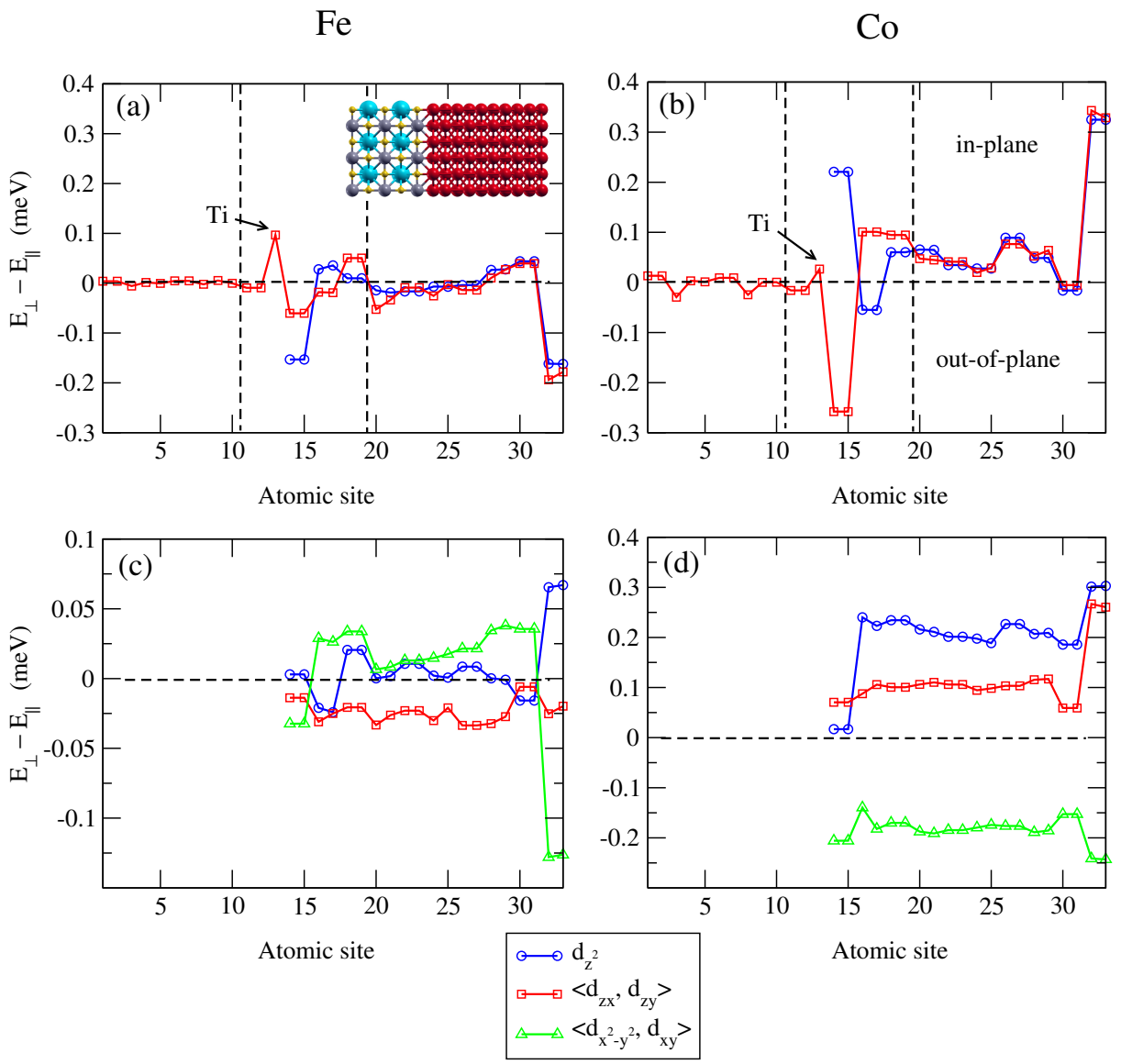

Figure 5.4: Atom-resolved MCA at Fe|SrTiO$_3$ (a) and Co|SrTiO$_3$ (b) interfaces, blue circles and red squares correspond to free slab and slab on a SrTiO$_3$ substrate, respectively. d-orbitals-resolved MCA for Fe (c) and Co (d) slabs on SrTiO$_3$, we plot only the part of ferromagnetic slabs. Due to symmetry, contributions from different orbitals in (d_{zx}, d_{zy}) and $(d_{x^2-y^2}, d_{xy})$ pairs are very similar so that their averaged values are presented for simplicity. Note that positive and negative MCA represent in-plane and out-of-plane magnetization, respectively.

meV/atom and the out-of-plane magnetization remains. However, in the case of Co(**S**+1), the MCA abruply changes from $\sim$ 0.22 to $\sim$ -0.25 meV/atom exhibiting magnetization reversal from in-plane to out-of-plane at the same time. For **S**+2 layer, we find a sign change of MCA between free slab and slab on $SrTiO_3$ for both elements, with the MCA difference of $\sim$ 0.04 meV/atom and $\sim$ 0.15 meV/atom for Fe and Co, respectively. For **S**+3 layer, the MCA enhances slightly ($\sim$ 0.05 meV/atom) in-plane MCA when depositing slabs on $SrTiO_3$ for both elements. Furthermore, the Ti atom in **S** layer [indicated by arrows in Fig. 5.4 (a) and (b)] presents a strong in-plane MCA of $\sim$ 0.1 meV/atom and a much smaller in-plane MCA of $\sim$ 0.03 meV/atom for Fe and Co-based interfaces, respectively. As a result, for free slabs, the MCA values from **S**+1 layer to **S**+3 layer sum up to the total value of $\sim$ -0.22 meV (out-of-plane) and 0.45 meV (in-plane) for Fe and Co. However, when the slabs are supported on $SrTiO_3$, the overall out-of-plane MCA in the vicinity of the surface (here, the **S** layer is also taken into account) is almost quenched for Fe by $\sim$ 0 meV, and in the case of Co, a spin transition from in-plane to out-of-plane magnetization has been found with a MCA value of $\sim$ -0.10 meV.

In order to understand the origin of this difference in MCA between free Fe(Co) slab and Fe(Co)|$SrTiO_3$ system, we investigated the d-orbitals-resolved MCA of the Fe(Co) atom as shown in Fig. 5.4 (c) and (d). Here, due to symmetry, the contributions to MCA from (d_{zx}, d_{zy}) and $(d_{x^2-y^2}, d_{xy})$ pairs are almost equal, therefore, their averaged values are presented for simplicity. As shown before in Fig. 5.3, close to the Fermi level, the shape of the electron density for O and Ti suggest that this density has a p_z character and d_{zx} (d_{zy}) character, respectively.

In the case of Fe, we notice that from free Fe slab to Fe|$SrTiO_3$ system, the MCA from d_{z^2} (in-plane magnetization) and $(d_{x^2-y^2}, d_{xy})$ (out-of-plane magnetization) orbitals decreases in magnitude, while the MCA of (d_{zx}, d_{zy}) orbitals are almost not affected. In addition, quantitatively, the reduction of MCA is much larger in $(d_{x^2-y^2}, d_{xy})$ than in d_{z^2} due to stronger hybridization between (Fe-$d_{x^2-y^2,\ xy}$, Ti-$d_{zx,\ zy}$) orbitals than between (Fe-d_{z^2}, O-p_z) orbitals. Moreover, the strong in-plane MCA in Ti (**S**) layer originates from the Ti-$d_{zx,\ zy}$ orbitals since there is a significant weight close to Fermi level for minority-spin (Ti-$d_{zx,\ zy}$) orbitals [see Fig. 5.3 (c) left panel]. As a result, the MCA at the interface appears to almost quench the out-of-plane magnetization when the Fe slab is deposited on $SrTiO_3$. Moreover, if we sum over the contribution of the first three layers of Fe slab at the interface, we found that d_{zx}, d_{zy} orbitals tend to maintain the out-of-plane MCA while $d_{x^2-y^2,\ xy}$ orbitals tend to favor the in-plane MCA. A similar result has also been reported in Ref. [138] in Fe|MgO magnetic tunnel junctions.

In the case of Co, we find that the hybridization between p_z orbitals of O and d_{z^2} (and, to a slightly lesser extent with $d_{zx,\ zy}$) of Co plays a crucial role to decrease in-plane MCA of the free Co slab. On the other hand, the MCA from in-plane ($d_{x^2-y^2,\ xy}$) orbitals of Co is less affected due to rather small minority-spin states of (Ti-$d_{zx,\ zy}$) close to the Fermi level [see Fig. 5.3 (c) right panel]. This leads to induce an inverse spin orientation transition from in-plane to out-of-plane in Co|$SrTiO_3$ system. A similar result has also been reported in Ref. [95] at C_{60}|Co interface.

5.2 Fe and Co clusters on $SrTiO_3$

5.2.1 Atomic structures and computational details

The first-principles calculations were performed again using plane-wave-basis-set QUANTUM ESPRESSO within the generalized gradient approximation (GGA) for exchange-correlation functionals in Perdew, Burke and Ernzerhof parametrization [36]. Energy cutoffs of 30 Ry and 300 Ry were employed for the wavefunctions and the charge density, respectively. The interface was simulated by a (4×4) in-plane TiO_2-terminated $SrTiO_3(001)$ substrate with 5 atomic layers containing one Fe(Co) cluster made of 5 atoms. Two bottom layers were fixed while other three layers of substrate and Fe(Co) cluster were relaxed until atomic forces are less than 10^{-3} eV/Å. For both scalar and full relativistic calculations, a $(8\times8\times1)$ k-points mesh and a smearing parameter of 10^{-3} Ry was used. In addition, the effect of unphysical interaction in the direction z was minimized by taking a vacuum space of about 15 Å.

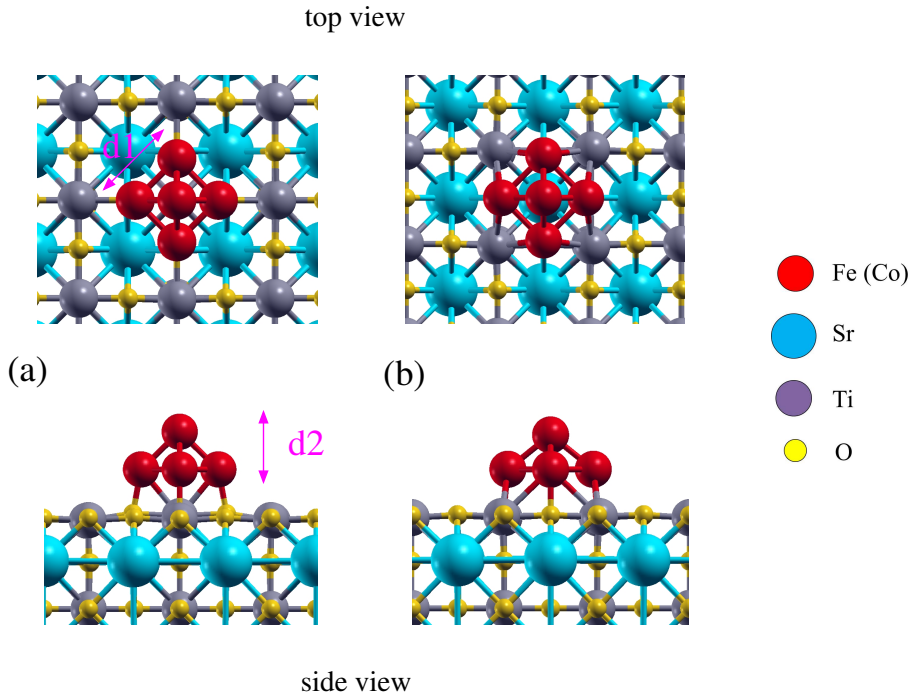

Figure 5.5: Top (upper panels) and side (lower panels) views of the optimized geometries of Fe and Co cluster absorbed on TiO_2-terminated $SrTiO_3(001)$. Two different adsorption configurations are presented in (a) and (b), the latter one is the most stable configuration for both Fe and Co clusters. The bond length d_1 between base atoms and the vertical distance d_2 between base and top atoms are indicated.

As shown in Fig. 5.5, two geometries are examined, namely top (a) and hollow (b) adsorption sites. The base atoms of Fe(Co) clusters are always on top of O atom for both

geometries however the apex atom is either on top of a Ti atom (top geometry) or of an underneath Sr atom (hollow geometry). We found that a hollow adsorption site is more energetically stable for both elements, with an energy difference of ~ 0.65 eV and ~ 0.88 eV for Fe and Co, respectively. In the following, we concentrate on the lowest energy configuration.

The strength of the cluster-$SrTiO_3$ interaction can be quantified by calculating the binding energy via the energy difference:

$$E_\mathrm{b} = E[\mathrm{cluster}] + E[\mathrm{SrTiO_3}] - E[\mathrm{cluster|SrTiO_3}] \tag{5.1}$$

where E[cluster], E[$SrTiO_3$] and E[cluster|$SrTiO_3$] are the total energy of the free cluster, the free $SrTiO_3$ substrate and the cluster-$SrTiO_3$ system, respectively. The calculated binding energy was found to be ~ 4.23 (4.58) eV for Fe(Co) cluster on $SrTiO_3$ substrate, showing strong chemisorption mechanism (see Tab. 5.1).

	Fe		Co	
	Free cluster	Cluster on $SrTiO_3$	Free cluster	Cluster on $SrTiO_3$
E_b (eV)	—	4.23	—	4.58
d_1 (Å)	2.31	2.55	2.17	2.20
d_2 (Å)	1.73	1.45	1.80	1.74
$M_\mathrm{s}^\mathrm{tot}$ (μ_B)	18.00	16.63	13.00	7.67
$\lvert M_\mathrm{s}^\mathrm{tot}\rvert$ (μ_B)	18.34	17.96	13.41	11.06
$M_\mathrm{s}^\mathrm{base}$ (μ_B)	3.62	3.33	2.54	1.75
$M_\mathrm{s}^\mathrm{top}$ (μ_B)	3.58	3.32	2.84	1.57

Table 5.1: Binding energies (E_b), atomic bonds, total/total absolute spin moments ($M_\mathrm{s}^\mathrm{tot}/|M_\mathrm{s}^\mathrm{tot}|$), spin moment of base ($M_\mathrm{s}^\mathrm{base}$) and top ($M_\mathrm{s}^\mathrm{top}$) atoms of the free clusters and clusters deposited on $SrTiO_3$ for the lowest energy configuration.

Compared to free Fe cluster, the Fe-Fe distance in basal plane (d_1) is elongated from 2.31 Å to 2.55 Å while the Fe-Fe distance in vertical distance from apex to basal plane (d_2) is compressed from 1.73 Å to 1.45 Å (see Tab. 5.1). However, in the case of Co, the geometry optimization of $Co_5|SrTiO_3$ results in a rather small (negligible) distortion compared to its free Co_5 cluster. In addition, the atomic bond between Fe(Co) and O is length of ~ 2 Å.

5.2.2 Magnetic spin moment

We next investigated the local magnetic spin moment. In Tab. 5.1, the local spin moments for both free clusters and the clusters on $SrTiO_3$ are given. The binding between Fe(Co) and O atoms reduces the total spin moment from 18.00 μ_B (free Fe_5) to 16.63 μ_B

and from 13.00 μ_B (free Co_5) to 7.67 μ_B for the deposited clusters. We also calculated the absolute total spin moment $|M_s^{tot}|$ and compared to corresponding total spin moment M_s^{tot}. Interestingly, a substantial difference of ~ 3.4 μ_B has been found between $|M_s^{tot}|$ and M_s^{tot} for $Co_5|SrTiO_3$. In order to understand the origin of this difference, we plot in Fig. 5.6 the real-space distribution of magnetic spin moment of Co cluster on $SrTiO_3$. Note that the red (blue) corresponds to positive (negative) spin moment. We can see clearly the negative magnetic moment is mainly localized on Ti atoms at the interface and around the Co top atom of cluster. However, for Fe cluster, the positive spin moment is very localized on the Fe atoms and the negative part is negligible.

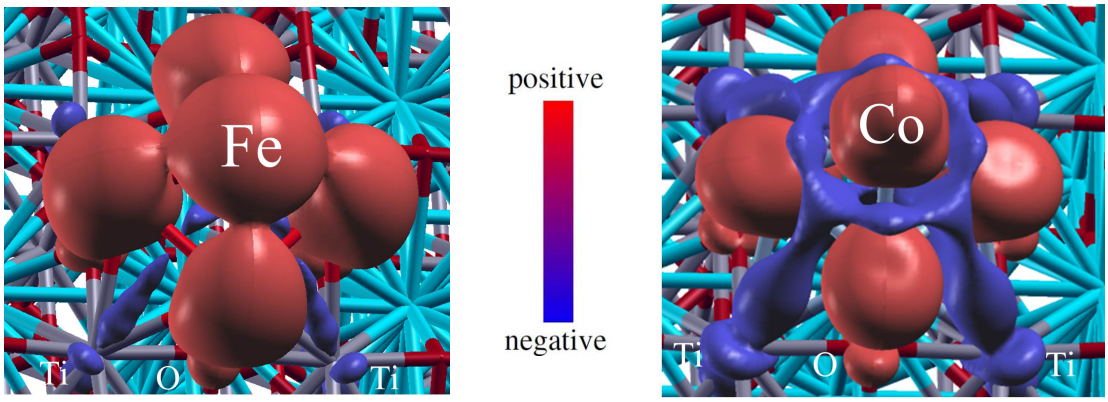

Figure 5.6: Real-space distribution of magnetic spin moment of Fe (left) and Co (right) cluster on $SrTiO_3$. Note that red (blue) corresponds to positive (negative) spin moment. The nonnegligible negative part of spin moment has been found around the Ti atoms at the interface and the Co top atom of cluster.

5.2.3 Electronic structure properties

To gain more insight into the electronic structure of $Fe_5|SrTiO_3$ and $Co_5|SrTiO_3$, we plot the scalar-relativistic projected density of states (PDOS) on d orbitals of Fe(Co) base atom and top atom of the cluster in Fig. 5.7 (a) and (b).

For the base atom of both clusters, the density of majority states is almost completely occupied and negligibly small around the Fermi level, while the density of minority states is partially occupied. Around the Fermi level, there is a higher density of $(d_{x^2-y^2}, d_{xy}, d_{zy})$ states for Fe while the most dominant states are the out-of-plane d orbitals for Co, namely $(d_{z^2}, d_{zx}, d_{zy})$ orbitals. For top atom, in the interval of energies [-0.25, +0.25] eV, the density of states for both majority and minority spins is negligibly small for both clusters.

Although the PDOS analysis is very instructive no experiment can provide a direct information on this quantity. Nevertheless, the spin-polarized scanning tunneling spectroscopy (SP-STS) can probes the evanescent local density of states (LDOS) in the vacuum. It can

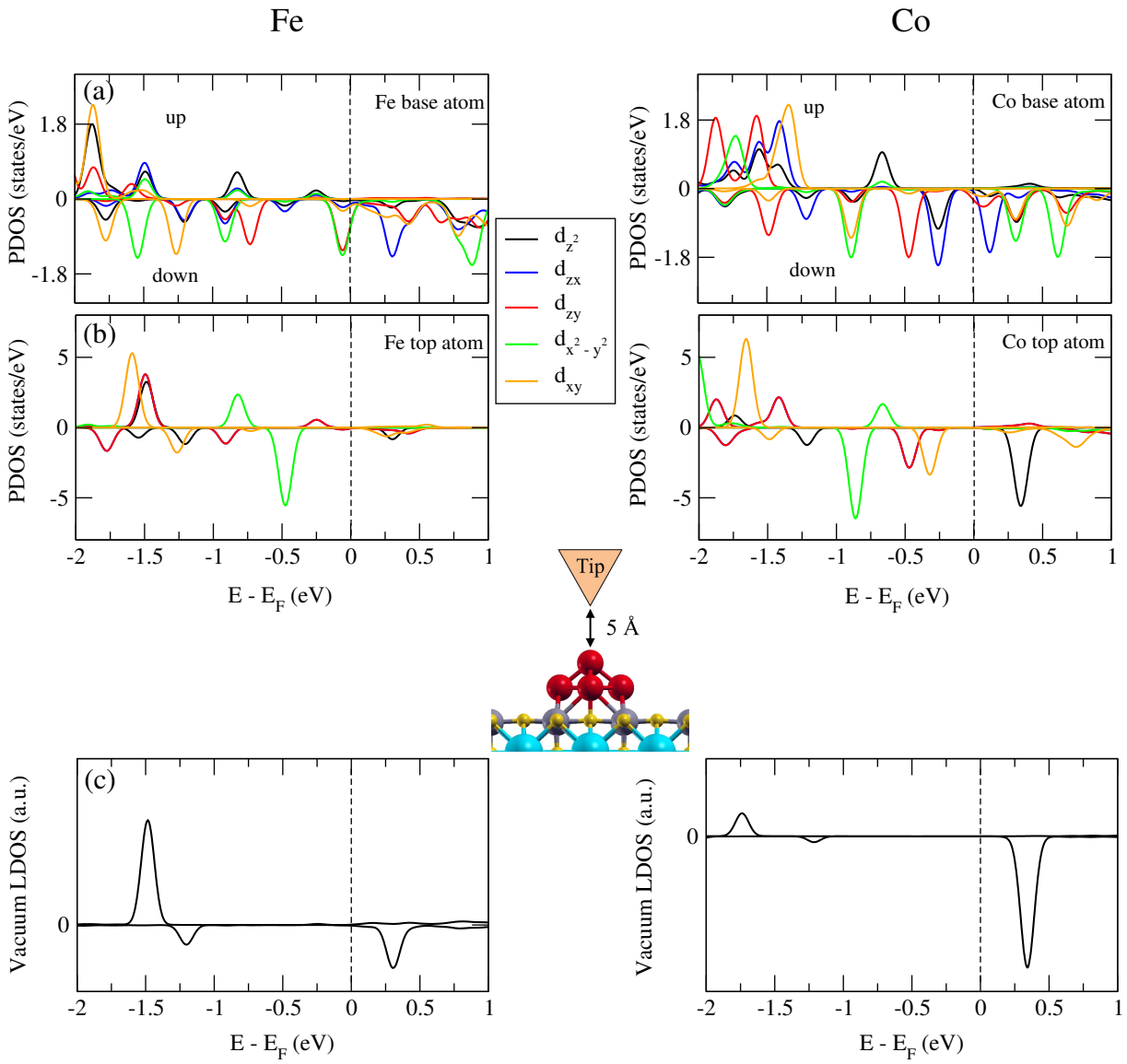

Figure 5.7: Scalar-relativistic *d*-orbitals projected density of states (PDOS) for Fe(Co) base atom (a) and top atom (b) of the cluster absorbed on $SrTiO_3$, (c) spin-resolved vacuum local density of states (LDOS) at 5 Å above the cluster (see inset). Positive and negative PDOS are for spin up and spin down channels, respectively. The vertical dashed lines mark the Fermi level (E_F)

be simulated by using Tersoff and Hamann approach generalized to spin-polarized STM [139]. The SP-STS is then simply related to spin-resolved LDOS of the sample and tip.

$$G = \frac{dI}{dV}(R_{\mathrm{T}}, V) \propto \sum_{\sigma} n_{\mathrm{T}}^{\sigma} n_{\mathrm{S}}^{\sigma}(R_{\mathrm{T}}, E_{\mathrm{F}} + eV) \tag{5.2}$$

where n_{T}^{σ}, $n_{\mathrm{S}}^{\sigma}(R_{\mathrm{T}}, E_{\mathrm{F}} + eV)$ are spin-dependent tip DOS (assumed to be constant in energy) and vacuum LDOS of the sample (cluster deposited on surface) calculated at the tip position R_{T} above the cluster and at the energy corresponding to applied voltage V, respectively. In practice the vacuum LDOS presented in Fig. 5.7 (c) is calculated by integrating $n_{\mathrm{S}}^{\sigma}(R_{\mathrm{T}}, E)$ inside a small cubic box of size 0.4 Å at 5 Å above top atom of the cluster for both spin up and down.

Interestingly we noticed that for both clusters a sharp peak corresponds to the d_{z^2}-like minority spin states of top atom has been found at about 0.3 eV with respect to the Fermi level. Since these states are rather close to the Fermi level the largest magnetic contrast could be probed by SP-STS experiments at a bias voltage of 0.3 eV.

5.2.4 Local analysis of MCA

The MCA is calculated by the formula MCA $= E_z^{\mathrm{band}} - E_{x'}^{\mathrm{band}}$ using as usual the magnetic force theorem. The MCA in the xy plane is found to be extremely small. we have chosen the most symmetric in-plane direction x' (see Fig. 5.8) which has an azimuthal angle of $\phi = 45°$ with respect to x. Due to symmetry, this definition gives us almost similar contribution for each pair of (d_{zx}, d_{zy}) and of $(d_{x^2-y^2}, d_{xy})$ Fe(Co) orbitals, therefore, their averaged values are presented for the sake of simplicity.

In Fig.5.8 (a) and (b) the local decomposition of MCA with different atomic sites as well as with different d-orbitals is presented for $Fe_5|SrTiO_3$ and $Co_5|SrTiO_3$, respectively. Note that only the contributions of clusters is shown. Interestingly, we find the opposite behavior of MCA for Fe and Co clusters deposited on $SrTiO_3$. The easy axis of magnetization is directed along out-of-plane for Fe cluster with a total MCA of $\sim$ -5.08 meV, on the contrary it is in-plane for Co with a total MCA of $\sim$ 4.72 meV. For both elements, the atomically resolved MCA (black lines) reveals that the MCA is mainly dominated by the base atoms (numbered as 1 $\sim$ 4) and a relatively much smaller contribution from the top atom (numbered as 5). The value of MCA per atom is as large as $\sim$ -1.22 (1.08) meV/atom for base atom and $\sim$ -0.18 (0.38) meV/atom for the top atom of Fe(Co) cluster.

It is also interesting to note that the MCA mainly originates from the d-orbitals of the cluster extending in-plane for Fe, namely $(d_{x^2-y^2}, d_{xy})$ orbitals, and out-of-plane for Co, namely, $(d_{z^2}, d_{zx}, d_{zy})$. From the perturbation treatment of MCA as mentioned in Sec. 2.2.3, the dominant contribution to the MCA comes from the coupling between occupied and unoccupied eigenstates near the Fermi level through the spin-orbit coupling [16, 17, 140]. The sign of the MCA can probably be explained by taking into account the most important transition (occupied-unoccupied) through a second order pertrubation expansion but such analysis remains very qualitative.

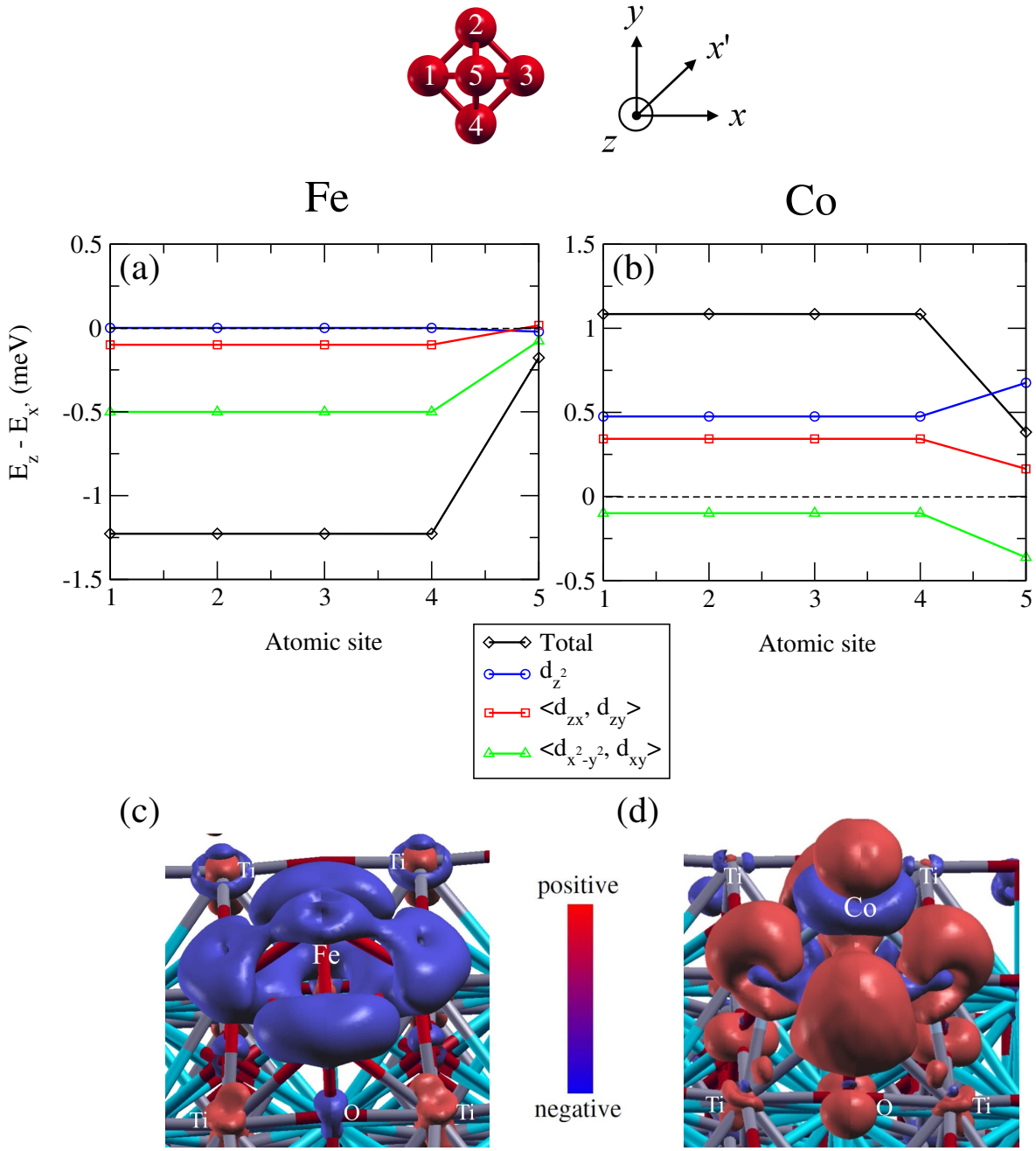

Figure 5.8: Atom/d-orbitals-resolved MCA of Fe (a) and Co (b) clusters deposited on $SrTiO_3$. Due to symmetry, contributions from different orbitals in (d_{zx}, d_{zy}) and $(d_{x^2-y^2}, d_{xy})$ pairs are very similar so that their averaged values are presented for simplicity. Clear out-of-plane and in-plane MCA have been found for Fe and Co clusters, respectively. Real-space distribution of MCA for Fe (c) and Co (d) clusters is given. Note that red (blue) colors represent the regions favoring in-plane (out-of-plane) magnetization orientation. The MCA mainly from the base atoms for both clusters, and for Fe (Co) the MCA originates from d-orbitals of the cluster extending in-plane (out-of-plane).

Finally in Fig. 5.8 (c) and (d), we present the real-space distribution of MCA for $Fe_5|SrTiO_3$ and $Co_5|SrTiO_3$. The red colors represent in-plane magnetization direction, whereas the blue colors are out-of-plane easy axis. We can see clearly, the MCA mainly comes from the base atoms for both clusters, and for Fe(Co) the MCA originates from *d*-orbitals of the cluster extending in-plane (out-of-plane). In addition, due to hybridization between the states of TiO_2 surface and *d*-orbitals of the cluster, the Ti and O atoms close to the cluster gives a rather small contribution to MCA. For Fe, Ti atom slightly favors the in-plane easy axis and the easy axis of O atom is out-of-plane. In the case of Co, both Ti and O atoms around the cluster favor to in-plane magnetization direction.

As a consequence, we predict that the Fe_5 nanocrystals should be magnetically stable and are thus good potential candidates for magnetic storage devices.

Conclusion

We investigated the MCA of Fe and Co nanocrystals, which can be grown experimentally by epitaxy on $SrTiO_3$ substrate, using tight-binding and first-principles calculations in the density functional theory (DFT) framework. The former approach allows handling very big clusters, up to several thousands of atoms. In order to define a proper local decomposition of MCA, we implemented the force theorem approach within the grand-canonical formulation in our magnetic tight-binding model and QUANTUM ESPRESSO code. A relatively good agreement has been found between the MCA obtained from tight-binding and first-principles calculations. In addition, the MCA is calculated using the force theorem which was checked to work very well due to the small SOC in Fe and Co-based systems.

We first studied the MCA of bcc-Fe and fcc-Co bulk slabs of different crystallographic orientations which form the facets of the nanocrystals. Interestingly, we find the opposite behavior for Fe and Co slabs: while the total MCA is out-of-plane/in-plane for Fe(001)/ Fe(110) slabs it is, on the contrary, in-plane/out-of-plane for Co(001)/Co(111) ones. The local analysis reveals that the MCA is mainly dominated by outer planes, a small contribution from the sub-surface layers gives rise, however, to an oscillatory behavior for large thicknesses which originates from the sub-surface contributions. This kind of oscillatory dependence of MCA on the film thickness can be explained in terms of quantum well states and has also been observed experimentally in thin ferromagnetic films [74, 90, 91].

Next, we investigated free Fe and Co nanocrystals having the shape of truncated pyramids. From the local analysis it was found that the MCA of free nanocrystals is largely dominated by (001) facets resulting in the opposite behavior: out-of-plane and in-plane magnetization direction is favored in Fe and Co nanocrystals, respectively. Moreover, the largest contribution is coming from the perimeter atoms of the base facet of the pyramid. In agreement with the previous analysis of the slabs this favors the out-of-plane/in-plane anisotropy for Fe/Co nanoclusters, respectively.

In order to understand the substrate effect on Fe(001) and Co(001) surfaces which give the dominant contribution for the free nanocrystals, we investigated Fe(Co)|$SrTiO_3$ interfaces. At the interface, we found that the $SrTiO_3$ favors in-plane MCA for Fe and out-of-plane MCA for Co. In particular, in the first layer of Co slab at the interface, the

spin-orientation from in-plane to out-of-plane has been found.

We also find a strong enhancement of out-of-plane and in-plane MCA for small Fe and Co clusters (containing only several atoms) upon deposition on a $SrTiO_3$ substrate. The hybridization between the substrate and the *d*-orbitals of the cluster extending in-plane for Fe and out-of-plane for Co is at the origin of this enhancement of MCA. As a consequence, we predict that the Fe nanocrystals (even rather small) should be magnetically stable and are thus good potential candidates for magnetic storage applications.

As a perspective, it has been shown that the shape of surface anisotropy could have consequences on the magnetization reversal in nanoparticles [141]. Therefore it is very likely that a detailed investigation of the spin dynamics of nanocrystals could reveal such surface effects in the anisotropy. So far, the deposited nanocrystals are not very peoriodic in experiments, however highly ordered long range arrays of nano-magnets can be obtained by using tunable supramolecular networks to host the shape-selected magnetic nanocrystals. The hybridization between nanocrystals and hosting molecules could result in the change of the magnetism. Thus it is interesting to study the MCA for such hybrid organo-ferromagnetic nanoarchitectures. Finally, our implementation of the force theorem is rather general and can be applied to many other systems. In particular, the local analysis of MCA has recently allowed us to interpret and predict the MCA behavior of ferromagnetic surfaces and its modification upon covering by organic overlayers, such as C_{60} molecules [95].

APPENDIX A

Convergence tests: Force theorem

Since the MCA is a very small quantity, careful tests have been performed to check its numerical convergence with respect to the various computational parameters. In the force theorem (FT) approach adopted in this work, the first step is to perform a SCF calculations without SOC. The computational parameters for this first collinear calculation are less drastic than the one including SOC. Typical vallues are presented in Sec. 2.3.1 and were found enough to obtain a well converged charge density and spin magnetization. In the following, we will present the convergence tests for the MCA only (*i.e.* including SOC) and our system is the bcc-Fe(001) slab contaning 10 atomic layers. We start by the tight-binding model followed by the DFT calculations.

A.1 Tight-binding

Before discussing the convergence tests it is important to validate the force theorem approach used throughout this manuscript. In Fig. A.1 we show the total MCA as a function of the number of layers of Fe (001) slabs obtained from a full SCF calculation (including SOC) and the FT approach. An almost perfect agreement is obtained between the two approaches proving the validity of the force theorem.

The first parameter to be checked is the density of the k-mesh sampling that is controled by the number of k-points in the the first Brillouin zone. We have used the so-called Marzari-Vanderbilt (MV) mesh which is a uniform sampling of k-space. The system is a slab of rectangular lattice and the k-mesh is characterized by only one parameter n_k corresponding to a MV sampling (n_k, n_k).

The convergence of the MCA with respect to n_k is shown in Fig. A.2. We found that $n_k = 80$ is sufficient to obtain a precision for the MCA below 10^{-2} meV. For this calcuation the remaining parameters (in particular the level smearing) have been kept constant and

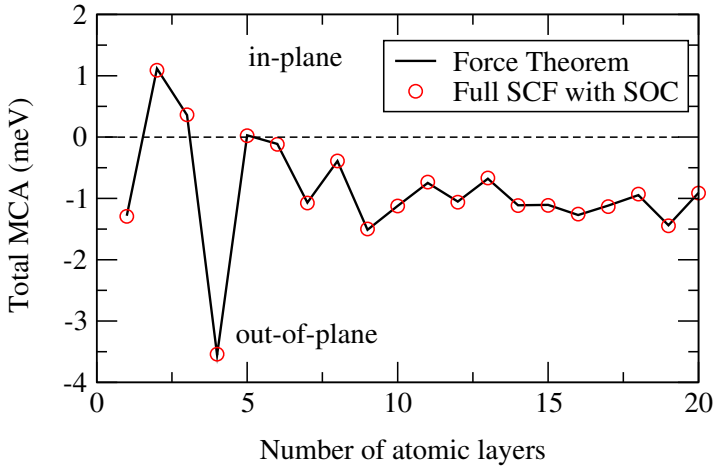

Figure A.1: TB results: MCA of a bcc-Fe(001) slab (per unit surface cell) as a function of its thickness N. The Force theorem (solid black lines) is compared to the full self-consistent filed calculations including SOC (red circles). Excellent agreement has been found.

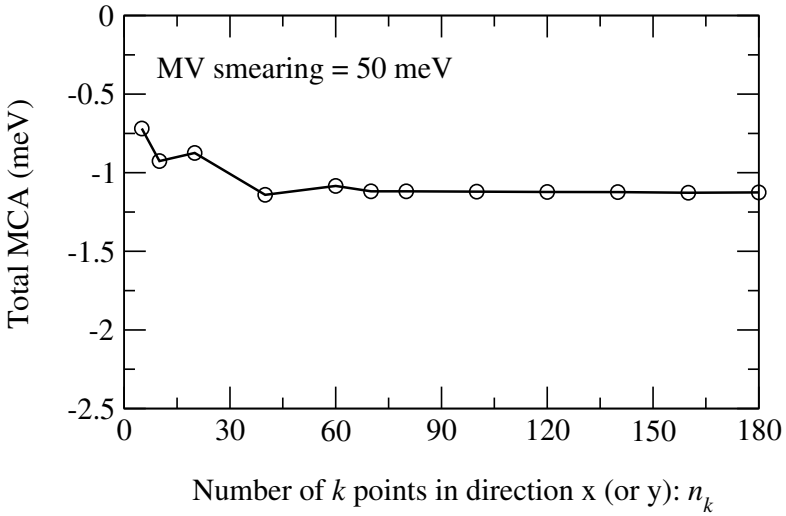

Figure A.2: TB results: Convergence of the total MCA with respect to the density of the k-points mesh sampling (n_k, n_k) for a bcc-Fe(001) slab containing 10 atomic layers.

equal to "reasonable" values (see Sec. 2.3.1).

A.2 DFT calculations

We performed the DFT calculations by using Quantum Espresso package [28]. In DFT calculations of MCA the most important parameters that have to be considered are the number of k-points, the planewave cutoff for the expansion of the wavefunction and the smearing parameters. The other parameters are kept constant and equal to "reasonable" values.

In Fig. A.3 we present the variation of the total MCA with the number of k-points. Four calculations (5×5, 10×10, 20×20, 30×30, 40×40, 50×50) were compared to the calculation with the highest number of k-points that was performed (60×60). We found that 40×40 was sufficient to obtain a precision of MCA below 10^{-2} meV.

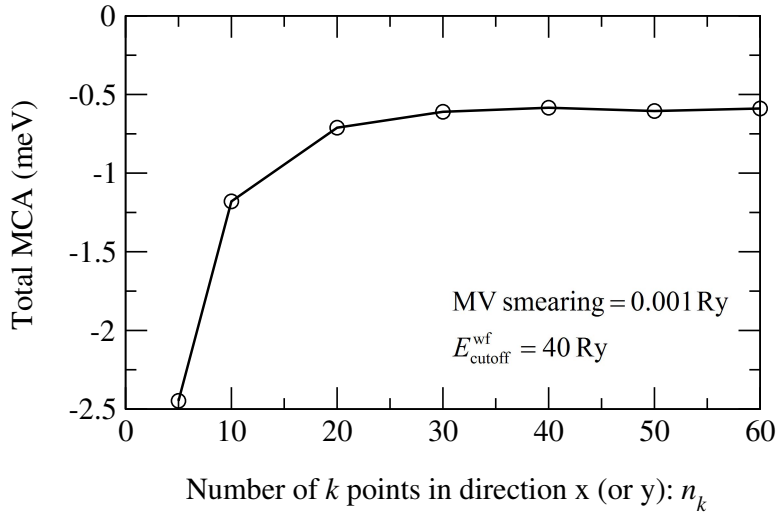

Figure A.3: DFT results: Convergence of the total MCA with respect to the density of the k-points mesh sampling (n_k, n_k) for a bcc-Fe(001) slab containing 10 atomic layers.

In DFT the planewave cutoff for the expansion of the K-S orbitals determines the number of basis functions. The basis set can be systematically improved by increasing number of planewaves. From Fig. A.4 we notice only a slight oscillating behavior of the total MCA for kinetic energy cutoff above 30 Ry. In this thesis we used the planewave cuoff of 40 Ry with a convergency of MCA below 10^{-1} meV.

Another parameter which has been tested is the smearing parameter, we plot in Fig. A.5 the convergence of total MCA with respect to the different values of smearing parameters (ranging from 0.001 to 0.01 Ry). Interestingly the "Marzari-Vanderbilt" technique and the "Methfessel-Paxton" agree for smearing parameters below 0.002 Ry but can differ by more

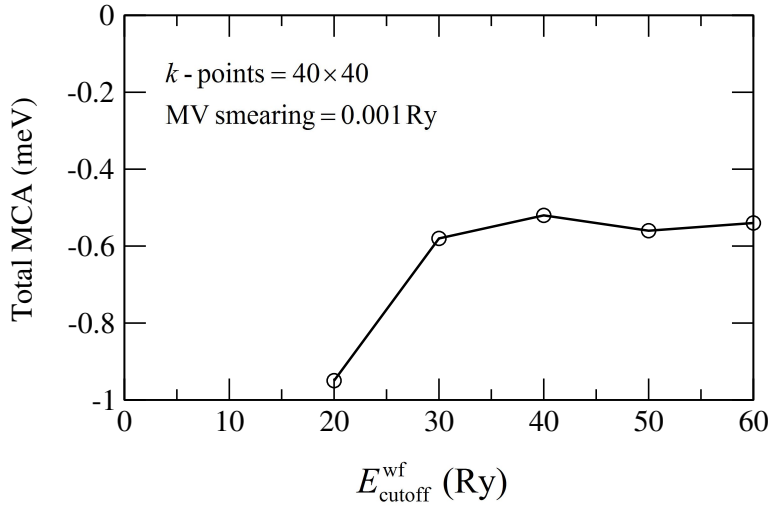

Figure A.4: DFT results: Convergence of total MCA with respect to the kinetic energy cutoff for wavefunctions for a bcc-Fe(001) slab containing 10 atomic layers.

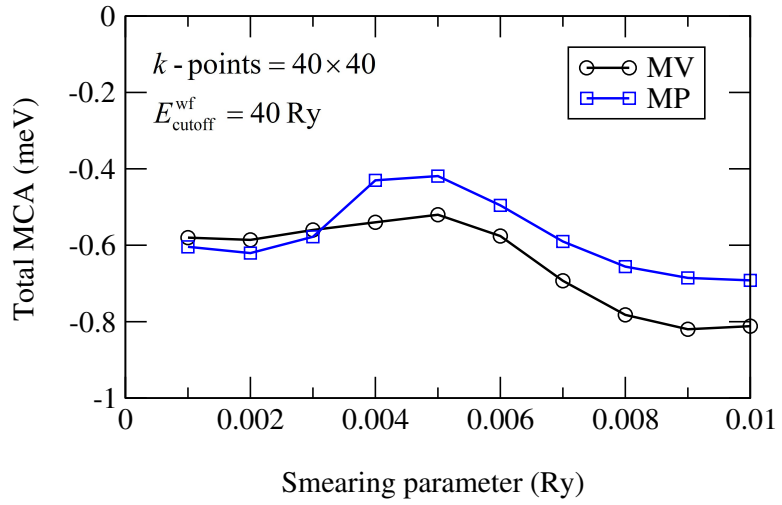

Figure A.5: DFT results: Convergence of total MCA with respect to smearing parameters for a bcc-Fe(001) slab containing 10 atomic layers, two different smearing techniques are presented, namely "Marzari-Vanderbilt" (black circles) and "Methfessel-Paxton" (blue squares).

than 0.1meV for larger smearings. In this thesis we used a Marzari-Vanderbilt broadening scheme with 0.001 Ry broadening

APPENDIX B

The 1D quantum well

To illustrate the difference between FT and $\mathrm{FT_{gc}}$ let us consider one of the simplest models, a one-dimensional free-electron gas bounded within a length L by infinite barriers. The normalized wave functions and the corresponding discretized eigenvalues are (atomic units in which $\hbar^2 = 2m = e^2/2 = 1$ are used):

$$\psi_k(z) = \sqrt{\frac{2}{L}} \sin kz \quad \epsilon_k = k^2 \quad \text{with} \quad k = p\frac{\pi}{L} \tag{B.1}$$

where p takes only positive integer values. For the unbounded electron-gas with periodic Born-Von Karman (BVK) boundary conditions:

$$\psi_k^{\mathrm{BVK}}(z) = \sqrt{\frac{1}{L}} e^{ikz} \quad \epsilon_k = k^2 \quad \text{with} \quad k = 2n\frac{\pi}{L} \tag{B.2}$$

In that case n take any postive or negative integer values including 0. In the continuum limit the excess energy due to the creation of two surfaces is given by:

$$\Delta E = 2 \times \frac{L}{\pi}\Big[\int_0^{k_F+\delta k_F} \epsilon_k dk - \int_0^{k_F} \epsilon_k dk\Big], \tag{B.3}$$

where the factor 2 is due to the spin degeneracy and $k_F = \frac{\pi N}{2L}$ (N is the total number of electrons in the box of the length L) is the Fermi wave vector of the unbounded homogeous gas. Since an electron at $k = 0$ is not allowed in the case of quantum well, it should be instead placed on the next free level, which leads to $\delta k_F = \frac{\pi}{2L}$ and thus $\Delta E = k_F^2 = E_F$. Local decomposition of ΔE is naturally achieved by weighting each energy eigenvalue in Eq. B.3 by the squared modulus of the corresponding wave function which results in:

$$\Delta E(z) = -\frac{2}{\pi}\int_0^{k_F} k^2 \cos(2kz) dk + \frac{2k_F^2}{L} \sin^2(k_F z) \tag{B.4}$$

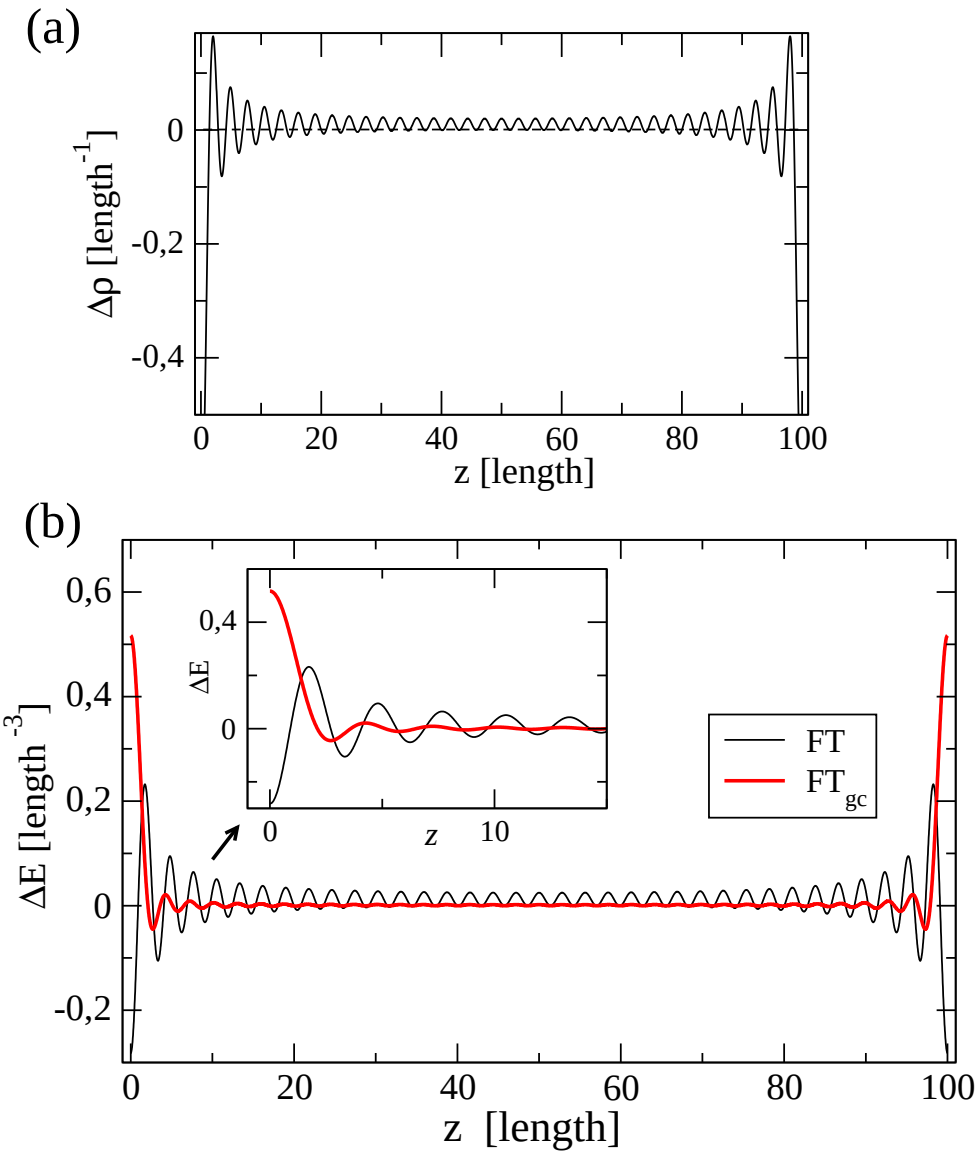

Figure B.1: Graphical representation of the functions $\Delta E(z)$, $\Delta E_{\mathrm{gc}}(z)$, and $\Delta\rho(z)$ for a one-dimensional electron gas confined by infinite barriers in the box of the length L. The discretized calculations were done with the parameters $N = 70$ (total number of electrons) and $L = 100$.

Equivalently, a grand-canonical formulation gives:

$$\Delta E_{\rm gc}(z) = -\frac{2}{\pi}\int_0^{k_F}(k^2-k_F^2)\cos(2kz)dk\Big] \tag{B.5}$$

Simple integration leads to exact expressions for $\Delta E(z)$ and $\Delta E_{\rm gc}(z)$:

$$\Delta E_{\rm gc}(z) = \frac{1}{\pi}\Big(\frac{\sin(2k_Fz)}{2(k_Fz)^3}-\frac{\cos(2k_Fz)}{(k_Fz)^2}\Big)E_Fk_F \tag{B.6}$$

$$\Delta E(z) = \Delta E_{\rm gc}(z)-\frac{\sin(2k_Fz)}{\pi z}E_F+\frac{2\sin^2(k_Fz)}{L}E_F \tag{B.7}$$

$$\tag{B.8}$$

These expressions, illustrated in Fig. B.1, are quite instructive. Within the $\mathrm{FT_{gc}}$ formulation the density of surface energy behaves like $1/z^2$ for large z. The case of the FT formulation is more tricky: it contains, in addition, a term slowly decaying as $1/z$ and a term which does not decay (for a given L) but tends to zero as L goes to infinity. In fact, these two last terms are simply proportional to the surface excess electronic density:

$$\Delta\rho(z) = -\frac{\sin(2k_Fz)}{\pi z}+\frac{2\sin^2(k_Fz)}{L} \tag{B.9}$$

so that $\Delta E(z) = \Delta E_{\rm gc}(z) + E_F\Delta\rho(z)$. Therefore, we conclude that the long-range Friedel oscillations in $\Delta\rho(z)$ are at the origin of the slow convergence with z observed for the FT $\Delta E(z)$ which is perfectly in line with our previous analysis of layer-resolved magnetic anisotropies as illustrated by the striking similarities between Fig. 2.1 and Fig. B.1.

APPENDIX C

Length to height ratio of nanocrystals

The experimentalists showed that the self-assembled Fe and Co nanocrystals by epitaxy have the shape of truncated pyramids with a well defined ratio of length (l) of the top square to the height (h) for different sizes of the nanocrystals (see the inset of Fig. C.1). The length to height ration is found to be $\sim$ 1.20 and $\sim$ 1.48 for Fe and Co nanocrystals, respectively.

In the case of bcc-Fe nanocrystals, the inter-atomic distance in the same layer is a_0^{Fe} while the interlayer distance is $a_0^{\mathrm{Fe}}/2$, where a_0^{Fe} is the lattice parameter of bcc-Fe bulk. The length to height ratio can be written as follows:

$$\frac{l}{h}\Big|_{\mathrm{Fe}} = \frac{2(n_1 - 1)}{n_2 - n_1}, \tag{C.1}$$

where $n_2 \times n_2$ and $n_1 \times n_1$ are the number of atoms in the first (bottom) and last (up) layers of the truncated pyramids.

In the fcc structure the atoms can pack closer together than they can in the bcc structure. The inter-atomic distance and interlayer distance in fcc-Co nanocrystals are $a_0^{\mathrm{Co}}/\sqrt{2}$ and $a_0^{\mathrm{Co}}/2$, respectively. Note that a_0^{Co} is the lattice parameter of fcc-Co bulk. The length to height ratio can be written as follows:

$$\frac{l}{h}\Big|_{\mathrm{Co}} = \frac{\sqrt{2}(n_1 - 1)}{n_2 - n_1}, \tag{C.2}$$

In Fig. C.1 we plot the l/h of Fe (left) and Co (right) nanocrystals with respect to n_2 for a given n_1. We then selected different sizes of nanocrystals (up to several hundreds of atoms) by using experimental value (plotted as the dotted lines) of l/h. For Fe nanocrystals, the l/h is found to be $\sim$ 1.0 which is close to the experimental value of 1.20 [3], more precisely $l/h = 1.0$ for $N = 29$, 135; 1.20 for $N = 271$; 1.14 for $N = 620$, where N is the total number of the nanocrystal. The l/h for different sizes of Co nanocrystals is equal

to 1.41 close to experimental value of 1.48. The biggest Fe and Co nanocrystals which we have calculated containing 620 and 728 atoms with 8 and 7 atomic layers, respectively. From the value of l/h we can see that the Co nanocrystals are flatter than those of Fe.

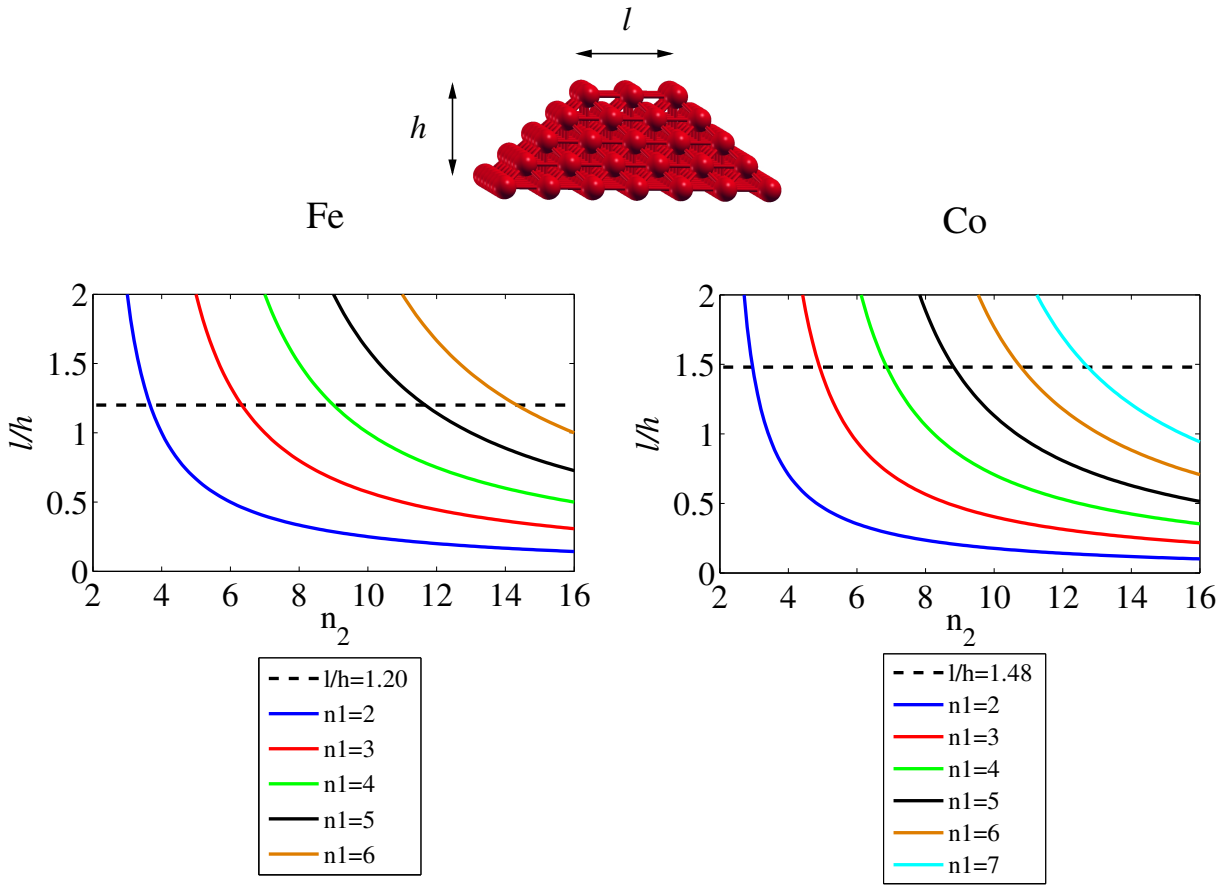

Figure C.1: The ratio of the length (l) of the top square to the height (h) of the Fe (left) and Co (right) trancated pyramids with respect to n_2 as a given n_1. Note that $n_2 \times n_2$ and $n_1 \times n_1$ are the number of atoms in the first (bottom) and last (up) layers of the truncated pyramids. The experimental value of l/h is also indicated as a black dotted line.

APPENDIX D

Shape anisotropy

As explained in Sec. 2.1, an important contribution to magnetic anisotropy energy (MAE) is the shape anisotropy. The shape anisotropy is calculated numerically by using the magnetic dipole-dipole interaction energy:

$$E_{\text{dip}} = \frac{\mu_0}{8\pi} \sum_{i \neq j} \frac{1}{r_{ij}^3} \left[\mathbf{M_i} \cdot \mathbf{M_j} - 3 \frac{(\mathbf{r_{ij}} \cdot \mathbf{M_i})(\mathbf{r_{ij}} \cdot \mathbf{M_j})}{r_{ij}^2} \right]. \tag{D.1}$$

with M_i the atomic spin moment at site i (obtained in practice by a tight binding or DFT calculation) and r_{ij} the distance between atoms i and j. The summation runs in principle over all atoms in systems, but in practice we have introduced a cut-off radius. Since we are not dealing with really large systems we did not use any computational trick to speed up our calculations and the summation is performed in a straightforward manner.

D.1 Fe and Co free-standing slabs

The shape anisotropy essentially depends upon the shape of the sample and it becomes important in elongated system such as thin films for which it systematically favors in-plane alignment of the magnetization. Here, the shape anisotropy, ΔE_{dip}, is defined as the energy difference between magnetic dipolar interaction energy for $\mathbf{M}$ perpendicular and parallel to the atomic slabs. Explicitely, $\Delta E_{\text{dip}} = E_{\perp}^{\text{dip}} - E_{\parallel}^{\text{dip}}$.

Since the shape anisotropy is a long range interaction as it varies in $1/r_{ij}^3$, first of all we checked carefully the convergence of the shape anisotropy with respect to the cutoff radius, $r_{ij}^{\max}$, above which the interaction between two dipoles is neglected. In Fig. D.1, we plot the shape anisotropy with respect to the cutoff radius for fcc-Co(001) containing 5 atomic layers. We found that the shape anisotropy increases with respect to the cutoff radius and it converges to 0.43 meV for cutoff radius above 150 Å. This value is in good agreement

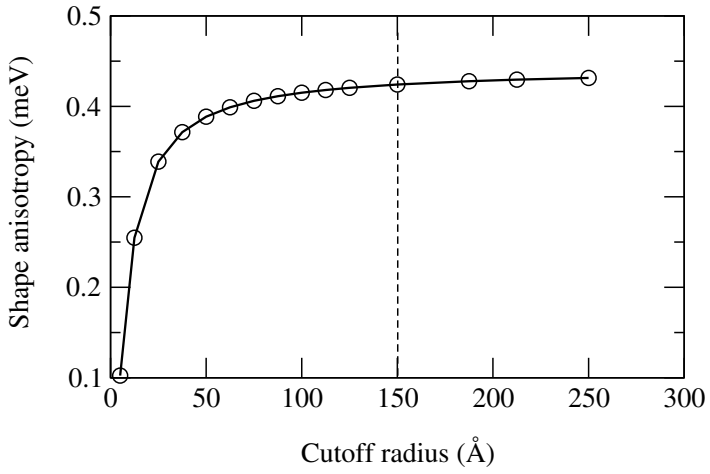

Figure D.1: Convergence test: Shape anisotropy energy with respect to the cutoff radius of a 5-layer Fe-bcc(001) slab. The cutoff radius of 150 Å is used in the following to get well-converged shape anisotropy energy.

with Ref. [95]. In the following, we use $r_{ij}^{\max} = 150$ Å and the magnetic moments are obtained from TB calculations.

Fig. D.2 shows thickness dependence of the shape anisotropy for N-layer bcc-Fe and fcc-Co slabs of different crystallographic orientations, (001)/(110) for Fe and (001)/(111) for Co, respectively. For both Fe and Co slabs, the shape anisotropy favors in-plane magnetization. In the case of Co, the shape anisotropy energy has almost the same linear dependence with respect to the thickness for both (001) and (111) orientations, this result compares rather well with Ref. [92]. The shape anisotropy of Fe slabs is slightly larger compared to Co slabs due to their larger magnetic spin moment. Interestingly for Fe slabs one can note a larger value of the shape anisotropy for the (001) slab orientation which can be attributed to an enhancement of the surface magnetization for this more open surface (typically 2.85 μ_B and 2.59 μ_B for (001) and (110) respectively).

D.2 Free Fe and Co nanocrystals

In Fig. D.3, we plot the shape anisotropy energy of Fe and Co nanocrystals of growing size. The size of nanocrystals was chosen so to keep a constant length-to-height ratio, more precisely it is ∼1.0 and 1.41 for Fe and Co, respectively. For both nanocrystals, the shape anisotropy energy favors in-plane magnetization and has an almost linear dependence with respect to the the number of atoms. Moreover the shape anisotropy of Fe nanocrystals is larger compared to Co ones due to their larger magnetic spin moment.

We define MCA to ΔE_{dip} ration as β and checked the evaluation of β with respect to the number of atoms. Interestingly, the value of β decreses when the size of the nanocrystal

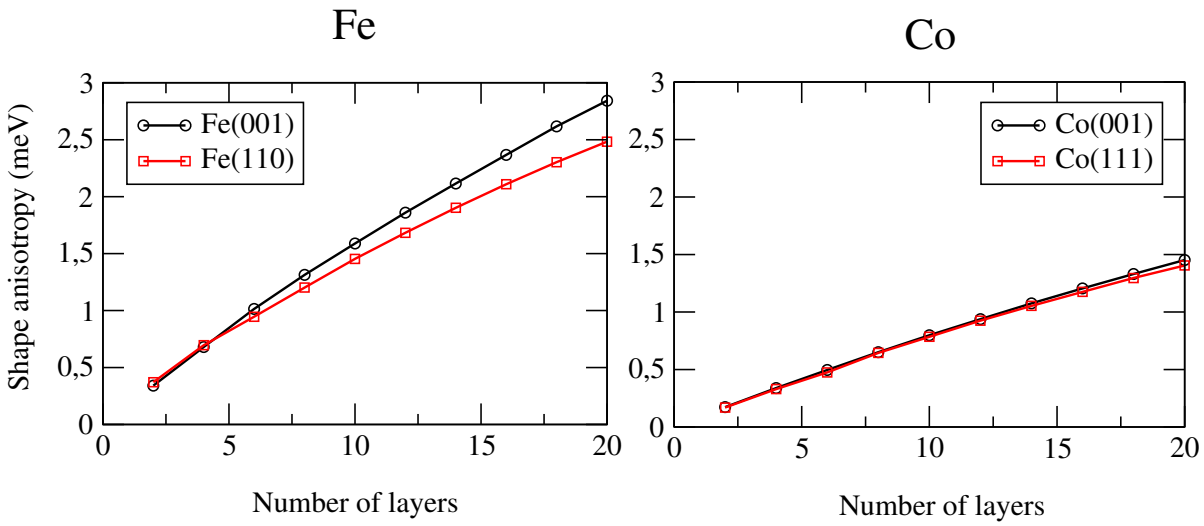

Figure D.2: Shape anisotropy energy of bcc-Fe (left) and fcc-Co (right) N-layer slabs with two different orientations. Note that the spin moments are taken from a tight binding calculation.

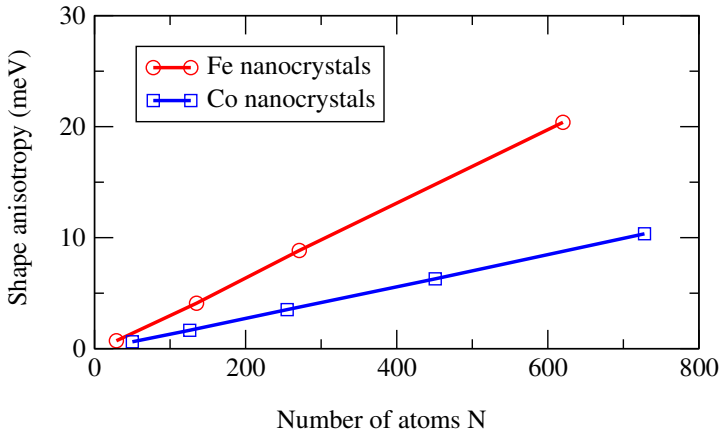

Figure D.3: Shape anisotropy energy of Co (blue circles) and Fe (red squares) nanocrystals with respect to the number of atoms. The size of nanocrystals was chosen so to keep a constant length-to-height ratio, 1.41 (Co) and ∼1.0 (Fe).

grows, for example in the case of Fe (Co) nanocrystals $\beta = 14$ (24) for $N = 29$ (50) and $\beta = 6$ (10) for $N = 620$ (728). However the amplitude of shape anisotropy energy is much smaller than its corresponding MCA so it dose not change the magnetic stability of the nanocrystals.

Publications

1. **Dongzhe Li**, Cyrille Barreteau, Martin R. Castell, Fabien Silly and Alexander Smogunov, *Out- versus in-plane magnetic anisotropy of free Fe and Co nanocrystals: Tight-binding and first-principles studies*, Phys. Rev. B **90**, 205409 (2014).

2. **Dongzhe Li**, Alexander Smogunov, Cyrille Barreteau, François Ducastelle, and Daniel Spanjaard, *Magnetocrystalline anisotropy energy of Fe(001) and Fe(110) slabs and nanoclusters: A detailed local analysis within a tight-binding model*, Phys. Rev. B **88**, 214413 (2013).

3. K. Bairagi, A. Bellec, V. Repain, C. Chacon, Y. Girard, J. Lagoute, S. Rousset, R. Breitwieser, Yu-Cheng Hu, Yen Cheng Chao, Woei Wu Pai, **Dongzhe Li**, A. Smogunov and C. Barreteau, *Tuning the magnetic anisotropy at a molecule-metal interface*, Phys. Rev. Lett. **114**, 247203 (2015).

4. Peng Yang, **Dongzhe Li**, Vincent Repain, Cyril Chacon, Yann Girard, Sylvie Rousset, Alexander Smogunov, Yannick J. Dappe, Cyrille Barreteau and Jérôme Lagoute, *C_{60} as an Atom Trap to Capture Co Adatoms*, J. Phys. Chem. C **119**, 6873 (2015).

5. Marta Viciano-Chumillas, **Dongzhe Li**, Alexander Smogunov, Sylvain Latil, Yannick J. Dappe, Cyrille Barreteau, Talal Mallah, Fabien Silly, *Tailoring the Structure of Two-Dimensional Self-Assembled Nanoarchitectures Based on Ni-Salen Building Blocks*, Chem. Eur. J. **20**, 13566 (2014).

6. **Dongzhe Li**, Cyrille Barreteau, Seiji Leo Kawahara, Jérôme Lagoute, Cyril Chacon, Yann Girard, Sylvie Rousset, Vincent Repain and Alexander Smogunov, *Symmetry-*

selected Spin-split Hybrid States in C_{60}/Ferromagnetic Interfaces, Submitted to Phys. Rev. B (arXiv:1509.06787).

Bibliography

[1] M. L. Plumer, J. van Ek, and D. Weller, *The Physics of Ultra-High-Density Magnetic Recording* (Springer, Berlin, 2001). 1, 19

[2] M. Albrecht, C. T. Rettner, A. Moser, M. E. Best, and B. D. Terris, Applied Physics Letters **81**, 2875 (2002). 1, 19

[3] F. Silly and M. R. Castell, Applied Physics Letters **87**, 063106 (2005). 2, 3, 44, 45, 47, 48, 50, 85

[4] H. J. F. Jansen, Phys. Rev. B **38**, 8022 (1988). 1, 12, 20

[5] S. R, *Principles of Quantum Mechanics: Second Edition* (Springer, Switzerland, 2013). 1, 11

[6] J. D. Burton, R. F. Sabirianov, J. P. Velev, O. N. Mryasov, and E. Y. Tsymbal, Phys. Rev. B **76**, 144430 (2007). 1

[7] D. Jacob, J. Fernández-Rossier, and J. J. Palacios, Phys. Rev. B **77**, 165412 (2008). 1

[8] B. G. Park, J. Wunderlich, D. A. Williams, S. J. Joo, K. Y. Jung, K. H. Shin, K. Olejník, A. B. Shick, and T. Jungwirth, Phys. Rev. Lett. **100**, 087204 (2008). 1, 57

[9] M. Bode, M. Heide, K. v. Bergmann, P. Ferriani, S. Heinze, A. Bihlmayer, G.and Kubetzka, O. Pietzsch, and R. Blügel, S. andWiesendange, Nature **447**, 190 (2007). 1

[10] C.-Z. Chang, J. Zhang, X. Feng, J. Shen, Z. Zhang, M. Guo, K. Li, Y. Ou, P. Wei, L.-L. Wang, et al., Science **340**, 167 (2013). 1

[11] I. G. Rau, S. Baumann, S. Rusponi, F. Donati, S. Stepanow, L. Gragnaniello, J. Dreiser, C. Piamonteze, F. Nolting, S. Gangopadhyay, et al., Science **344**, 988 (2014). 2, 58

[12] O. Eriksson, *Band-Ferromagnetism* (Springer, Berlin, 2001). 2, 20

[13] X. Wang, D.-s. Wang, R. Wu, and A. Freeman, Journal of Magnetism and Magnetic Materials **159**, 337 (1996). 3, 20, 21, 28

[14] G. H. O. Daalderop, P. J. Kelly, and M. F. H. Schuurmans, Phys. Rev. B **41**, 11919 (1990). 3, 20, 21, 28

[15] D.-s. Wang, R. Wu, and A. J. Freeman, Phys. Rev. B **47**, 14932 (1993). 3, 20, 22

[16] M. Tsujikawa and T. Oda, Phys. Rev. Lett. **102**, 247203 (2009). 3, 20, 22, 34, 69

[17] P. Bruno, Phys. Rev. B **39**, 865 (1989). 3, 20, 23, 27, 34, 69

[18] G. Autès, C. Barreteau, D. Spanjaard, and M.-C. Desjonquères, Journal of Physics: Condensed Matter **18**, 6785 (2006). 3, 14, 17, 23

[19] P. Ravindran, A. Kjekshus, H. Fjellvåg, P. James, L. Nordström, B. Johansson, and O. Eriksson, Phys. Rev. B **63**, 144409 (2001). 3

[20] C. Andersson, B. Sanyal, O. Eriksson, L. Nordström, O. Karis, D. Arvanitis, T. Konishi, E. Holub-Krappe, and J. H. Dunn, Phys. Rev. Lett. **99**, 177207 (2007). 3, 23

[21] D. Li, A. Smogunov, C. Barreteau, F. Ducastelle, and D. Spanjaard, Phys. Rev. B **88**, 214413 (2013). 3, 20, 21, 34, 43

[22] G. v. d. Laan, Journal of physics. Condensed matter **10**, 3239 (1997). 3, 23

[23] X. Wang, R. Wu, D.-s. Wang, and A. J. Freeman, Phys. Rev. B **54**, 61 (1996). 3, 20

[24] M. Jamet, W. Wernsdorfer, C. Thirion, V. Dupuis, P. Mélinon, A. Pérez, and D. Mailly, Phys. Rev. B **69**, 024401 (2004). 3, 20, 43, 48

[25] D. Li, C. Barreteau, M. R. Castell, F. Silly, and A. Smogunov, Phys. Rev. B **90**, 205409 (2014). 3, 43, 44, 45, 47, 48

[26] G. Autès, Ph.D. thesis, Université Pierre et Marie Curie, Paris (2008). 3, 14, 23

[27] C. Barreteau and D. Spanjaard, Journal of physics. Condensed matter **24**, 406004 (2012). 3, 14, 23

[28] P. Giannozzi, S. Baroni, N. Bonini, M. Calandra, R. Car, C. Cavazzoni, D. Ceresoli, G. L. Chiarotti, M. Cococcioni, I. Dabo, et al., Journal of physics. Condensed matter : an Institute of Physics journal **21**, 395502 (2009). 3, 13, 23, 29, 34, 58, 77

[29] P. Hohenberg and W. Kohn, Phys. Rev. **136**, B864 (1964). 6

[30] R. M. Dreizler and E. K. U. Gross, *Density Functional Theory: An Approach to the Quantum Many-body Problem* (Springer, Berlin, 1990). 6

[31] W. Kohn and L. J. Sham, Phys. Rev. **140**, A1133 (1965). 7

[32] J. P. Perdew and A. Zunger, Phys. Rev. B **23**, 5048 (1981). 9

[33] D. M. Ceperley and B. J. Alder, Phys. Rev. Lett. **45**, 566 (1980). 9

[34] P. Kurz, F. Förster, L. Nordström, G. Bihlmayer, and S. Blügel, Phys. Rev. B **69**, 024415 (2004). 10

[35] J. P. Perdew and Y. Wang, Phys. Rev. B **45**, 13244 (1992). 10

[36] J. P. Perdew, K. Burke, and M. Ernzerhof, Phys. Rev. Lett. **77**, 3865 (1996). 10, 30, 35, 58, 65

[37] I. Žutić, J. Fabian, and S. Das Sarma, Rev. Mod. Phys. **76**, 323 (2004). 13, 19

[38] W. E. Pickett, Computer Physics Reports **9**, 115 (1989). 13, 29

[39] A. D. Corso and A. M. Conte, Phys. Rev. B **71**, 115106 (2005). 13, 14

[40] D. R. Hamann, M. Schlüter, and C. Chiang, Phys. Rev. Lett. **43**, 1494 (1979). 13

[41] D. Vanderbilt, Phys. Rev. B **41**, 7892 (1990). 13

[42] M. Mehl and D. Papaconstantopoulos, Physical Review B **54**, 4519 (1996). 16

[43] E. C. Stoner, Proc. Roy. Soc. A **154**, 656 (1934). 16

[44] E. C. Stoner, Proc. Roy. Soc. A **165**, 372 (1938). 16

[45] F. Ducastelle, *Order and Phase Stability in Alloys* (Springer, Amsterdam, 1991). 22

[46] M. C. Desjonquères and D. Spanjaard, *Concept in Surface Physics* (Springer Verlag, Berlin, 1995). 22

[47] M. Cinal and D. M. Edwards, Phys. Rev. B **55**, 3636 (1997). 22, 28

[48] M. Cinal, D. M. Edwards, and J. Mathon, Phys. Rev. B **50**, 3754 (1994). 28

[49] F. Gimbert and L. Calmels, Phys. Rev. B **86**, 184407 (2012). 28

[50] T. Oda, A. Pasquarello, and R. Car, Phys. Rev. Lett. **80**, 3622 (1998). 29

[51] R. Gebauer and S. Baroni, Phys. Rev. B **61**, R6459 (2000). 29

[52] U. Gradmann and J. Müller, physica status solidi (b) **27**, 313 (1968), ISSN 1521-3951. 33

[53] C. Chen, Journal of Materials Science **26**, 3125 (1991). 33

[54] S. Mangin, D. Ravelosona, J. A. Katine, M. J. Carey, B. D. Terris, and E. E. Fullerton, Nature Materials **5**, 210 (2006). 33

[55] U. Gradmann, *Ferromagnetic Materials* (Springer, Amsterdam, 1993). 33

[56] E. Beaurepaire, H. Bulou, F. Scheurer, and K. Jean-Paul, *Magnetism and Synchrotron Radiation* (Springer, 2001). 34

[57] B. Heinrich and J. A. C. Bland, *Ultrathin Magnetic Structures II* (Springer, Berlin, 1994). 34

[58] G. Y. Guo, W. M. Temmerman, and H. Ebert, Journal of Physics: Condensed Matter **3**, 8205 (1991). 34

[59] J. G. Gay and R. Richter, Phys. Rev. Lett. **56**, 2728 (1986). 34

[60] J. G. Gay and R. Richter, Journal of Applied Physics **61** (1987). 34

[61] A. J. Freeman and C. Li, Journal of Applied Physics **69** (1991). 34

[62] S. Pick and H. Dreyssé, Phys. Rev. B **46**, 5802 (1992). 34

[63] S. Pick, J. Dorantes-Dávila, G. M. Pastor, and H. Dreyssé, Phys. Rev. B **50**, 993 (1994). 34

[64] G. H. O. Daalderop, P. J. Kelly, and M. F. H. Schuurmans, Phys. Rev. B **42**, 7270 (1990). 34

[65] G. H. O. Daalderop, P. J. Kelly, and M. F. H. Schuurmans, Phys. Rev. B **44**, 12054 (1991). 34

[66] G. H. O. Daalderop, P. J. Kelly, and F. J. A. den Broeder, Phys. Rev. Lett. **68**, 682 (1992). 34

[67] D.-s. Wang, R. Wu, and A. J. Freeman, Phys. Rev. Lett. **70**, 869 (1993). 34

[68] D.-s. Wang, R. Wu, and A. J. Freeman, Phys. Rev. B **47**, 14932 (1993). 34

[69] F. Bisio, R. Moroni, F. Buatier de Mongeot, M. Canepa, and L. Mattera, Phys. Rev. Lett. **96**, 057204 (2006). 34

[70] Z. Q. Qiu, J. Pearson, and S. D. Bader, Phys. Rev. Lett. **70**, 1006 (1993). 34

[71] J. Chen and J. L. Erskine, Phys. Rev. Lett. **68**, 1212 (1992). 34

[72] O. Thomas, Q. Shen, P. Schieffer, N. Tournerie, and B. Lépine, Phys. Rev. Lett. **90**, 017205 (2003). 34

[73] O. Durand, J. Childress, P. Galtier, R. Bisaro, and A. Schuhl, Journal of Magnetism and Magnetic Materials **145**, 111 (1995), ISSN 0304-8853. 34

[74] J. Li, M. Przybylski, F. Yildiz, X. D. Ma, and Y. Z. Wu, Phys. Rev. Lett. **102**, 207206 (2009). 34, 35, 73

[75] C. Quirós, S. M. Valvidares, O. Robach, and S. Ferrer, Journal of Physics: Condensed Matter **17**, 5551 (2005). 34

[76] M. Przybylski, L. Yan, J. Żukrowski, M. Nyvlt, Y. Shi, A. Winkelmann, J. Barthel, M. Waśniowska, and J. Kirschner, Phys. Rev. B **73**, 085413 (2006). 34

[77] F. El Gabaly, S. Gallego, C. Muñoz, L. Szunyogh, P. Weinberger, C. Klein, A. K. Schmid, K. F. McCarty, and J. de la Figuera, Phys. Rev. Lett. **96**, 147202 (2006). 34

[78] D. Weller, J. Stöhr, R. Nakajima, A. Carl, M. G. Samant, C. Chappert, R. Mégy, P. Beauvillain, P. Veillet, and G. A. Held, Phys. Rev. Lett. **75**, 3752 (1995). 34

[79] K. Chen, R. Frömter, S. Rössler, N. Mikuszeit, and H. P. Oepen, Phys. Rev. B **86**, 064432 (2012). 34

[80] L. Szunyogh, B. Újfalussy, and P. Weinberger, Phys. Rev. B **51**, 9552 (1995). 34

[81] L. Szunyogh, B. Újfalussy, and P. Weinberger, Phys. Rev. B **55**, 14392 (1997). 34

[82] C. Li, A. J. Freeman, H. J. F. Jansen, and C. L. Fu, Phys. Rev. B **42**, 5433 (1990). 34

[83] H. X. Yang, M. Chshiev, B. Dieny, J. H. Lee, A. Manchon, and K. H. Shin, Phys. Rev. B **84**, 054401 (2011). 34, 58

[84] I. Galanakis, M. Alouani, and H. Dreyssé, Phys. Rev. B **62**, 3923 (2000). 34

[85] G. Nicolas, J. Dorantes-Dávila, and G. M. Pastor, Phys. Rev. B **74**, 014415 (2006). 34, 43, 48

[86] A. Buruzs, P. Weinberger, L. Szunyogh, L. Udvardi, P. I. Chleboun, A. M. Fischer, and J. B. Staunton, Phys. Rev. B **76**, 064417 (2007). 34

[87] B. Újfalussy, L. Szunyogh, P. Bruno, and P. Weinberger, Phys. Rev. Lett. **77**, 1805 (1996). 34

[88] W. Weber, C. H. Back, A. Bischof, C. Würsch, and R. Allenspach, Phys. Rev. Lett. **76**, 1940 (1996). 34

[89] C. A. F. Vaz, J. A. C. Bland, and G. Lauhoff, Reports on Progress in Physics **71**, 056501 (2008). 34

[90] S. Manna, P. L. Gastelois, M. Dąbrowski, P. Kuświk, M. Cinal, M. Przybylski, and J. Kirschner, Phys. Rev. B **87**, 134401 (2013). 35, 73

[91] M. Przybylski, M. Dąbrowski, U. Bauer, M. Cinal, and J. Kirschner, Journal of Applied Physics **111**, (2012). 35, 73

[92] H. Zhang, Ph.D. thesis, Dresden University of Technology (2009). 37, 88

[93] N. Rougemaille, A. T. NDiaye, J. Coraux, C. Vo-Van, O. Fruchart, and A. K. Schmid, Applied Physics Letters **101**, 142403 (2012). 39

[94] R. Decker, J. Brede, N. Atodiresei, V. Caciuc, S. Blügel, and R. Wiesendanger, Phys. Rev. B **87**, 041403 (2013). 39

[95] K. Bairagi, A. Bellec, V. Repain, C. Chacon, Y. Girard, Y. Garreau, J. Lagoute, S. Rousset, R. Breitwieser, Y.-C. Hu, et al., Phys. Rev. Lett. **114**, 247203 (2015). 39, 40, 64, 74, 88

[96] J. P. Bucher, D. C. Douglass, and L. A. Bloomfield, Phys. Rev. Lett. **66**, 3052 (1991). 43

[97] I. M. L. Billas, J. A. Becker, A. Châtelain, and W. A. de Heer, Phys. Rev. Lett. **71**, 4067 (1993). 43

[98] A. J. Cox, J. G. Louderback, S. E. Apsel, and L. A. Bloomfield, Phys. Rev. B **49**, 12295 (1994). 43

[99] K. Lee, Phys. Rev. B **58**, 2391 (1998). 43

[100] T. Balashov, T. Schuh, A. F. Takács, A. Ernst, S. Ostanin, J. Henk, I. Mertig, P. Bruno, T. Miyamachi, S. Suga, et al., Phys. Rev. Lett. **102**, 257203 (2009). 43

[101] M. Jamet, W. Wernsdorfer, C. Thirion, D. Mailly, V. Dupuis, P. Mélinon, and A. Pérez, Phys. Rev. Lett. **86**, 4676 (2001). 43

[102] F. Luis, J. M. Torres, L. M. García, J. Bartolomé, J. Stankiewicz, F. Petroff, F. Fettar, J.-L. Maurice, and A. Vaurès, Phys. Rev. B **65**, 094409 (2002). 43

[103] G. M. Pastor, J. Dorantes-Dávila, S. Pick, and H. Dreyssé, Phys. Rev. Lett. **75**, 326 (1995). 43, 48

[104] Y. Xie and J. A. Blackman, Phys. Rev. B **74**, 054401 (2006). 43

[105] B. Lazarovits, L. Szunyogh, and P. Weinberger, Phys. Rev. B **65**, 104441 (2002). 43

[106] R. Félix-Medina, J. Dorantes-Dávila, and G. M. Pastor, Phys. Rev. B **67**, 094430 (2003). 43

[107] S. Sahoo, A. Hucht, M. E. Gruner, G. Rollmann, P. Entel, A. Postnikov, J. Ferrer, L. Fernández-Seivane, M. Richter, D. Fritsch, et al., Phys. Rev. B **82**, 054418 (2010). 43

[108] D. H. Kim, J. S. Yang, K. W. Lee, S. D. Bu, T. W. Noh, S.-J. Oh, Y.-W. Kim, J.-S. Chung, H. Tanaka, H. Y. Lee, et al., Applied Physics Letters **81** (2002). 44

[109] Y. Qiang, R. F. Sabiryanov, S. S. Jaswal, Y. Liu, H. Haberland, and D. J. Sellmyer, Phys. Rev. B **66**, 064404 (2002). 44

[110] J. Martin, J. Nogues, K. Liu, J. Vicent, and I. K. Schuller, Journal of Magnetism and Magnetic Materials **256**, 449 (2003), ISSN 0304-8853. 44

[111] F. Silly and M. R. Castell, Applied Physics Letters **87**, 053106 (2005). 44

[112] J. Sun, C. Wu, F. Silly, A. A. Koos, F. Dillon, N. Grobert, and M. R. Castell, Chem. Commun. **49**, 3748 (2013). 44

[113] H. F. Ding, A. K. Schmid, D. Li, K. Y. Guslienko, and S. D. Bader, Phys. Rev. Lett. **94**, 157202 (2005). 44

[114] W. A. A. Macedo and W. Keune, Phys. Rev. Lett. **61**, 475 (1988). 44

[115] M. A. Torija, Z. Gai, N. Myoung, E. W. Plummer, and J. Shen, Phys. Rev. Lett. **95**, 027201 (2005). 44

[116] J. de la Figuera, J. E. Prieto, C. Ocal, and R. Miranda, Phys. Rev. B **47**, 13043 (1993). 44

[117] C. Rath, J. E. Prieto, S. Müller, R. Miranda, and K. Heinz, Phys. Rev. B **55**, 10791 (1997). 44

[118] C. H. Lee, H. He, F. Lamelas, W. Vavra, C. Uher, and R. Clarke, Phys. Rev. Lett. **62**, 653 (1989). 44

[119] A. Midoir, H. Magnan, L. Barbier, P. L. Fèvre, and D. Chandesris, Surface Science **562**, 137 (2004), ISSN 0039-6028. 44

[120] M. Alden, S. Mirbt, H. L. Skriver, N. M. Rosengaard, and B. Johansson, Phys. Rev. B **46**, 6303 (1992). 44

[121] M. R. Castell, Surface Science **505**, 1 (2002), ISSN 0039-6028. 44

[122] W. Winterbottom, Acta Metallurgica **15**, 303 (1967), ISSN 0001-6160. 46

[123] M. J. Spencer, A. Hung, I. K. Snook, and I. Yarovsky, Surface Science **513**, 389 (2002), ISSN 0039-6028. 47

[124] M.-C. Desjonquères, C. Barreteau, G. Autès, and D. Spanjaard, Phys. Rev. B **76**, 024412 (2007). 48

[125] L. E. Nistor, B. Rodmacq, S. Auffret, and B. Dieny, Applied Physics Letters **94**, 012512 (2009). 57

[126] G. Kim, Y. Sakuraba, M. Oogane, Y. Ando, and T. Miyazaki, Applied Physics Letters **92**, 172502 (2008). 57

[127] K. Mizunuma, S. Ikeda, J. H. Park, H. Yamamoto, H. Gan, K. Miura, H. Hasegawa, J. Hayakawa, F. Matsukura, and H. Ohno, Applied Physics Letters **95**, 232516 (2009). 57

[128] L. Gao, X. Jiang, S.-H. Yang, J. D. Burton, E. Y. Tsymbal, and S. S. P. Parkin, Phys. Rev. Lett. **99**, 226602 (2007). 57

[129] N. Nakajima, T. Koide, T. Shidara, H. Miyauchi, H. Fukutani, A. Fujimori, K. Iio, T. Katayama, M. Nývlt, and Y. Suzuki, Phys. Rev. Lett. **81**, 5229 (1998). 57

[130] D. Weller, Y. Wu, J. Stöhr, M. G. Samant, B. D. Hermsmeier, and C. Chappert, Phys. Rev. B **49**, 12888 (1994). 57

[131] S. Bornemann, O. Šipr, S. Mankovsky, S. Polesya, J. B. Staunton, W. Wurth, H. Ebert, and J. Minár, Phys. Rev. B **86**, 104436 (2012). 58

[132] S. Monso, B. Rodmacq, S. Auffret, G. Casali, F. Fettar, B. Gilles, B. Dieny, and P. Boyer, Applied Physics Letters **80** (2002). 58

[133] S. Ikeda, K. Miura, H. Yamamoto, K. Mizunuma, H. D. Gan, M. Endo, S. Kanai, J. Hayakawa, F. Matsukura, and H. Ohno, Nature Materials **9**, 721 (2010). 58

[134] M. Fechner, S. Ostanin, and I. Mertig, Phys. Rev. B **77**, 094112 (2008). 58

[135] J. M. De Teresa, A. Barthélémy, A. Fert, J. P. Contour, R. Lyonnet, F. Montaigne, P. Seneor, and A. Vaurès, Phys. Rev. Lett. **82**, 4288 (1999). 58

[136] J. M. De Teresa, A. Barthélémy, A. Fert, J. P. Contour, F. Montaigne, and P. Seneor, Science **286**, 507 (1999). 58

[137] I. I. Oleinik, E. Y. Tsymbal, and D. G. Pettifor, Phys. Rev. B **65**, 020401 (2001). 59

[138] A. Hallal, H. X. Yang, B. Dieny, and M. Chshiev, Phys. Rev. B **88**, 184423 (2013). 64

[139] D. Wortmann, S. Heinze, P. Kurz, G. Bihlmayer, and S. Blügel, Phys. Rev. Lett. **86**, 4132 (2001). 69

[140] G. H. O. Daalderop, P. J. Kelly, and M. F. H. den Schuurnans, Phys. Rev. B **50** (1994). 69

[141] R. Skomski, X.-H. Wei, and D. Sellmyer, Magnetics, IEEE Transactions on **43**, 2890 (2007), ISSN 0018-9464. 74

Magneto-crystalline anisotropy of metallic nanostructures: Tight-binding and first-principles studies

The crucial issue in exploring ultimate density data storage is magneto-crystalline anisotropy (MCA) which originates from spin-orbit coupling. Using both tight-binding and first-principles methods, we report the MCA of Fe and Co nanocrystals that can be grown epitaxially on $SrTiO_3$ with a remarkable control of their size, shape and structure. In order to define the proper local decomposition of MCA, we implemented the "Force Theorem" within the grand-canonical formulation in QUANTUM ESPRESSO as well as in our tight-binding model. Interestingly, for both elements, the total MCA of free nanocrystals is largely dominated by (001) facets resulting in the opposite behavior: out-of-plane and in-plane magnetization direction is favored in Fe and Co nanocrystals (containing up to several hundred atoms), respectively. We also find a strong enhancement of MCA for small clusters (containing only several atoms) upon their deposition on a $SrTiO_3$ substrate. As a consequence, we predict that the Fe nanocrystals (even rather small) should be magnetically stable and are thus good potential candidates for magnetic storage devices. Finally, our rather general orbital-resolved analysis of MCA applies also to other systems and allows, for example, predicting the MCA behavior of magnetic thin films upon covering by various organic materials such as graphene or C_{60} molecule.

Anisotropie magnéto-cristalline de nanostructures métalliques: étude combinant par méthode des liaisons fortes et calculs premiers principes

La question cruciale dans l'exploration du stockage ultime à haute densité est l'anisotropie magnéto-cristalline (MCA) qui provient du couplage spin-orbite. Utilisant à la fois la méthode des liaisons fortes et les calculs "premiers principes", nous calculons la MCA de nanocristaux de fer et de cobalt qui peuvent être obtenus par croissance épitaxiale sur un substrat de $SrTiO_3$ avec un contrôle remarquable de leur taille, forme et structure. Afin de définir une décomposition locale appropriée de la MCA, nous avons implémenté le "Théorème de Force" à l'aide d'une formulation grand-canonique dans le code QUANTUM ESPRESSO ainsi que dans notre modèle de liaisons fortes. Il est intéressant de noter que pour les deux éléments, la MCA totale de nanocristaux isolés est largement dominée par les facettes (001) dont il résulte un comportement opposé: une anisotropie "hors-plan" pour les nanocristaux (contenant plusieurs centaines d'atomes) de fer et "dans le plan" pour ceux de cobalt. Nous avons également mis en évidence un fort renforcement de la MCA pour les petits clusters (contenant quelques atomes seulement) déposés sur un substrat $SrTiO_3$. En conséquence, nous prévoyons que les nanocristaux de fer (même de très petite taille) devraient être magnétiquement plus stables et sont donc de bons candidats potentiels pour le stockage magnétique. Enfin, notre analyse MCA résolu en orbitales s'applique également à d'autres système et permet, par exemple, de prédire le comportement de la MCA de films minces magnétiques après déposition de matériaux organiques comme le graphène ou de molécules tel C_{60}.